

AD-A262 184



①

ARMY RESEARCH LABORATORY



Tungsten Alloy Technology

Edited by
Robert J. Dowding

ARL-MR-57

January 1993

DTIC
ELECTR
MAR 16 1993
S B D

98 3 16 036

93-05306



9507

The findings in this report are not to be construed as an official Department of the Army position unless so designated by other authorized documents.

Citation of manufacturer's or trade names does not constitute an official endorsement or approval of the use thereof.

Destroy this report when it is no longer needed. Do not return it to the originator.

REPORT DOCUMENTATION PAGE

Form Approved
OMB No. 0704-0188

Public reporting burden for this collection of information is estimated to average 1 hour per response, including the time for reviewing instructions, searching existing data sources, gathering and maintaining the data needed, and completing and reviewing the collection of information. Send comments regarding this burden estimate or any other aspect of this collection of information, including suggestions for reducing this burden, to Washington Headquarters Services, Directorate for Information Operations and Reports, 1215 Jefferson Davis Highway, Suite 1204, Arlington, VA 22202-4302, and to the Office of Management and Budget, Paperwork Reduction Project (0704-0188), Washington, DC 20503.

1. AGENCY USE ONLY (Leave blank)		2. REPORT DATE January 1993	3. REPORT TYPE AND DATES COVERED Final Report	
4. TITLE AND SUBTITLE Tungsten Alloy Technology			5. FUNDING NUMBERS	
6. AUTHOR(S) Edited by Robert J. Dowding				
7. PERFORMING ORGANIZATION NAME(S) AND ADDRESS(ES) U.S. Army Research Laboratory Watertown, Massachusetts 02172-0001 ATTN: AMSRL-MA-MB			8. PERFORMING ORGANIZATION REPORT NUMBER ARL-MR-57	
9. SPONSORING/MONITORING AGENCY NAME(S) AND ADDRESS(ES) U.S. Army Research Laboratory 2800 Powder Mill Road Adelphi, Maryland 20783-1197			10. SPONSORING/MONITORING AGENCY REPORT NUMBER	
11. SUPPLEMENTARY NOTES Presented at Proceedings of the International Conference on Tungsten and Tungsten Alloys, Arlington, VA, November 16-18, 1992.				
12a. DISTRIBUTION/AVAILABILITY STATEMENT Approved for public release; distribution unlimited.			12b. DISTRIBUTION CODE A	
13. ABSTRACT (Maximum 200 words) The papers collected here represent contributions to the International Conference on Tungsten and its Alloys in which Materials Directorate personnel had primary or secondary authorship responsibility. The conference was held in Arlington, VA, 16-18 November 1992. These papers are indicative of the present interests of the Army in tungsten alloys for kinetic energy penetrator applications. The papers are compiled in alphabetical order, according to the last name of the first author listed.				
14. SUBJECT TERMS Tungsten alloys, Heavy alloys, Composites, Mechanical properties, Metallography, Transition Electron Microscopy, Dynamic testing, Hopkinson bar, Proc. Tech.			15. NUMBER OF PAGES 85	
			16. PRICE CODE	
17. SECURITY CLASSIFICATION OF REPORT Unclassified	18. SECURITY CLASSIFICATION OF THIS PAGE Unclassified	19. SECURITY CLASSIFICATION OF ABSTRACT Unclassified	20. LIMITATION OF ABSTRACT UL	

Contents

	Page
TUNGSTEN ALLOY PENETRATOR INTERACTION WITH A TITANIUM ALUMINIDE COMPOSITE.	1
Ernest S. C. Chin, Robert J. Dowding, Patrick Woolsey, and Ronald R. Biederman	
QUASISTATIC AND DYNAMIC PROPERTIES OF TUNGSTEN HEAVY ALLOYS WITH L1 ₂ INTERMETALLIC MATRICIES.	11
S. Guha, C. Kyriacou, J. C. Withers, R. O. Loutfy, G. T. Gray III, and R. J. Dowding	
DYNAMIC SHEAR TESTING OF TUNGSTEN BASED COMPOSITES	21
Murray Kornhauser and Robert J. Dowding	
EFFECT OF IMPURITIES ON THE ELECTRONIC STRUCTURE OF GRAIN BOUNDARIES AND INTERGRANULAR COHESION IN TUNGSTFN.	27
Genrich L. Krasko	
POST-FABRICATION EVALUATION AND CHARACTERIZATION OF A COMMERCIAL TUNGSTEN HEAVY ALLOY.	37
John B. Posthill, Robert J. Dowding, and Kenneth J. Tauer	
YIELD PROPERTIES OF TUNGSTEN AND TUNGSTEN HEAVY ALLOYS	45
Kenneth F. Ryan and Robert J. Dowding	
BALLISTIC PERFORMANCE OF A COATED TUNGSTEN POWDER ALLOY.	57
Kenneth J. Tauer, Robert J. Dowding, and Patrick Woolsey	
DEFORMATION AND FAILURE BEHAVIOR OF 93W-5Ni-2Fe AT DIFFERENT SHEAR STRAIN RATE LOADING.	65
Tusit Weerasooriya and Patricia Beaulieu	
PERFORMANCE-PROPERTY RELATIONSHIPS IN TUNGSTEN ALLOY PENETRATORS.	73
Patrick Woolsey, Robert J. Dowding, Kenneth J. Tauer, and Frank S. Hodi	

Accession For	
NTIS GRA&I	<input checked="" type="checkbox"/>
DTIC TAB	<input type="checkbox"/>
Unannounced	<input type="checkbox"/>
Justification	
By	
Distribution/	
Availability Codes	
Dist	Avail and/or Special
A-1	

TUNGSTEN ALLOY PENETRATOR INTERACTION WITH A TITANIUM ALUMINIDE COMPOSITE

Ernest S.C. Chin, Robert J. Dowding and Patrick Woolsey
U.S. Army Research Laboratory, Materials Directorate,
Watertown, MA

Ronald R. Biederman
Worcester Polytechnic Institute, Worcester, MA

ABSTRACT

A 7.5 vol% titanium diboride (TiB₂) reinforced titanium aluminide (Ti-48 at% Al) forging was impacted by a long rod tungsten heavy alloy (WHA) kinetic energy penetrator. Post-mortem failure analysis of the penetration cavity was performed. Microstructural analysis of the residual WHA along the side wall of the penetration cavity showed localized regions of both highly deformed and undeformed tungsten grains. Ultra-fine particles of tungsten were dispersed throughout the nickel-iron-cobalt (Ni-Fe-Co) matrix of the WHA. Intermixing of TiB₂ particles and titanium aluminide composite fragments within the Ni-Fe-Co matrix was observed along the penetrator/target interfacial regions. Residual WHA penetrator materials also infiltrated into the fine cracks and voids of the titanium aluminide composite, creating what appears to be a "healing" process which prevented catastrophic failure of the target material.

INTRODUCTION

The failure modes of traditional metallic armor materials are a reasonably well established area. Much less attention has been given to the large variety of high-performance composite materials which are now coming into more general use. Excepting the established uses of fiber reinforced polymers, there is only a limited amount of data available regarding the ballistic behavior of inorganic composite materials. Some limited studies on aluminum matrix composites have indicated that the reinforced aluminum was better¹ or significantly more efficient² than the monolithic base alloy against tungsten heavy alloy (WHA) penetrators. Other preliminary studies at the U.S. Army Research Laboratory's Materials Directorate (ARL-MD) have demonstrated improvement over conventional aluminum armor alloy in penetration resistance against armor piercing (AP) projectiles for a thermomechanically processed silicon carbide-reinforced 6061 aluminum system³. Furthermore, exploratory studies on intermetallics at ARL-MD also revealed ballistic equivalence of titanium aluminide composites to aluminum oxide ceramic against WHA penetrators⁴. This equivalence of performance makes the interaction of the WHA penetrator and intermetallic target system of considerable interest from a materials perspective.

Titanium Aluminide Composites

Until the past few years, intermetallic compounds were employed primarily as precipitation hardening and strengthening agents in metallic alloys. However, the search for improved materials in response to the stringent performance guidelines set forth by new technology thrust areas, such as the Integrated High Performance Turbine Engine Technology Initiative (IHPTET), the NASA High Temperature Engine Materials Technology Program (HITEMP), and the National Aerospace Plane (NASP) Program, has brought a number of new materials systems to cognizance. Intermetallic materials are one focal point of these materials development efforts.

Titanium aluminides have been the most widely studied intermetallic system, and continue to be the focus of numerous research efforts^{5,6}. They possess many valuable properties, including low densities, good high temperature stiffness, excellent creep resistance, and excellent oxidation resistance. The critical obstacles to their broad utilization in engineering applications are their poor room temperature (RT) ductility and toughness associated with this class of material. Significant progress in addressing and improving ambient temperature ductility and fracture toughness is being made through suitable alloying, thermomechanical processing (TMP), and composite reinforcement routes. In order to meet the expanding requirements for higher performance materials, extensive efforts have been directed toward the production of intermetallic matrix composite materials.

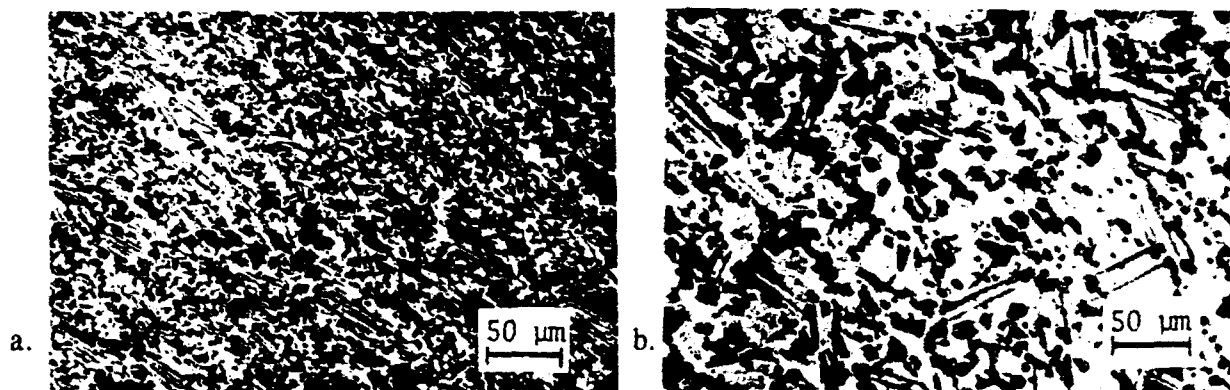
The most common types of intermetallic matrix composites (IMCs) are fiber-reinforced IMCs and particulate-reinforced IMCs. Fiber-reinforced intermetallic composites provide excellent high temperature stiffness and strength, with the additional benefit of good damage tolerance. The reinforcing fibers typically have a tailored surface chemistry to provide high temperature stability and interface compatibility. The composite may be consolidated by either standard powder metallurgy processes, or via a spray deposition and hot pressing operation. Both of these methods are relatively expensive when compared to conventional ingot metallurgy. Recent advances in the development of *in situ* composites have led to another means of producing IMCs with the desired reinforcing agents. This method relies upon the precipitation of selected phases in a standard ingot melt environment by a suitably prepared exothermic reaction. Martin Marietta Laboratories' (MML) proprietary XDTM metallic⁷ and intermetallic⁸ composites are produced by a process based on the aforementioned principle. The previous ARL-MD ballistic study incorporated several compositional variations of XDTM intermetallic composites⁹. One of the outcome from this study was that each of the compositional variations tested had a performance, on an areal density basis, equivalent to that of aluminum oxide. One particular composition, a 7.5 vol% TiB₂ reinforced titanium aluminide, was chosen for further examination.

This XDTM intermetallic composite is a TiB₂-reinforced titanium aluminide with a composition near the gamma (γ) region of the Al-Ti phase diagram¹⁰. The TiB₂ dispersoids are typically single crystal¹¹ and act as nucleation sites in refining and stabilizing the as-cast microstructure¹². The resultant fine-grained microstructure is indicative to better hot workability and room temperature ductility. At elevated temperatures, the reinforcements pin dislocations to retard creep flow, thus allowing excellent mechanical property retention¹³. The reinforcement loading, distribution, and size play a major role in affecting all mechanical properties exhibited by this material. For example, a reinforcement loading of up to 7 vol% can increase the yield strength from the 400 MPa characteristic of the matrix to around 600 MPa with no significant loss of ductility ranging from 0.8 to 1.1%. Both direct and indirect strengthening mechanisms contribute to this effect¹⁴. The specific distribution of reinforcing particles in the titanium aluminide matrix can be varied during the XDTM casting process.

Intermetallic Material Condition

The titanium aluminide IMC described in this study was produced by MML via the XDTM process. The particular material examined here is a 7.5 vol% TiB₂ reinforced Ti-48Al-2V forging provided by MML. For simplicity, it will be referred to in the text as 7.5XD. The material was provided as a 3.81 cm thick hot-forged pancake, with a fine duplex microstructure consisting of

lamellar and equiaxed recrystallized $\alpha_2(\text{Ti}_3\text{Al}) + \gamma(\text{TiAl})$, grains (see •Figure 1a). Before testing, the 7.5XD was annealed in the $\alpha+\gamma$ temperature region to obtain a higher hardness from the as-forged condition. On the Al-Ti phase diagram, this region is bounded by the $\alpha \rightarrow \alpha_2 + \gamma$ eutectoid isotherm and the α transus. A previous study of 5 vol% $\text{TiB}_2/\text{Ti-48 at\% Al}$ found that the $\alpha \rightarrow \alpha_2 + \gamma$ eutectoid isotherm falls between 1300°C and 1310°C, and the α transus temperature falls between 1360°C and 1375°C¹⁵. Therefore, the heat treatment condition selected was 1330°C for 20 hours. Heat treatment was performed in a vacuum furnace, with the specimen wrapped in tantalum foil. The hardness change resulting from this heat treatment is shown in Table 1. Coarsening of the duplex structure toward a subtransus microstructure was observed in the 7.5 XD after the heat treatment (see •Figure 1b). The matrix consists of fine equiaxed grains of α_2 and γ with an interspersed lamellar component of alternating laths of α_2 and γ . The TiB_2 particles are faceted, and are generally distributed along the flow lines produced by the hot forging process. The resulting microstructure exhibited a significant increase in hardness from the as-received condition.



•Figure 1. BEI of a Transverse Section from 7.5 XD in (a) As-Received, and (b) Post-Heat Treatment Conditions.

Table 1. Vickers Hardness (1 kg Load)

Composition	As Received	Heat Treated (1330°C - 20 hr)
(Ti-48 at.% Al-2V + 7.5 vol% TiB_2)	414.7	505.1

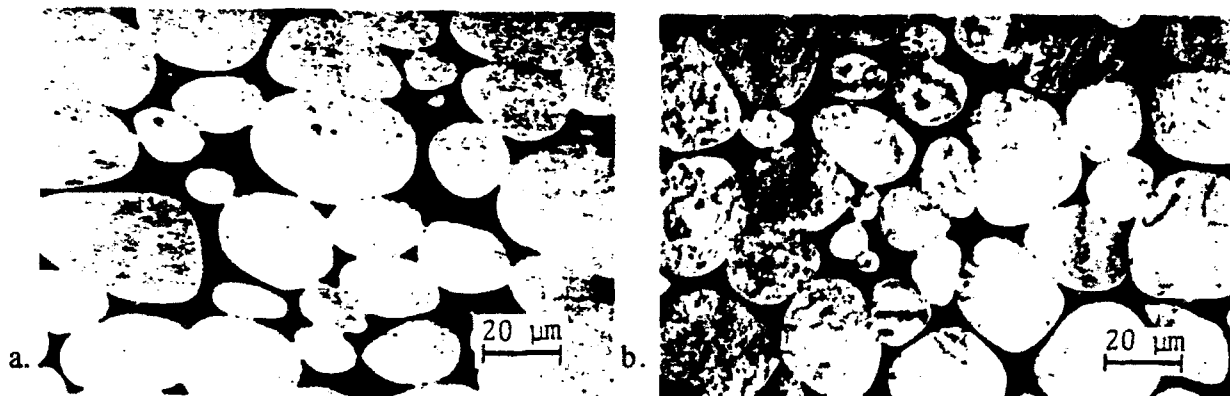
Ballistic Test Conditions

Ballistic tests were performed at ARL-MD by the residual penetration method. Residual penetration ballistic tests rely on the construction of a performance map for a material over a range of areal densities. Areal density is the measure of target material mass per unit surface area. Varying the areal density corresponds to varying the thickness of target material. Performance is measured by the depth of penetration of a projectile into a semi-infinite backplate after passing through a target containing the material to be evaluated. This penetration in the backplate is known as the residual penetration; for convenience, it is often referred to as "DOP", for "depth of (residual) penetration". The basic assumptions which must be satisfied to ensure applicability of the test are as follows: that the projectile class of interest is a ductile heavy alloy long rod; that the operative penetration mechanism is hydrodynamic erosion, rather than rigid body penetration, and that the backing plate is of effectively infinite thickness with regard to the final position of the penetrator, so that no rear surface effects influence the penetration.

The standard residual penetration target consists of a material confinement package in contact with a thick steel backplate of monolithic rolled homogeneous armor steel (commonly

termed RHA), per U.S. MIL-A-12560, Class 3. Target packages are mechanically clamped to the backup block for testing. After the ballistic test, the penetration cavities in the steel backing block are directly sectioned, and measurements of residual penetration depth are made on the sections.

The projectile used was a standard 91% tungsten heavy alloy long rod, with an aspect ratio (L/D) of 10:1 and a hemispherical nose. The rod weight was 65 grams. The tungsten alloy employed is a standard commercial material, Teledyne X-27C, in a 15% swaged condition. It has a bulk density of 17.35 g/cc, a 0.2% yield strength of 1275 MPa, an ultimate tensile strength of 1285 MPa with a reduction area of 23.8%. Nominal composition by weight is 91%W, 4.5% Ni, 2% Fe, and 2.5% Co. Longitudinal and transverse views of this alloy are shown in Figure 2a-b. More complete discussions of the penetration performance of this tungsten alloy rod have been published by Dowding¹⁶ and Woolsey¹⁷, while papers by Hohler and Stulp¹⁸, and Anderson and Walker¹⁹, among others, provide detailed analyses regarding the penetration of long rods in homogeneous semi-infinite media. Further information regarding the residual penetration test method, including the development of the ceramic baselines, may be found in various ARL-MD reports^{20,21}.



•Figure 2. SEI of Virgin WHA Penetrator in (a) Longitudinal and (b) Transverse Directions.

The 7.5XD titanium aluminide plate was prepared as a standard geometry target, of 15 cm by 15 cm lateral dimensions and 3.81 cm thickness, and tested at a 1500 m/s nominal velocity. The backing plate was sectioned in the normal manner to permit measurement of the residual penetration. In addition, specimens of the target material were taken from the area surrounding the penetration cavity by electro-discharge machining (EDM). The reference material employed for purposes of performance comparison was a 90% pure, sintered aluminum oxide from Coors Ceramics (AD90).

Analytical Techniques

Post-mortem fractographic analysis was performed on the impacted target to observe the interaction region and attempt to determine the governing dynamic fracture mechanisms in this material. Representative sections from regions around the penetration cavity were taken from the tested target by EDM to provide samples for metallography and scanning electron microscopy. Secondary and backscattered electron imaging were the primary analytical techniques utilized in the analysis. Quantitative and qualitative chemical analyses were performed via energy dispersion spectroscopy (EDS). Spectra of the various phases taken from the WHA and the XD™ Titanium aluminide composite were utilized as standard references for quantitative analysis of the impacted target material. Quantitative phase analysis was accomplished through measurement of areas in the backscattered images. Areal fractions of distinct components in the virgin target and penetrator materials were obtained as references for comparison to features observed in the post-mortem analysis. For example, the theoretical areal fractions of tungsten and matrix based on the alloy

chemistry were 83% W and 17% matrix. Measurements made on samples via automated image analysis showed identical respective areal fractions.

RESULTS AND DISCUSSION

The ballistic test of the 7.5XD material gave a resultant DOP, corrected for actual striking velocity, of 30.2mm. This is within 5% of the average DOP value for the AD90 alumina oxide at an equivalent areal density. Thus, the titanium aluminide composite has the same level of ballistic performance against this penetrator as the reference alumina. This similarity of performance is quite interesting, given the significant differences observed in macro- and microscopic failure morphology from aluminum oxide or other ceramic materials. Of course, the evidence of one ballistic test is certainly not conclusive. As detailed in the previous paper, however, results with similar materials having higher and lower amounts of reinforcement have shown equivalent behavior.²²

A frontal view of the (post-impact) target is shown in Figure 3; this view shows that the bulk of the material remained basically intact, in contrast to ceramic target plates, which undergo large amounts of cracking and generalized failure. Ceramics such as AD90 exhibit extensive damage in the form of radial cracking, ring cracking, and extensive comminution of material in the penetration zone. Some radial cracks have developed in the 7.5XD titanium aluminide plate, but they are limited in number and extent.

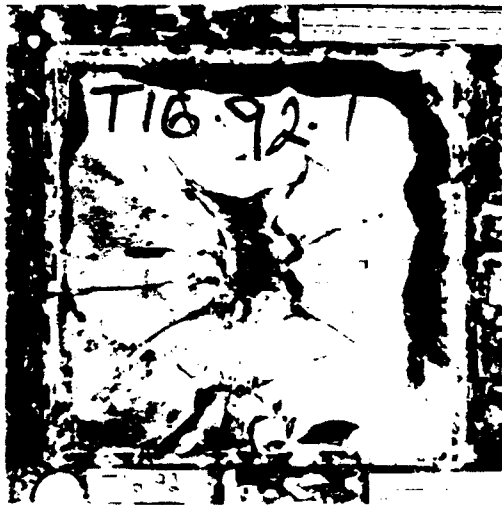


Figure 3. Frontal Surface of 7.5XD Ballistic Target

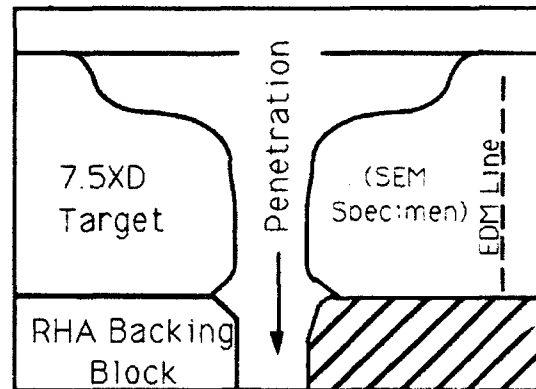


Figure 4. Schematic of Penetration Cavity Cross-Section

Macroscopic examination of a cross-section from the impacted target shows a shape in the affected material which roughly conforms to the features of a shallow champagne glass (see Figure 4). The failure mechanism for the target material in the immediate penetration zone is plastic yielding. Detail description of the deformed microstructure within the target material is described elsewhere⁴. In addition to microstructural evidence, plastic yielding of the target is also illustrated by the effective constraint which the 7.5XD IMC plate provided to the surface of the steel backup block. The degree of plastic flow at the top of the penetration cavity in the steel is minimal. This is a normal feature of penetration observed between interfaces in metallic materials which undergo ductile yielding, e.g. stacked steel plates. In ceramics, however, extensive fracture at late times due to accumulated damage from the penetration event makes the material along the interfacial region between the ceramic target and the semi-infinite steel block unable to support shear loading. Hence, it cannot provide an effective constraint to the steel block face, which responds much like a free surface and flows outward near the penetration cavity.

A reverse spallation phenomenon is evident in this target. Spallation is the term applied to the failure of a localized region in the target due to the tensile stress created on some plane within

the plate when a compressive shock wave reflects at an interface and propagates back into the target. The position of the spall plane is determined by material and geometric factors of the target. This phenomenon is often observed on the rear surfaces of ballistic test plates, where a ring or a disc of material is detached from around the penetration zone and ejected away from the rear of the plate. Preferential failure along the path of microstructural features such as the local flow regions along the rolling direction is commonly observed. In this test, the backplate constraint has suppressed the common mode of behavior, but sufficient tensile stresses are generated near the surface to cause detachment and ejection of material in a direction opposite to the penetration event. Examination of the failure surface shows that cracks propagate preferentially in the direction of particulate alignment developed by the axially symmetric forging process.

Secondary and backscattered electron imaging of the cross sectional area along the cavity wall in the stem region of the target reveal chunks of penetrator and target material amalgamated in the interaction medium (see •Figure 5a and 5b). Both the WHA and titanium aluminide composite chunks exhibit rounded features, with microstructures that otherwise correspond to their respective virgin material.

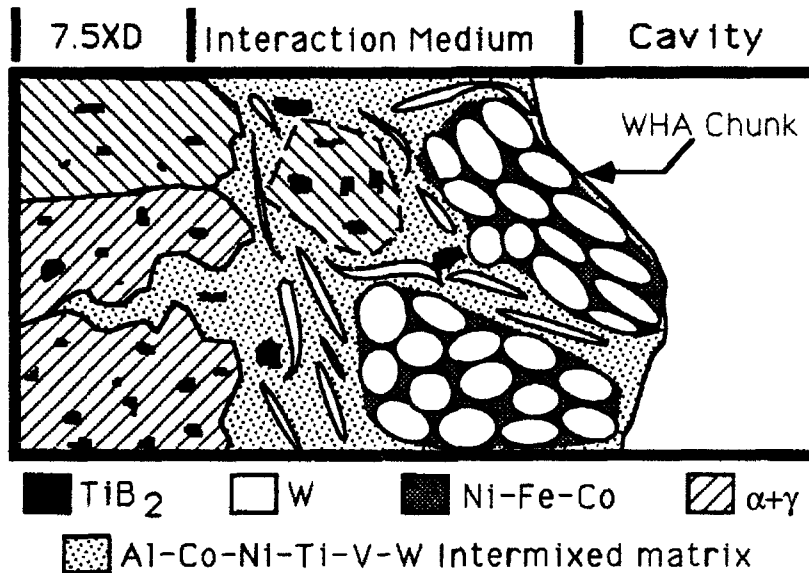


Figure 5a. Schematic of the Cavity Cross Section

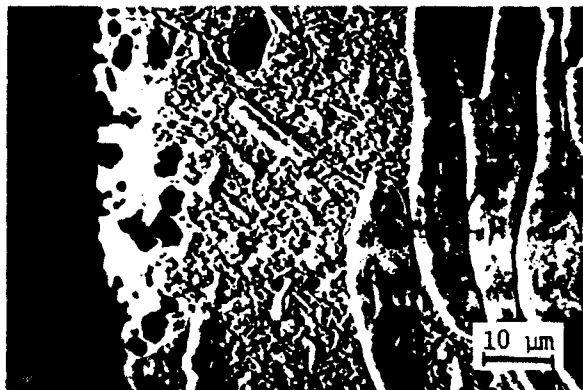


Figure 5b. SEI/BEI of Cavity Cross Section

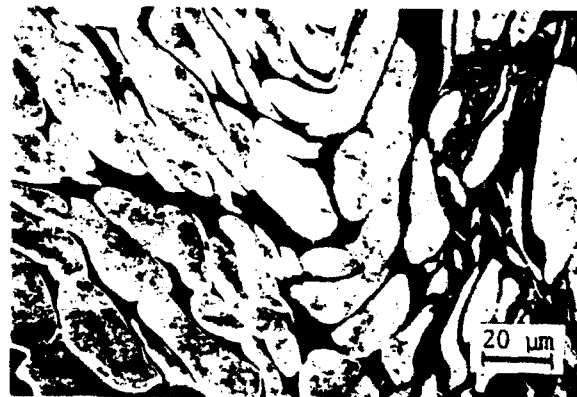


Figure 6. SEI/BEI of WHA chunk.

The WHA chunks composed of tungsten grains, display greater deformation than that of the virgin penetrator material (see •Figure 6). As is typical for a WHA, the tungsten grains are bound in a Ni-Fe-Co matrix. EDS analysis of the matrix discloses a composition with an identical Ni-Fe-Co ratio to that of the virgin WHA penetrator. The microstructure near the perimeter of each WHA chunk consists of further delineated tungsten grains, transitioning into the matrix of the intermixing medium. These WHA chunks are probably fragments eroded from the projectile during the penetration process.

Similar to the base 7.5XD, the titanium aluminide composite chunks contain TiB₂ particulates distributed in a lamellar structure of alternating γ -TiAl and α_2 -Ti₃Al layers. Unlike the target regions along the cavity wall, the composite chunks did not display any sign of plastic deformation nor any crack propagation into the material. The titanium aluminide composite chunks are probably fragments from the initial impact that have coalesced with the intermixed matrix during the penetration process.

The interaction medium appears to be a mixture of intermingled and bound WHA and the titanium aluminide composite fragments along the target sidewall (see Figure 7). In addition, the interaction medium has an intermixed matrix with submicron tungsten particles, shavings of tungsten, and TiB₂ particulates. The tungsten components in the intermixed matrix are analogous to those commonly found in interactions between penetrator material and steel targets. The ultra-fine tungsten particles may be evidence of a grinding or pulverization process. Similarly, the shavings of tungsten may be considered as having undergone a shearing or a severe extrusion-like process. These observations can be rationalized as results from the progressive erosion of a WHA rod penetrating the target.

The TiB₂ particulates are similar to those found in the composite matrix; however, the areal fraction of TiB₂ particulates in the characteristic medium is only 20% of that found in the intact 7.5XD IMC. Either the TiB₂ particulates uncoupled from the titanium aluminide composite, or the titanium aluminide matrix has simply transformed and diluted during the penetrator/target interaction process. The intermixed matrix consists of Al-Co-Ni-Ti-V-W. Qualitative EDS analysis reveals relative elemental consistency with both the penetrator matrix of Ni-Fe-Co, and the composite matrix of titanium aluminide. However, rather than a mechanical mixture of Ni-Fe-Co and the lamellar structure of γ -TiAl and α_2 -Ti₃Al, a solid solution of all the elements in their respective compositions is observed.



Figure 7. SEI/BEI of Interaction Medium



Figure 8. BEI of Materials from the Interaction Medium Incorporated Into Cracks

In addition, material from the interaction medium is also present in fine cracks that have propagated into the intermetallic composite target (Figure 8). This is evidence that the matrix of the characteristic medium has exhibited a fluid-like behavior during the penetration process. Perhaps the medium also acts as a bonding agent, which penetrates into cracks and fuses the local damaged area in the target material. If this conjecture is valid, it provides a unique method for preserving target integrity during ballistic penetration. Similar phenomena have been observed in other materials subjected to extreme hydrodynamic loading conditions. In order to account for the existence of this process, complete solutionization of the Ni-Fe-Co and the titanium aluminide must occur. A penetration-induced mechanical dissolution or melting process, aided by the large hydrodynamic pressures, may explain the hypothesized solutionizing process, as well as the rounded features found in the WHA and titanium aluminide composite chunks.

In summary, this XD™ TiB₂ reinforced titanium aluminide displayed ballistic performance comparable to that of an alumina armor ceramic. The titanium aluminide composite did not shatter nor pulverize like a ceramic, but maintained its integrity, with a relatively narrow penetration cavity. Microscopic post-mortem analysis of the penetration cavity walls revealed the existence of

nor pulverize like a ceramic, but maintained its integrity, with a relatively narrow penetration cavity. Microscopic post-mortem analysis of the penetration cavity walls revealed the existence of an interaction medium composed of all the constituents from the WHA penetrator and the titanium aluminide composite target. The intermixed matrix is thought to be an interaction product of hydrodynamic conditions experienced by the penetrator and the target during the penetration process. A fluid-like behavior of the medium is evident from the microscopic analysis. The interaction medium may play some role in the erosion of the penetrator as well as healing the target. The dynamic temperature and pressure associated with this phenomenon and the role of the interaction medium in ballistic penetration will be the subject for future study.

CONCLUSIONS

- Post-mortem analysis of the target cavity revealed fragments of highly deformed WHA bonded to the titanium aluminide composite wall through a interfacial reaction zone.
- The interfacial reaction zone composed of "shavings" and ultra-fine particles of tungsten from the penetrator, titanium diboride particulates from the target material, and an intermixed matrix solution of Al-Co-Fe-Ni-Ti-V-W.
- The relative chemical proportions within the intermixed matrix solution was consistent with the contributions from the metallic Ni-Fe-Co WHA matrix and the intermetallic titanium aluminide XD™ composite matrix.
- Microstructural features exhibited in the penetrator/target interfacial reaction zone suggest a fluid-like interaction due to the localized hydrodynamic environment during the penetration process between the WHA and the XD™ titanium aluminide composite.
- Materials from the interaction medium infiltrated into fine cracks in the titanium aluminide composite target. This observation was evidence of a healing process which apparently had an influence in maintaining target integrity during and after projectile penetration.

ACKNOWLEDGMENTS

The authors would like to thank the many people who have contributed to this effort. They would like to particularly thank Dr. C. Robert Crowe of the Naval Research Laboratory and Dr. Steven Kampe of Martin Marietta Laboratories for providing the materials used to perform this study as well as much background information on the characteristics of these materials. They appreciate the valuable technical consultations given by Mr. John Nunes and Mr. George Schmidt.

1. G. Pageau, in *Proc. 23rd International SAMPE Technical Conference*, (Oct 1991), p. 639-649.
2. S.J. Bless et al., "Ballistic Impact Behavior of SiC Reinforced Aluminum Alloy Matrix Composites", technical report to be published, (1992).
3. E.Chin, J. Morgan, and F. Tuler, AMTL TR 90-49, (Oct 1990).
4. E. Chin and P. Woolsey, in *Proc. 16th Army Science Conference*, Jun 1992.
5. H. Lipsitt, in *MRS Symp. Proc.*, Vol. 39, (1985), p. 351-364.
6. S. Ashley, *Mech. Eng.*, Dec, Vol. 49, (1991).
7. J.M. Brupbacher, L. Christodoulou, D.C. Nagle, U.S. Patent No. 4,710,348; U.S. Patent No. 4,772,452.
8. D.C. Nagle, J.M. Brupbacher, L. Christodoulou, U.S. Patent No. 4,774,052; U.S. Patent No. 4,916,029.
9. E. Chin and P. Woolsey, in *Proc. 16th Army Science Conference*, Jun 1992.
10. Y. Kim and D.M. Dimiduk, *JOM*, Aug, Vol. 40, (1991).

-
- 11 L. Christodoulou, P.A. Parrish, and C.R. Crowe, in *MRS Symp. Proc.*, Vol. 120, (1988), p. 29-34.
 - 12 D.E. Larsen, S. Kampe, and L. Christodoulou, in *MRS Symp. Proc.*, Vol. 194, (1990), p. 285-292.
 - 13 E. Robertson and P.L. Martin, in *MRS Symp. Proc.*, Vol.194, (1990), p. 233-240.
 - 14 Steven Kampe, 1992, Martin Marietta Laboratories, private communication.
 - 15 E. Chin and R. Biederman, AMTL TR 92-47 (July 1992).
 - 16 R.J. Dowding et al., AMTL TR 90-31 (Apr 1990).
 - 17 P. Woolsey et al., in *Proc. 1st International Symposium on Tungsten and Its Alloys*(1992).
 - 18 V. Hohler and A.J. Stilp, in *Proc. 3rd Intl. Symp. on Ballistics*(1977).
 - 19 C. E. Anderson Jr. and J. D. Walker, *Int. J. Impact Eng.*, Vol. 4, 1991, p. 481.
 - 20 P. Woolsey, S. Mariano, D. Kokidko, AMTL TR 89-43 (Apr 1989).
 - 21 P. Woolsey, AMTL TR 92-28 (Apr 1992).
 - 22 E. Chin and P. Woolsey, in *Proc. 16th Army Science Conference*, Jun 1992.

QUASISTATIC AND DYNAMIC PROPERTIES OF TUNGSTEN HEAVY ALLOYS WITH L₁₂ INTERMETALLIC MATRICES

S. Guha, C. Kyriacou, J.C. Withers, R.O. Loutfy
Materials and Electrochemical Research (MER) Corp.,
7960 S. Kolb Rd, Tucson AZ 85706

G.T. Gray III
Materials Research and Processing Science, MST-5,
Los Alamos National Laboratory, Los Alamos NM 87545.

R.J. Dowding
Army Research Laboratory, Materials Directorate
AMSRL-MA-MB, Watertown MA 02172-0001.

ABSTRACT

The superior ballistic penetration behavior of Depleted Uranium (DU) alloys compared to W-Ni-Fe heavy alloys (WHA) has been attributed to a self-sharpening behavior in DU where failure occurs along adiabatic shear bands. Since adiabatic shear represents a plastic flow instability condition between competing processes of thermal softening and work-hardening, cracking along these bands will occur more readily if the matrix were to harden (decreased ductility) with increased temperature along these shear bands. While conventional materials exhibit decreasing strength and increasing ductility with increasing temperature, certain L₁₂-structured intermetallic materials exhibiting positive temperature dependence of strength and negative temperature dependence of ductility should be susceptible to failure along shear bands. L₁₂ structured intermetallic such as Ni₃Al and L₁₂+f.c.c intermetallic Ni-12Al-40Fe(at.%) exhibit such 'anomalous' behavior as decreased ductility and increased strength with increasing temperatures. Hence, tungsten heavy alloys that utilize such intermetallic matrices exhibit potential to fail along adiabatic shear under high strain rate conditions. Heavy alloys with different weight fractions of tungsten and types of intermetallic matrix were processed by a liquid phase sintering approach. Such heavy alloys exhibit significantly increased (with respect to conventional heavy alloys) flow stress levels during high strain rate testing and shear localization; the heavy alloy with Ni-Fe-Al L₁₂/fcc matrix also failed along these shear bands.

INTRODUCTION

In recent years, the use of thicker armor have prompted the designers of anti-armor munitions to increase the energy density at the target. Among materials with densities greater than 15g/cc, only two types of materials namely Tungsten Heavy Alloys (WHA) and Depleted Uranium (DU) are commonly utilized. DU and WHA are two different kinds of materials. The microstructure of U-0.75Ti is a lenticular martensitic structure where an aging treatment (16hrs/360°C or 4hrs/385°C) precipitates an intermetallic U₂Ti which both strengthens the alloy and reduces its ductility. The typical quasi-static tensile 0.2% yield strength, ultimate strength and ductility of this alloy after aging are, respectively, 1100MPa, 1600 MPa and 12% elongation [1]. In contrast to DU alloys, WHA are in-situ composites and consist of essentially pure W particles, 30-60µm in diameter, in a matrix of Ni, Fe and dissolved W. While WHA lack any precipitation hardening mechanisms like DU alloys, cold-working is used to develop various combinations of strength and ductility. In a 20%

swaged state, the typical quasi-static tensile strength and ductility of a 97wt.%W-balance Ni, Fe, Co alloy are, respectively, $\approx 1200\text{MPa}$ and 4% [2].

The process of penetration of a target by a projectile consists of the penetrator being consumed as it burrows into the armor, 'back-extruding' from the penetrator-target interface while the interface moves forward into the target. For penetrators of equivalent geometry (L-to-D ratio = 20) and mass (65 gms) penetrating a semi-infinite Rolled Homogeneous Armor (RHA) steel target, DU penetrators were observed to perform better than WHA with 93wt.% W [2]. An alternate method of judging the relative penetration capability is the determination of limit velocities where the velocity of a 65 gm projectile that will just perforate a 3" (75mm) thick RHA plate is measured; this limit velocity was $\approx 100\text{m/s}$ lower for DU projectiles than WHA [2]. While increasing strength and hardness of DU improved penetration capability, similar changes in mechanical properties of WHA exerted only mild influence on the penetration performance (only an increased density was helpful [3,4]). X-ray radiographic images of the target-penetrator interface taken during the penetration process show less mushrooming for DU projectiles [5]. The improved performance was attributed to a lower work-hardening rate for DU alloys (during dynamic loading) which itself is in contrast to very high work-hardening rates during quasi-static loading [6]. Alternate suggestions include formation of low melting point U-Fe intermetallics which act as a lubricant at the target-penetrator interface allowing easier defeat of target [7].

While the performance gap between DU and WHA cannot be easily explained by differences in conventional mechanical properties, they do exhibit differences in penetration behavior. For example, while the DU alloys retain a chisel-nose after penetration, the WHA usually retain a mushroom head on the back side of the armor. The chisel-nose appearance has been related to deformation being localized in adiabatic shear bands while the large mushroom head is related to extensive plastic deformation in WHA before localization of deformation and discarding of back-extruded material. The strength of WHA appears to exert minimal influence on the penetration performance. Replacing the Ni-Fe matrix with Ta resulted in further degraded performance (25-30m/s higher limit velocity) and no localization of plastic flow was observed [8]. Similarly, a U-6%Nb penetrator which exhibited bulk plastic deformation but no localized flow led to reduced penetration performance in relation to U-0.75Ti penetrators; the limiting velocity of U-6%Nb penetrators was similar to that of equidensity WHA [9]. These results are strongly indicative of the superior ballistic performance being related to failure by localized deformation [2].

The formation of adiabatic shear bands represents an instability condition between the competing processes of work-hardening and thermal softening. At high strain rates ($> 10^2\text{s}^{-1}$), beyond a critical strain [10], deformation can be limited to narrow bands termed adiabatic shear bands (where the conversion of strain energy into heat raises the temperature of material in these bands). Failure along these bands occurs when thermal softening is dominant over work-hardening and significant strain has been accumulated within these bands. Conventional heavy alloy matrices which exhibit increasing ductility with increasing temperature, can often resist the failure process along these bands. By contrast, materials that exhibit decreased ductility with increasing temperature should be more susceptible to failure along these shear bands thereby enhancing the chance of a self-sharpening behavior. Some L_{12} -structured intermetallics such as Ni_3Al exhibit such a high temperature embrittlement [11]. However, Ni_3Al also exhibits high quasi-static work-hardening rates and sharply positive dependence of yield strength on temperature. By

contrast, certain Ni-Fe-Al intermetallics (with a dispersion of $L1_2$ precipitates within a fcc matrix, see Figure 1a [12]) exhibit high temperature embrittlement, low work-hardening rates during quasi-static deformation and a gradual negative strength dependence on temperature, see Figure 1b [12]. In addition, plastic deformation within these intermetallics occurs primarily by paired APB-coupled superlattice dislocations on $\{111\}$ planes which leads to planar slip [11]; the planar nature of deformation may lead to shear localization along the preferred deformation planes. Thus, it would be interesting to examine the high strain rate properties of WHA based on these intermetallic matrices.

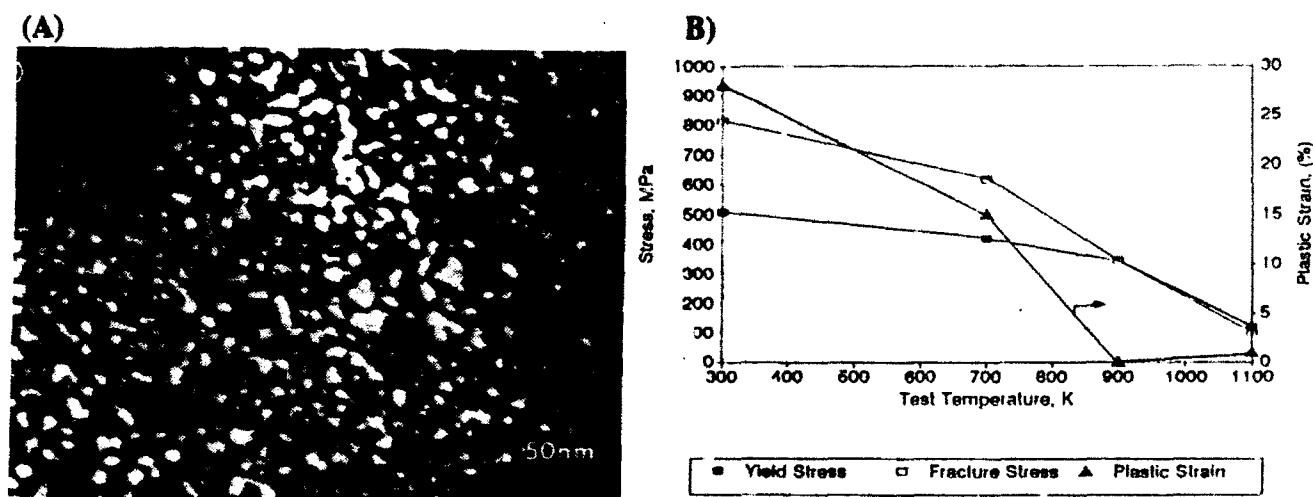


Figure 1. (a) $\{001\}$ Superlattice dark-field image of Ni-12Al-40Fe(at.%) showing a dispersion of ≈ 10 nm sized $L1_2$ precipitates (bright contrast) within a disordered (dark) fcc matrix. (b) Variation of ductility, yield strength and fracture stress with temperature for Ni-12Al-40Fe (at.%). (From [12]).

EXPERIMENTAL TECHNIQUES

The tungsten powder (AESAR/Johnson Matthey) used had an average particle size of 0.6 microns, surface area of $1.5\text{m}^2/\text{g}$ and a purity of 99.9%. The as-received intermetallic powders of compositions Ni-24at.%Al-0.2at.%B and Ni-12at.%Al-40at.%Fe (custom made by Atlantic Equipments and Engineers, NJ) had a particle size range of 5-100 μm ; finer particle sizes with a narrower particle size distribution were obtained by ball milling and sedimentation in a solvent medium. The W and intermetallic powders for liquid phase sintering were wet mixed in isopropyl alcohol with a surfactant (SOLSPERSE 24000) added to aid in powder dispersion. The dried powder mixtures were compacted in a stainless steel die at 200 MPa pressure. Sintering was performed in a graphite element furnace at temperatures between 1475°C and 1575°C for 15-30 minutes depending upon alloy type and matrix content. A dry hydrogen atmosphere was maintained during the heat-up and half-way through the soak of the sintering schedule and then switched to dry Argon.

Flat rectangles of size 50mm x 25mm x 2.5mm were sintered for mechanical testing. Shrinkages during sintering were of the order of 20%. Sintered densities of the specimens measured as per ASTM C373-72 standard were in the range of 97-99% of theoretical. For each composition, two dog-bone shaped flat tensile specimens with gage dimensions of 8.75mm x 3.45mm x 1.5mm were machined using EDM, polished, annealed at 750°C for 2 hours in vacuum and tested using an initial strain rate of $\approx 1 \times 10^{-4}/\text{sec}$. High strain rate

($\approx 5000\text{s}^{-1}$) compression tests were performed using a Split Hopkinson Pressure bar utilizing right circular cylindrical specimens (as-sintered), 4.6mm in diameter with a L-to-D ratio of 1.4. The flat sides were ground parallel to 0.0025mm and lubricated during testing.

Microstructural analysis of the as-sintered and tensile-tested specimens was done using a scanning electron microscope (SEM). Semi-quantitative compositional analysis of microstructural features was performed using an x-ray analyzer (EDAX) and phases identified using a SCINTAG x-ray diffractometer equipped with a solid-state detector.

RESULTS

The microstructure of the heavy alloys with 7 wt.% matrix (Ni_3Al and Ni-12Al-40Fe , henceforth referred to as NiFeAl) are shown in Figure 2. The as-sintered microstructure consists of roughly spherical grains of nearly pure W, $\approx 25\mu\text{m}$ in diameter, within the intermetallic matrix. X-ray diffraction identified W and the intermetallic as the predominant phases; the intensity of the superlattice peaks are considerably reduced presumably the result of dissolved tungsten (W sitting on Al sites would increase the atomic scattering factors of Al sites thereby diminishing the intensity of superlattice peaks), however, a weak $\{110\}$ peak is still visible, see Figure 3. A small volume fraction of additional phases (arrowed in Figure 2) was observed at the W-matrix interfaces. The microstructure of the as-sintered WHA with 7% or 10% Ni-Fe matrix (8:2 weight ratio) did not indicate the presence of such phases indicating that such phases were probably related to the presence of Al in the matrix; compositional measurements using EDS indeed suggested that such phases were Al-rich. X-ray diffraction, however, identified $\text{Ni}_2\text{W}_4\text{C}$ as one of the likely phases (see Figure 3) although the identification is not definite due to overlap with strong W peaks. Compositional measurements using a microprobe, however, indicated that both Al-rich (with dissolved Ni and W) and carbon containing phases were present; such C-based phases would not be identifiable in a SEM because of their low atomic number. The microstructures of heavy alloys with higher and lower matrix weight fractions were qualitatively similar to those described above.

Quasi-static tensile tests were performed at room temperature and the results are listed in Table I. The Rockwell hardness values listed in Table I represent an average of three measurements. The engineering stress-strain curves are shown in Figure 4. The alloys containing the L_{12} matrix (Ni_3Al or Ni-12Al-40Fe) exhibit an increase in UTS as the matrix fraction increased from 5 wt% to 7wt%. An increase in matrix fraction from 7wt% to 10wt%, however, shows little improvement in UTS or ductility for the Ni_3Al -based heavy alloys. Also, for similar weight fractions of matrix, the heavy alloys with Ni-12Al-40Fe matrix exhibited lower yield strength but similar (or possibly slightly higher) UTS than those with Ni_3Al matrix. This is evident in the UTS, YS and elongation data. The conventional heavy alloys containing 7% and 10% (8Ni + 2Fe) matrix were tested primarily for comparison purposes. These samples showed much higher UTS and elongation but slightly lower yield strengths. It is worthwhile noting that the alloys containing NiFeAl matrix exhibited higher tensile elongation than those containing Ni_3Al matrix. The lower ductility of $\text{W} + 10\%\text{NiFeAl}$ than $\text{W} + 7\%\text{NiFeAl}$ is attributable to microstructural flaws (pores). Overall the alloy composition $\text{W} + 7\% \text{NiFeAl}$ showed the best mechanical behavior among the L_{12} -based heavy alloys.

Table I: Summary of Tensile Test Results of W-Heavy Alloys

Sample Composition	Density (g/cc) (% theoretical)	UTS (MPa)	Yield Strength (MPa)	Elong. (%)	Hardness (Rc)
W + 5% Ni ₃ Al	17.39 (96.7)	545	-	0	36
	17.31 (97.2)	552	-	0	
W + 7% Ni ₃ Al	16.96 (97.5)	724	649	1.3	35
W + 10% Ni ₃ Al	16.45 (98.7)	740	685	1.2	37
	16.43 (98.5)	718	656	1.1	
W + 5% NiFeAl	17.46 (97.6)	406	-	0	34
	17.59 (98.3)	517	-	0	
W + 7% NiFeAl	17.01 (97.8)	762	590	5.3	34
	17.14 (98.5)	758	595	3.9	
W + 10% NiFeAl	16.34 (98.0)	670	581	2.2	33
	16.32 (97.9)	674	551	2.4	
W + 7% (8Ni + 2Fe)	17.54 (98.7)	908	567	15.5	34
	17.67 (99.4)	840	609	8.3	
W + 10% (8Ni + 2Fe)	17.10 (99.4)	932	620	16.6	34
	16.99 (98.8)	932	613	18.6	

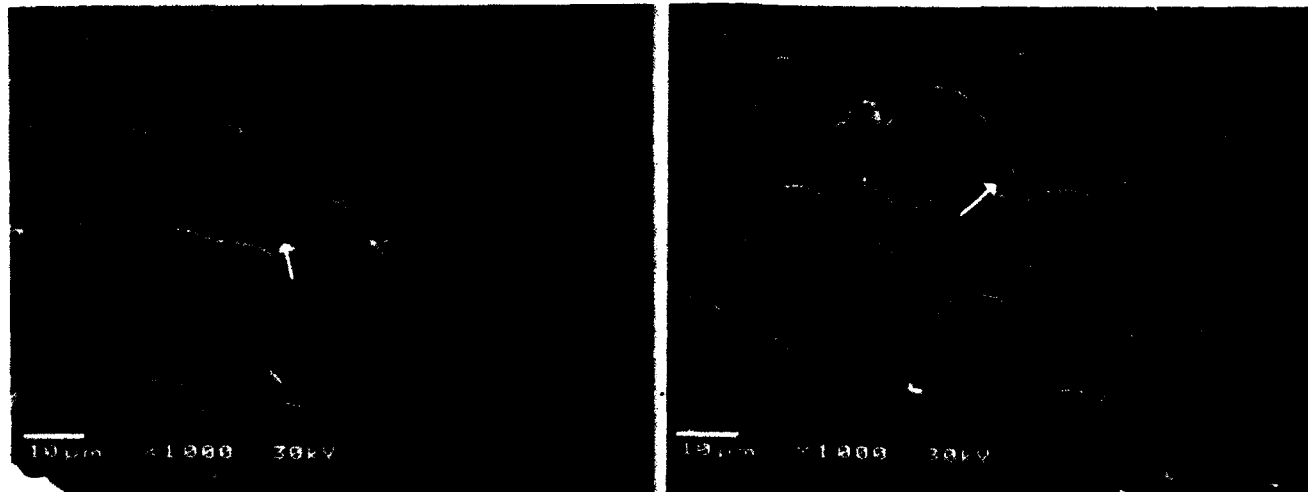


Figure 2. As-sintered microstructure of (a) W+7%Ni₃Al (b) W+7%(Ni₄₀Al₁₂Fe₄₈).

The fracture surfaces of WHA tensile specimens were examined and only the fractographs for 93%W+7%matrix specimens are shown in Figure 5. Comparing the fracture surfaces of heavy alloys based on Ni₃Al matrix, it was clear that for alloys containing only 5% matrix, failure was by separation between and by cleavage cracks in the W grains. By contrast, the alloys with 7 and 10wt% matrix exhibit evidence of plastic tearing in the matrix which is indicative of the intrinsic ductility of the intermetallic matrix. A large number of small (1-2 μ m diameter) particles are also observed on the fracture surfaces which are believed to be the dark particles observed during microstructural analysis

of these heavy alloys (see Figures 2). Compared to the Ni₃Al-based WHA, those based on the intermetallic Ni-12Al-40Fe exhibit evidence of considerably higher ductility as seen by the size of the dimples encircling the W grains (these are comparable to the dimples in the conventional WHA based on a Ni-Fe matrix).

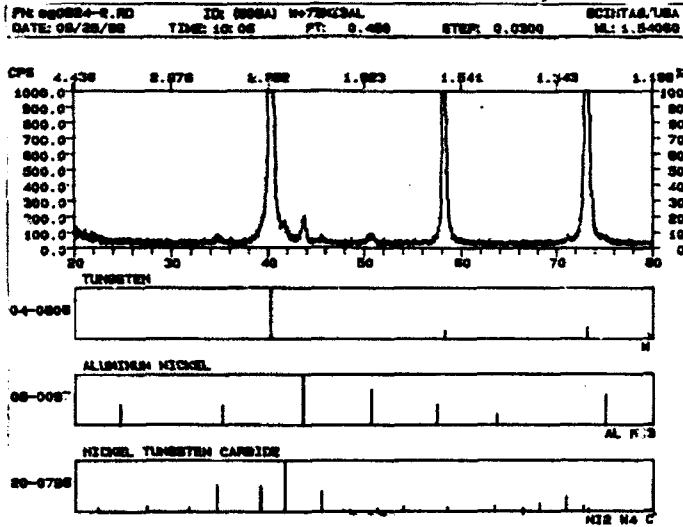


Figure 3. X-ray diffraction pattern from W+7% Ni₃Al composite.

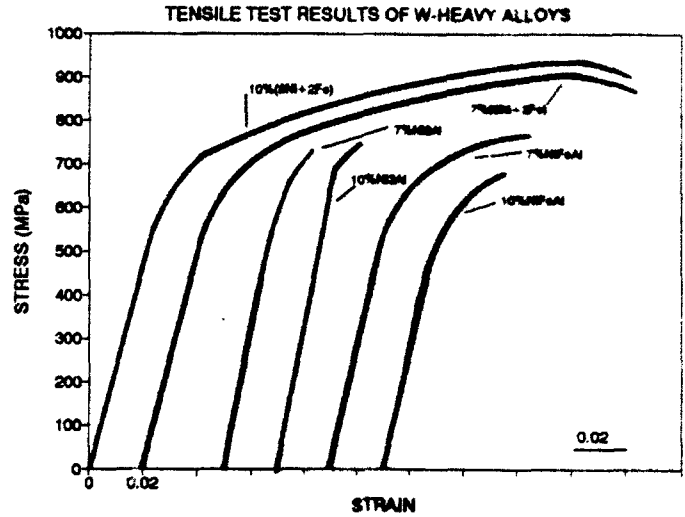


Figure 4. Quasistatic stress-strain curves for W-Ni₃Al and W-Ni₄₈Al₁₂Fe₄₀.

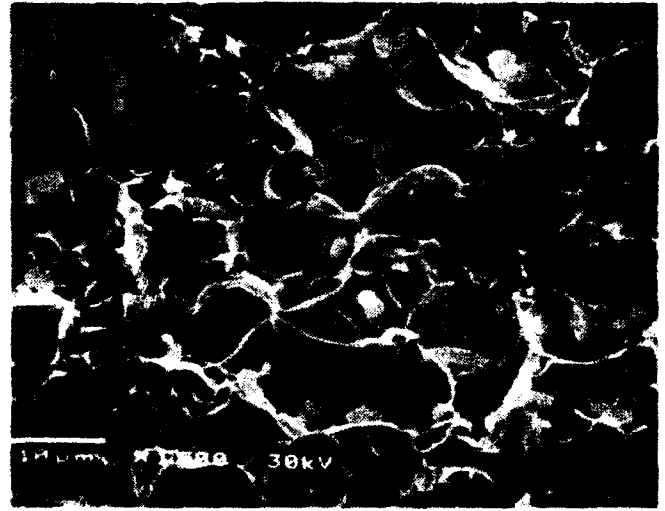
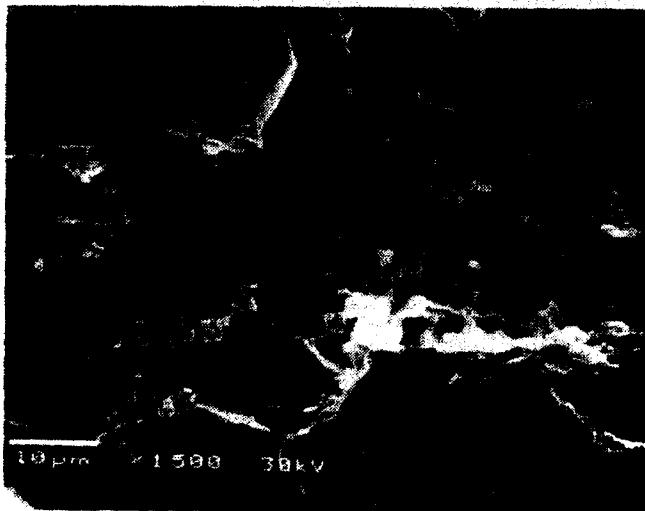


Figure 5. Fractographs of (a) W+7%Ni₃Al (b) W+7% Ni₄₈Al₁₂Fe₄₀.

The flow stress curves at high strain rates ($\approx 5-8 \times 10^3 \text{ s}^{-1}$) for the intermetallics Ni₃Al and Ni-12Al-40Fe and as-sintered heavy alloy composites W+7%Ni₃Al, W+10%Ni₃Al, W+7%NiFeAl and W+10%NiFeAl are shown in Figure 6. The specimens W+7%Ni₃Al and W+7%NiFeAl were hit harder (5" striker bar, 35psi pressure) than the other specimens (3" bar, 20psi pressure) to observe shear localization behavior in these alloys. The flow stress levels are considerably higher than those obtainable in conventional as-sintered WHA. Increasing W weight fractions lead to increased strength. Further, the heavy alloys based on NiFeAl matrix are stronger than those based on Ni₃Al. The most noteworthy feature of these flow stress curves is the high rate of work-hardening in these intermetallics; the rate of work-hardening decreases in the W composites. Further, the rate of work-hardening is lower in the W+7%NiFeAl composite than the W+7%Ni₃Al composite. The hard-hit

W+7%Ni₃Al composites exhibit a plateau in flow stress (≈ 2500 MPa) @ 24% true strain indicating that shear localization may have been initiated, however, the specimen did not fail. By contrast, the W+7%NiFeAl exhibited a plateau in flow stress (2600 MPa) @ $\approx 15\%$ strain and the specimen failed after a total strain of 22%. Figure 7a shows the polished longitudinal section in the W+7% Ni₃Al composite where the elongated W grains within a narrow ($\approx 50\mu\text{m}$ thick) band indicate the initiation of shear localization. Note that the shear band is $\approx 45^\circ$ to the original stress axis. Figure 7b shows the failed W+7%NiFeAl specimen where the failure surface is approximately at 45° to the stress axis indicating that in this case, the specimen failed along the shear band. The higher ultimate flow stresses and smaller failure strains of the W+7%NiFeAl specimen is in sharp contrast to the lower ultimate flow stresses and significantly higher failure strains observed in conventional WHA.

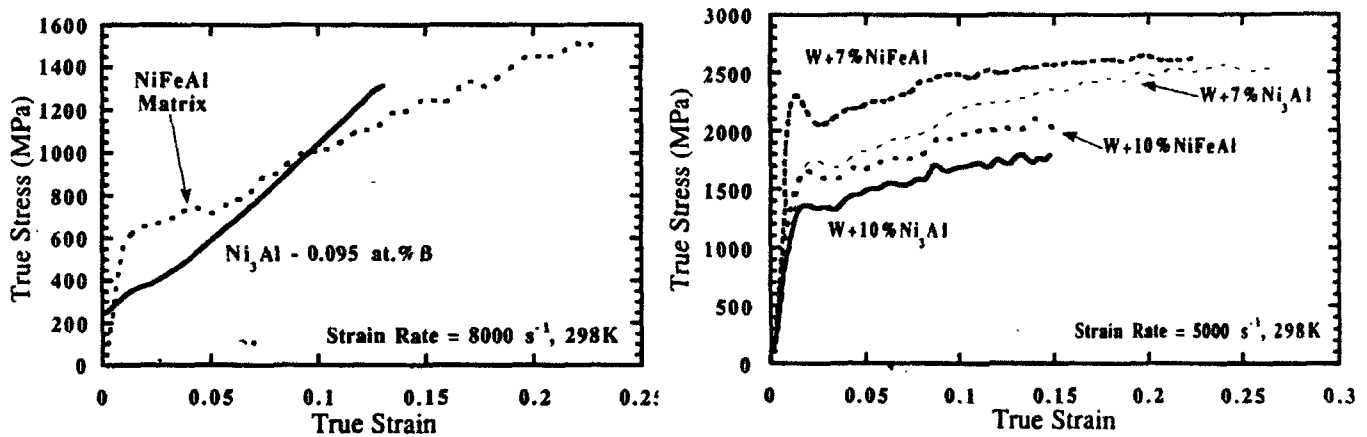


Figure 6. High strain rate compression tests for (a) L1₂ intermetallic matrices (b) intermetallic-based W heavy alloy composites. Data for Ni₃Al-0.095%B after Sizek and Gray [13].

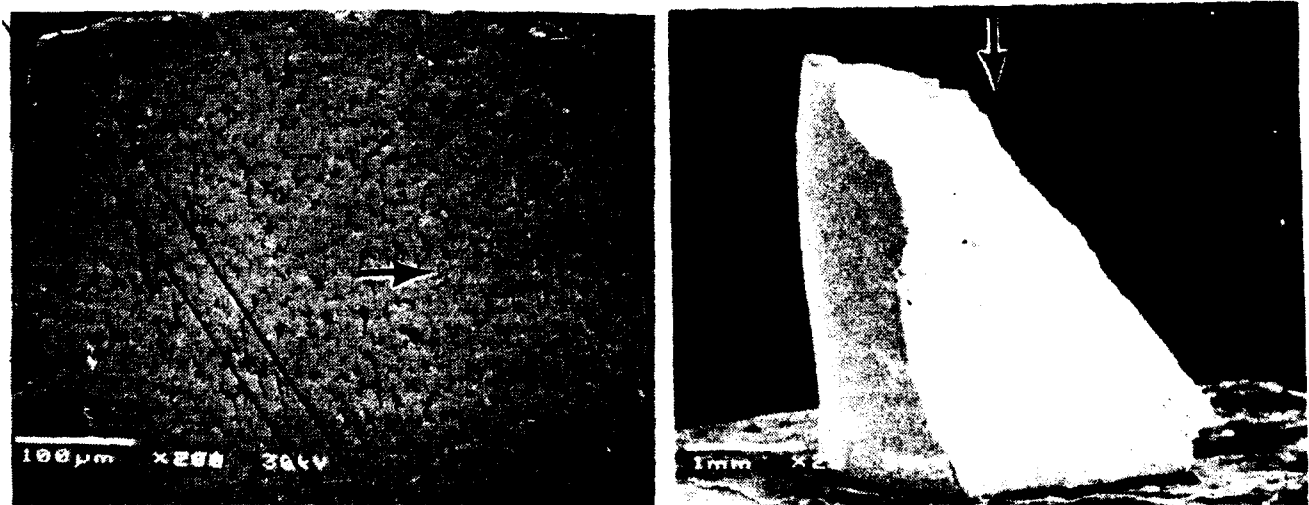


Figure 7. (a) Dynamic shear localization in W+7%Ni₃Al (b) Dynamic failure in W+7%(Ni₄₈Al₁₂Fe₄₀). Arrows indicate stress axis.

DISCUSSION

Bose, Couque and Lankford [14] have recently reported the high strain rate flow behavior of as-sintered WHA based on Ni-Fe and Ni-Co matrices. The peak flow stresses

for intermetallic-based WHA (≈ 2500 and 2600 MPa respectively for $W+7\%Ni_3Al$ and $W+7\%NiFeAl$) are ≈ 700 MPa higher than the peak flow stresses obtainable in as-sintered conventional WHA. Further, the flow stresses are either similar or ≈ 100 MPa higher than those reported for 25% swaged $W+9\%(Ni-Co)$ heavy alloy. Although the shear instability initiated at $\approx 15-20\%$ true strain, these conventional heavy alloys typically endured $\approx 40\%$ strain prior to failure. By contrast, shear instability initiated at $\approx 20\%$ strain in the $W+7\%NiFeAl$ composite and failure occurred at $\approx 22\%$ strain. Since these $L1_2$ intermetallics are known to exhibit a high temperature embrittlement, the quick failure is probably related to the ensuing high temperature embrittlement along adiabatic shear bands. It is interesting to note that the $W+7\%NiFeAl$ alloy also exhibits $\approx 5\%$ tensile elongation which may be adequate for thermo-mechanical processing and projectile launching considerations. This unique combination of reasonable quasi-static and excellent dynamic properties for NiFeAl based WHA indicates that such alloys indeed should be investigated further as viable replacement candidates for DU as kinetic energy penetrators.

The critical strain for shear localization is smaller for composites with lower work-hardening rates, consistent with the relationship of Staker [10]. From the flow stress behavior of matrices and W composites, it appears that the rate of work-hardening in the W composite is related to that for the matrix material itself; matrices with higher work-hardening rates (e.g. Ni_3Al compared to NiFeAl) impart higher work-hardening rate to the composite. The lower dynamic work-hardening rate of Ni-12Al-40Fe compared to Ni_3Al (B doped) is similar to its quasi-static characteristic. This difference in work-hardening, in turn, may be related to the microstructure and operating deformation mechanisms. While the microstructure of Ni_3Al is single phase, the alloy Ni-12Al-40Fe is two-phase, consisting of a dispersion of $L1_2$ -structured $(Ni,Fe)_3(Al,Fe)$ in a fcc (Ni,Fe,Al) matrix. It is possible that the higher resistance to flow offered by Ni_3Al may be related to the high APB energy on the primary deformation plane which would prevent these dislocations from operating individually or due to the splitting of superpartials into Shockley partials; cross-slip would then require re-combination of these Shockley partials and would lead to Kear-Wiltsdorf locks thereby further increasing the flow stress required to carry on deformation. By contrast, deformation in the two-phase alloy may be concentrated in the fcc matrix and proceed either by shearing of the intermetallic precipitates or passage of APB-coupled dislocations within the weakly ordered precipitates; the addition of Fe to Ni_3Al lowers the APB energy, hence the spacing between superpartials in Ni-12Al-40Fe is greater than in Ni_3Al , hence, deformation may proceed by cross-slip of single dislocations.

Bose et al.[14] have indicated the importance of matrix stoichiometry in promoting shear localization; a 7:3 rather than 8:2 ratio of Ni:Fe was found to be more susceptible to shear localization and cracking along shear bands despite their similar stress-strain behavior. Further, an inhomogeneous microstructure and swaging were shown to be favorable to shear localization. It is postulated that the residual dislocation density acts as a trigger to shear localization and cracking. Thus, similar to the conventional WHA discussed above, for WHA based on $L1_2$ intermetallic matrices, thermomechanical processing may be utilized to increase the residual dislocation density (reduce the rate of work-hardening) further thereby leading to initiation of shear localization at lower strains.

In summary, the present investigation suggests that ternary alloying elements such as Al affect the shear localization properties in WHA matrix either due to a compositional effect (similar to that of Ni-Fe ratios discussed by Bose et al.[14]) or a microstructural effect

where an ultrafine dispersion of $L1_2$ phase in fcc matrix leads to shear localization).

CONCLUSIONS

1. W heavy alloys based on $L1_2$ intermetallic matrices exhibit significantly improved ultimate flow stress levels compared to conventional heavy alloys in an as-sintered condition.
2. Shear localization in high strain rate tests was observed in W composites based on both Ni_3Al and Ni-12Al-40Fe matrices; failure along shear bands occurred only in W+7wt.%(Ni-12Al-40Fe) composite.
3. The composite W+7%(Ni-12Al-40Fe) exhibited the best combination of quasi-static and dynamic mechanical and shear localization properties.

ACKNOWLEDGEMENTS

The authors would like to acknowledge the assistance of Mr. I. McGregor, Mr. K. Anderson, Mr. T. Nguyen and Mr. W. Kelly for experimental work in this program. The use of the Dynamic Test facility at Los Alamos National Laboratory is also gratefully acknowledged. This research was funded by a SBIR Phase I program from US Army Materials Technology Laboratory, Watertown, MA under contract no. DAAL04-92-C-0009.

REFERENCES

1. T. Nicolas, Dynamic Tensile Testing of Structural Materials using Split Hopkinson Bar Apparatus, AFWAL-TR-80-4053 (1980).
2. L. Magness, Deformation Behavior and its Relationship to the Penetration Performance of High Density KE Penetrators, (Preprint).
3. "The Metallurgical and Ballistic Characterization of Quarter-Scale Tungsten Alloy Penetrators", R.J. Dowding, K.J. Tauer, P. Woolsey and F.S. Hodi, US Army Materials Tech. Lab, Watertown MA, MTL TR 90-31, May 1991.
4. Performance-Property Relationships in Tungsten Alloy Penetrators, P. Woolsey, F.S. Hodi, R.J. Dowding and K.J. Tauer, these proceedings.
5. L.W. Hantel and J.W. Taylor, PHERMEX Evaluation of Air Force Tungsten and U-0.75%Ti Penetrators (U), Los Alamos National Lab Report LA-5658.
6. L. Magness, Materials for Kinetic Energy Projectile Applications, Proc. 28th NATO DRG Seminar on Novel Materials for Impact Loading, Bremen, Germany.
7. D. Sandstrom, P. Dunn and W. Hogan, Comparison of Tungsten and Uranium Kinetic Energy Penetrators Fired Into Semi-Infinite Steel Targets", Proc. Tungsten Ordnance Tech. seminar, Washington DC (1986).
8. E. Foster et al., Penetration of Ballistic Test Specimens from Ta-coated W Powders, Batelle, Columbus, Contract Rep. to BRL.
9. F.J. Fulton, C.F. Cline and E.O. Snell, Penetration of Mild Steel targets by High Density Long-Rod Penetrators, Lawrence Livermore Lab rep., UCRL-52991.
10. M.R. Staker, Acta Met., 29 (1981) 683.
11. N.S. Stoloff, Int. Met. Rev., 34 (1989).
12. Sumit Guha, PhD Thesis, Dartmouth College, 1992.
13. H.W. Sizek and G.T. Gray III, Acta Metall., (1992) in press.
14. A. Bose, H. Couque and J. Lankford Jr., Paper Presented at 1992 World Congress MPIF, San Fransisco.

DYNAMIC SHEAR TESTING OF TUNGSTEN BASED COMPOSITES

Murray Kornhauser
3C Systems
Wynnewood, PA 19096

and

Robert J. Dowding
U.S. Army Research Laboratory
Watertown, MA 02172-0001

The objectives of this Phase I SBIR Program were to develop the test facility for very high strain rate shear testing of composite tungsten materials for use in kinetic energy (KE) penetrators, and to conduct shear tests with some promising tungsten composites in order to determine whether these test samples exhibit properties favorable for KE penetrators (1).

An electromagnetic stress wave generator, with its output augmented with a conical Hopkinson bar, was used to drive a half-inch diameter hardened steel punch through tungsten composite samples 1/16 inch thick and one-inch diameter. Figure 1 is a sketch of the Electromagnetic Hopkinson Bar in its shear test configuration.

The electromagnetically-generated compressive stress wave in the conical bar projects the steel punch at high velocity against the tungsten alloy (or composite) test sample, with the velocity depending on the kilovolt input to the coil, as shown in Figure 2. When the steel punch strikes the tungsten, high pressure stress waves are generated in the target plate. Note in Figure 3 that the impact stress waves generated by a flat-face punch could destroy a test sample when the waves reflect in tension from the rear face of the sample, if the stress wave intensity exceeds the material strength. In this test series, however, only one or two samples were tested with inputs above 3 kilovolts, and these tests were conducted with slant-faced punches.

Figure 4 shows the relationship between shear strain rate, using the steel punch with 0.0003 inch radial clearance, and the kilovolt input to the coil. The electromagnetic facility has a maximum strain rate capability of $8.8 \times 10^7 \text{ sec}^{-1}$, but tests were limited to approximately $2.4 \times 10^7 \text{ sec}^{-1}$ in order not to damage elements of the testing facility.

A commercially available liquid phase sintered (LPS) heavy alloy containing 90% W, 8% Ni and 2% Fe was considered the baseline material for the test series, and five HIPed composites were tested for comparison. The HIPed samples consisted of a coated tungsten powder (CWP) composite (95.4% W, 3.0% Ni, 1.6% Fe), three W-Ti (30, 40 50 volume percent Ti) composites, and a W-Zr laminate composite.

Two kinds of punches were employed, a flat-face punch and a punch with its face ground to become a slant-face punch with approximately an 8 degree slope. The slant-face punch is useful in removing the problem associated with the impact stress waves generated when the punch face strikes the test sample and it also makes it possible to obtain a continuous range of strain rates developed in a single test specimen. This possibility occurs since the leading edge of the

punch face shears through the test specimen at the highest velocity, while the trailing edge of the punch face shears through after the punch has been slowed down by the shearing resistance of the test sample.

Although it would be desirable to obtain direct measurements of shearing force, preliminary efforts during Phase I were not successful enough to result in useful data. Note, however, that a measure of shearing strength of a material may be obtained by determining the punch velocity threshold for complete punching of the test sample. Because of the small number of tests in Phase I, good values of V_{50} could not be obtained. However, the table in Figure 5 contains approximate kinetic energy (KE) threshold estimates. Kinetic energy required for complete punching was highest for the baseline LPS 90%W, next for the HIPed CWP 95%W, and lowest for the Zr-W laminate and the W-Ti HIPed samples.

Figure 6 shows the bulk microstructure of the baseline LPS material, where the tungsten grains are the round particles with the matrix phase surrounding them. This microstructure is normal for liquid phase sintered tungsten heavy alloys.

Figure 7 shows the region of failure of the baseline LPS sample after impact by the slant-face punch. It is of great interest to observe that, in the area of failure where the shear strain was less than required for failure, the tungsten-to-tungsten grain contacts were failing earlier than the alloy matrix. This observation has previously been made for similar alloys tested at quasi-static and elevated strain rates (2-7). This is a clear indication that these contacts are the weak links in the heavy alloy microstructure and this weakness is present at elevated strain rates.

There is considerable deformation of the tungsten grains in the region of maximum shear, as shown in Figure 8. This extreme deformation of the tungsten grains was not unexpected, but there is a lack of the previously observed tungsten grain contact failures. Extreme ductility of tungsten is not the norm in pure tungsten as it is usually characterized by a high degree of brittleness. But, in tungsten heavy alloys, the tungsten grains are capable of undergoing great amounts of deformation due to the ability of the matrix to apply a hydrostatic stress component that delays failure to greater total strains. This extreme deformation of the tungsten grains has been observed, for example, in the examination of ballistically tested fragments (8-10).

A test methodology partly developed in Phase I was to simulate the on-target heating generated by the impact stress waves. The LPS sample responsible for Figure 9 was heated to 500° F (260° C) before impact. This figure shows the region of the punch strike and the lack of general failure. What is seen is the tungsten-to-tungsten grain contact failure and a much greater grain size than the room temperature samples. It is possible, that this sample was of a slightly different alloy and consequently had a larger grain size.

The region of failure of a coated tungsten powder (CWP) composite sample is shown in Figure 10. Good ductility is shown in the region of failure, produced with a flat-face punch, but brittle failure was exhibited by a CWP sample impacted by a slant-face punch. The appearance of the bulk microstructure is identical to the liquid phase sintered samples and suggests the samples were over-HIPed. Properly consolidated coated tungsten powder should have tungsten particles completely surrounded by the matrix (11).

Tungsten-titanium composites were tested with 30, 40 and 50 volume percent titanium. All these composites exhibited extremely brittle behavior. Figure 11 shows a titanium matrix so brittle that cracks propagating through it avoid, and are blunted by, tungsten particles! Oxygen analysis of these samples indicated a very high content. In all of the tungsten-titanium samples an interesting observation is that the titanium appears to have penetrated the grain boundaries of polycrystalline tungsten particles. This could have important implications for tungsten alloys in which the elimination of tungsten grain contiguity is an objective.

The Zr-W laminate shown in Figure 12 behaved in a brittle manner, similar to the W-Ti composites, but this sample did not suffer from the excessive oxygen content. The entire cross section was composed of approximately three

lamination units. It has been recently made clear that this few number of laminations is not sufficient to influence the failure behavior in ballistic testing and that there is a direct effect whereby greater numbers of laminations are beneficial (12). Figure 12 shows the crack path in the region of the punch strike. The crack clearly propagates through the tungsten phase, but there is no cracking in the zirconium layer. The original purpose of the zirconium was to provide a preferred crack path, but it certainly appears to not be the case. Not enough testing was conducted to permit reporting on promising trends.

SUMMARY

An electromagnetic Hopkinson Bar apparatus was constructed to evaluate tungsten-based materials at elevated strain rates. This device was successfully tested and revealed unique failure behavior in the materials tested.

REFERENCES

1. M. Kornhauser and R.J. Dowding, "Development of Tungsten Based Composites", U.S. Army Materials Technology Laboratory, MTL TR 92-7, February 1992.
2. R.V. Minakova, V.L. Voitenko, P.A. Verkhovodov, L.P. Nedelyaeva and N.N. Kalinyuk, "Fractographic Features of the Fractures of W-Ni-Fe Alloy (90:7:3) (A Review), Translated from Poroshkovaya Metallurgiya, No.2 (266), pp 81-92, February 1985.
3. K.-S. Churn and D.N. Yoon, "Pore Formation and its Effect on Mechanical Properties in W-Ni-Fe Heavy Alloy", Pow. Met. No. 5, 1979, pp 175-78.
4. K.-S. Churn and R.M. German, "Fracture Behavior of W-Ni-Fe Heavy Alloys", Met Trans A, Vol. 15A, February 1984, pp 331-338.
5. B.H. Rabin and R.M. German, "Microstructure Effects on Tensile Properties of Tungsten-Nickel-Iron Composites" Met Trans A, Vol 19A, June 1988, pp 1523-32.
6. T. Weerasooriya, P.A. Beaulieu and R. Swanson, U.S. Army Materials Technology Laboratory, Watertown, MA, MTL TR 92-19, April 1992.
7. J.R. Spencer and J.A. Mullendore, U.S. Army Materials Technology Laboratory, Watertown, MA, MTL TR 91-44, November 1991.
8. U. Gerlach, "Microstructural Analysis of Residual Projectiles-A New Method to Explain Penetration Mechanisms", Met Trans A, Vol. 17A, March 1986, pp 435-442.
9. E.S.C. Chin & P. Woolsey, "Dynamic Impact Response of Titanium Aluminate Composites", Army Science Conference Proceedings, Orlando, FL, June 1992.
10. E.S.C. Chin, R.J. Dowding, P. Woolsey and R.R. Biederman, "Tungsten Alloy Penetrator Interaction with a Titanium Aluminate Composite" these proceedings.
11. B.E. Williams, J.J. Stiglich, Jr., R.B. Kaplan and R.H. Tuffias, "A Major Advance in Powder Metallurgy", Technology 2001, Technology Transfer Conference, San Jose, CA, December 1991.

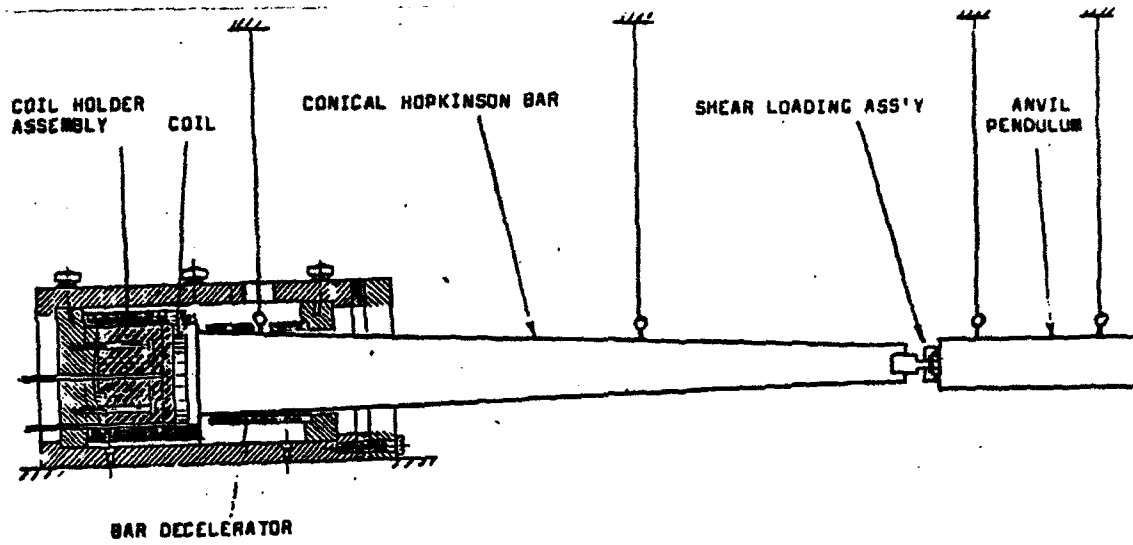


Figure 1. Electromagnetic Hopkinson Bar, Shear Test Configuration.

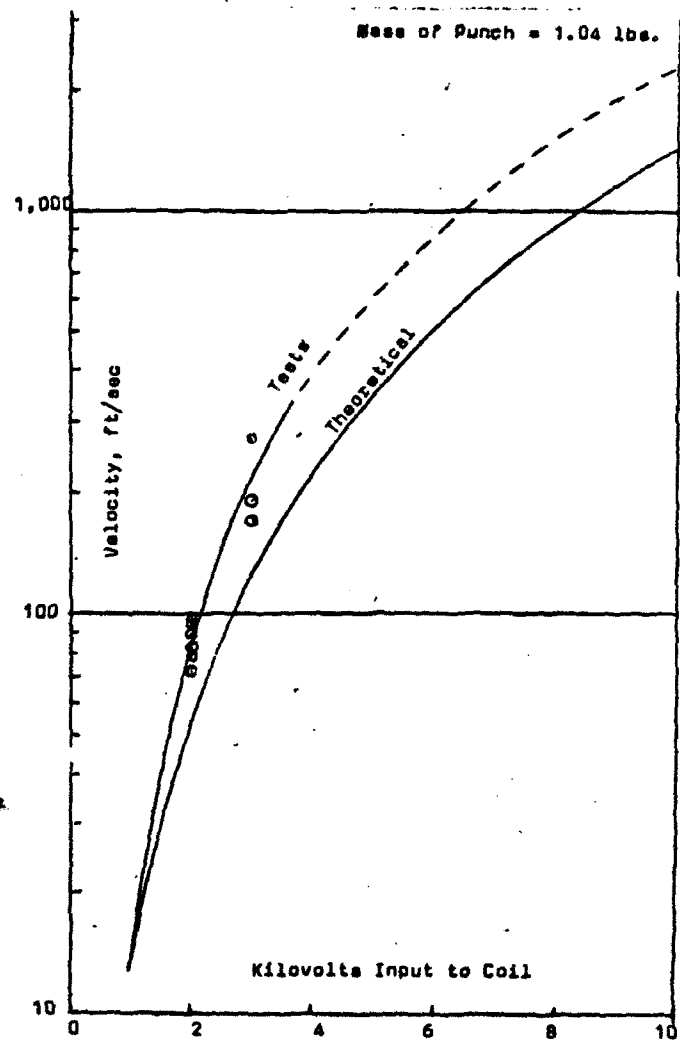


Figure 2. Punch Velocity versus Kilovolt Input.

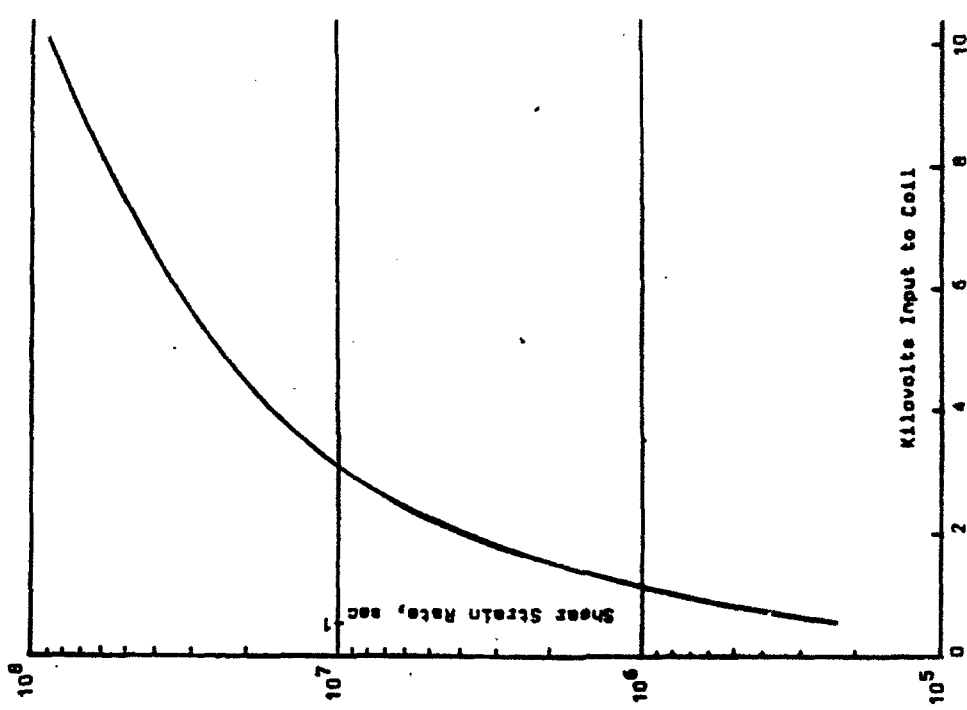


Figure 4. Strain Rates with 0.0003" Clearance.

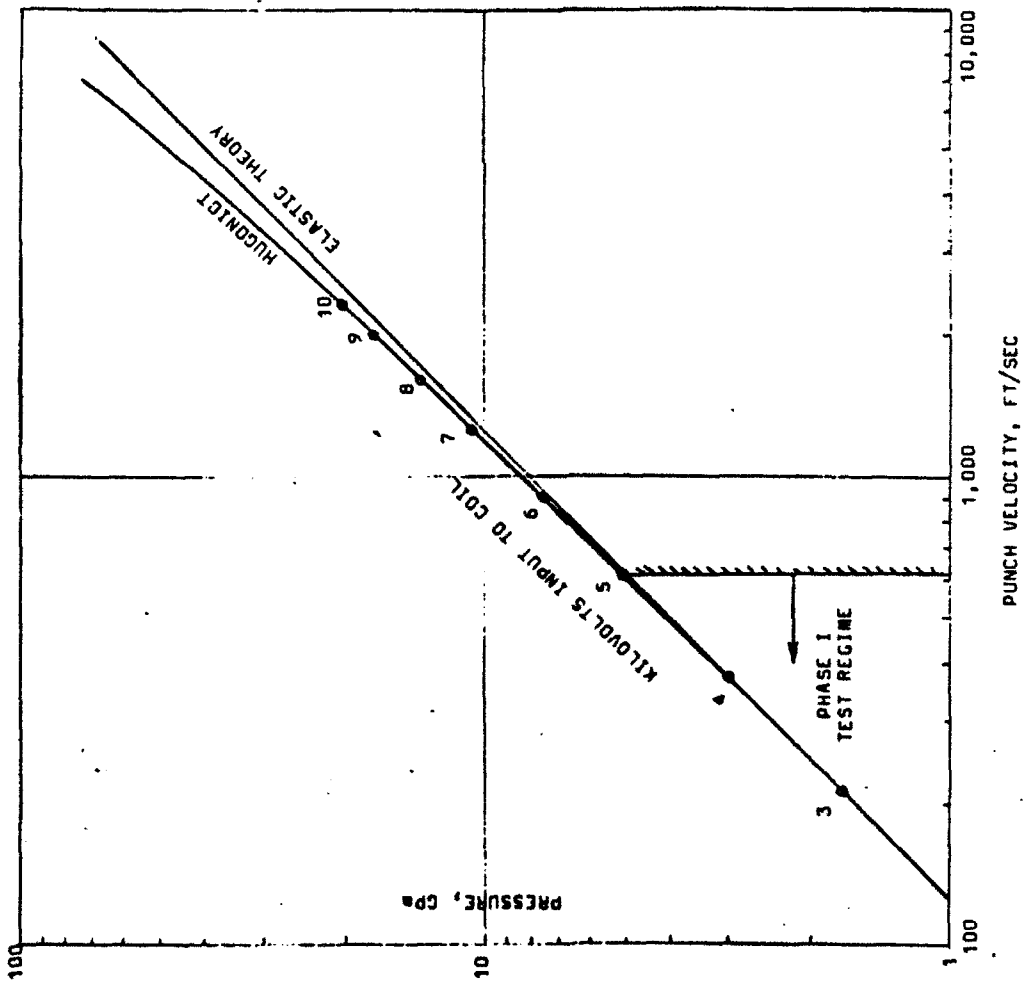


Figure 3. Pressure when Steel Punch Strikes Tungsten.

MATERIAL	FLAT	SLANT
(GTE) LPS 90%W	>5,910	1,580
CWP 95%W	403	403
Zr-W Lam.	403	<130
W-Ti	<130	<130

Figure 5. Threshold Kinetic Energy for Complete Punching, FT-LB.



Figure 6. Bulk Microstructure, Liquid Phase Sintered.

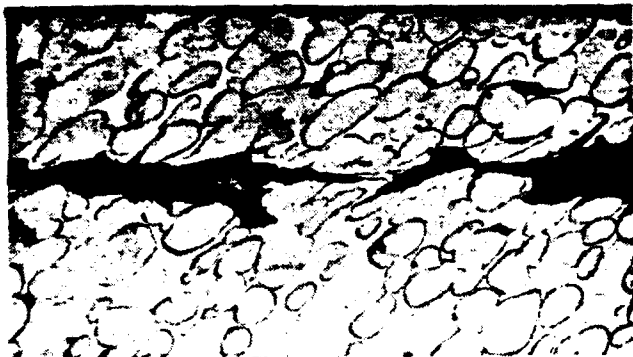


Figure 7. Region of Failure, Liquid Phase Sintered, Slant Punch, Ambient Temperature.



Figure 8. Region of Maximum Strain, Liquid Phase Sintered.

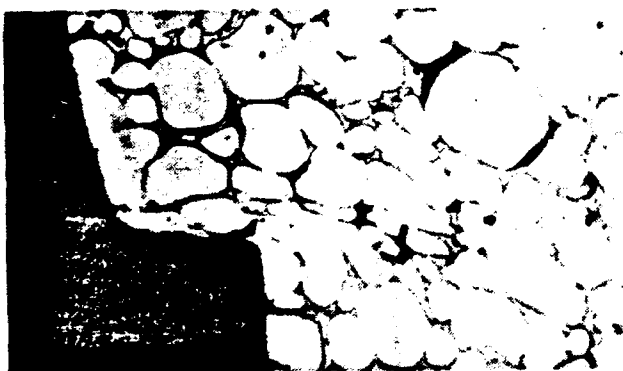


Figure 9. Region of the Punch Strike, Liquid Phase Sintered.

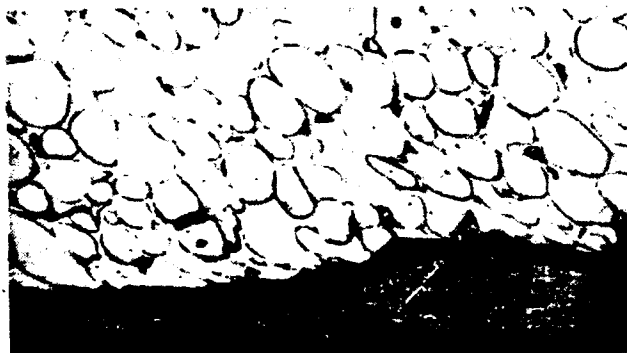


Figure 10. Region of Failure of Coated Tungsten Powder, Flat Punch, 530°F (275°C).

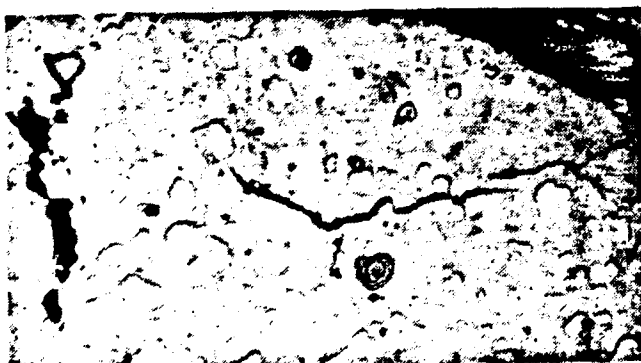


Figure 11. Region of Failure of W-30% Ti, Flat Punch, Ambient Temperature.

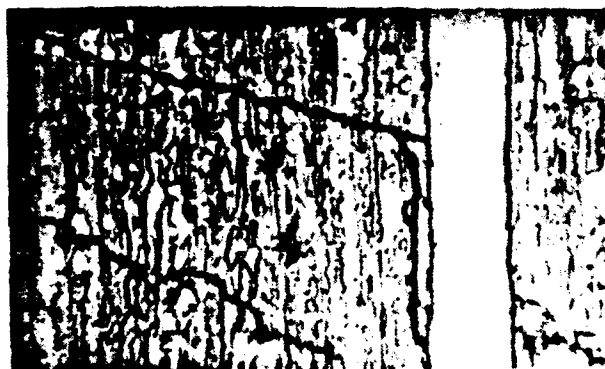


Figure 12. Crack Paths in Zr-W Laminations, Flat Punch, Ambient Temperature.

EFFECT OF IMPURITIES ON THE ELECTRONIC STRUCTURE OF GRAIN BOUNDARIES AND INTERGRANULAR COHESION IN TUNGSTEN

Genrich L. Krasko

Army Research Laboratory, Metals Research Branch
Watertown, MA 02172-0001

ABSTRACT

The cohesion of a grain boundary (GB) is believed to be the controlling factor limiting the ductility of high-strength metallic alloys, and particularly W. Intergranular embrittlement is usually associated with segregation of impurities at the GBs. Impurities present in ppm concentrations can result in a dramatic decrease in plasticity. This paper reviews recent results on both semi-empirical and first-principles modelling of the energetics and the electronic structures of impurities on a $\Sigma 3$ (111) GB in W. Our calculations have shown that impurities, such as N, O, P, S, and Si weaken the intergranular cohesion resulting in "loosening" the GB. The presence of B and C on the contrary, enhances the interatomic interaction across the GB. The so-called site-competition effect should play an important role affecting impurity distribution in W GBs. Among the impurities analyzed, B in the GB has the lowest energy, and thus would tend to displace other impurity atoms from the GB. Microalloying with 10-50 ppm B may be an effective way of improving tungsten's ductility. These results are important for understanding the fundamental physics of intergranular embrittlement.

INTRODUCTION

The reduced cohesion of grain boundaries (GBs) is often the controlling factor limiting ductility, and hence performance and reliability of high-strength metallic alloys [1]. Intergranular embrittlement in metals is usually caused by impurities segregating towards the GBs [2-6]. A ductile-brittle transition temperature (DBTT) as low as -196C [7] was observed in high purity W single crystals obtained by electron beam zone melting with special impurity gettering. Impurities present in bulk concentrations of 10^{-3} - 10^{-4} atomic percent can result in a dramatic decrease of plasticity, drastically degrading mechanical properties of metallic alloys, in particular, W, and thus posing significant technological and application problems. This detrimental effect of minute impurity concentrations can be readily understood. A simple estimate shows that a ppm amount of impurity is sufficient for saturating all the grain boundaries in a typical grain-size polycrystal. Sensitivity of the DBTT to the grain size confirms the above physical concept: the larger the grain size, the smaller amount of impurity is needed to saturate the GB[3]. Fine-grain polycrystals are known to be less brittle. It should be noted that BCC crystals, being not as close packed as FCC or HCP, are particularly prone to GB embrittlement by impurity segregation.

If impurities are the main cause of embrittlement, gettering the impurities is the obvious way of ductilizing W. A well-known, though extremely costly option is to use the so-called "Rhenium

Effect" (see, e.g.[8] and references therein). A more promising way of removing "the harmful" impurities, such as O, N, P, from the GBs is gettering by forming thermodynamically stable phases with other elements, e.g. Ti, Y, Mo, Zr, Hf, B [9-11]. This process, however, requires careful control since the ductility upon gettering will be improved only so far as the second phase precipitates remain fine; any coagulation of precipitates, such as the so-called Ostwald ripening, would result in an adverse embrittling effect.

During the recent decade, extensive experimental work was performed directed at a better understanding of the effect of impurities on intergranular cohesion in W. In this respect, a considerable contribution of Russian metallurgists should be acknowledged (see, e.g.[7-14] and references therein). Unfortunately, most of the related papers have been published in Russian, and therefore are virtually unknown to metallurgists in the West, though some of the papers have been translated.

Recent progress in developing efficient methods of first-principles calculations and computational algorithms made possible systematic studies of the role of impurities in intergranular cohesion of transition metals on the atomic and the electron-ion level. Calculations on both cluster, two-dimensional and supercell models of GBs with impurities have provided an in-depth insight into mechanisms of GB decohesion (for references, see[15]).

Since the first-principles electronic calculations on low-symmetry systems (such as lattice defects or GBs) are still extremely complicated and costly, semi-empirical methods based on solid first-principles foundations have also been developed. Among them, the most popular is the Embedded Atom Method (EAM) [16]. This method has been successfully used in a wide variety of calculations.

The purpose of this paper is to elucidate the energetics of impurities on a tungsten GB, and analyze the effect of impurities on the intergranular cohesion in W on the electron-atom level. A deeper understanding of the cohesion-decohesion processes on the microscopic level will lay a foundation for a "smart design" of ductile W alloys. In particular, the theoretical analysis of the electron structure and the energetics of W GBs, both clean (CL) and with impurities, enables one to make important predictions. As a result of the theoretical analysis we suggest a way of improving the W ductility by using the so-called "site-competition" effect. Boron introduced in minute quantities of 10-50ppm would cleanse the W GBs of other harmful impurities, enhancing the intergranular cohesion and thus improving the ductility.

ENERGETICS OF IMPURITIES IN W GBs.

In order to study the energetics of impurity atoms in a W GB, we have chosen first to calculate the quantity which may be called "environment-sensitive embedding energy" (ESE), the energy of an impurity atom in an atomic environment typical for a GB.

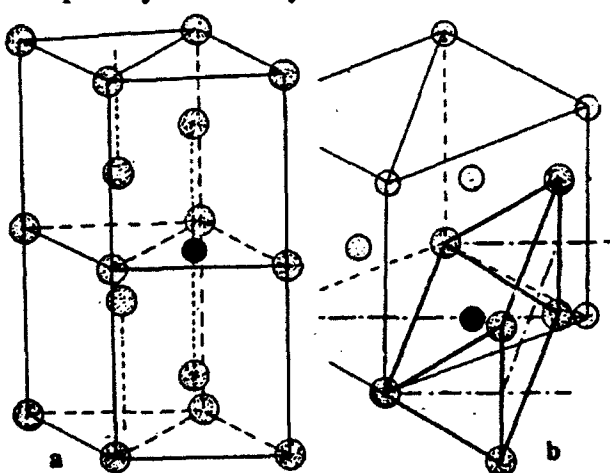


Fig. 1. The W_6X hexagonal supercell emulating a typical trigonal prism environment of W atoms in the (111) Σ 3 GB: a) the supercell; b) the trigonal prism coordination; \odot W, \bullet Impurity

Knowledge of these energies for various impurities enables one to compare the relative stability of a particular impurity in the W GB environment.

Having calculated the ESEs for a number of impurity atoms, one can use this information in a modified EAM approach for calculating the GB relaxation. The latter calculation enables one to draw important conclusions regarding the intergranular cohesion in W in the presence of a specific impurity in the GB.

The model chosen for the GB environment is an 8-atom hexagonal supercell (W_6X , where X is an impurity atom). The supercell is shown in Fig. 1, together with the capped trigonal prism coordination of the surrounding W atoms.

A trigonal prism GB configuration is believed to be a typical GB environment in BCC metals and is predicted by the theory of hard sphere

packing. Atomistic relaxation studies have shown that in Fe an impurity atom, such as P or B, is likely to occupy an interstitial position in the center of the trigonal prism formed by Fe atoms in the GB core (even if, like in case of P and B, the impurity forms a substitutional solid solution with the host). The hexagonal supercell of Fig. 1 has a relatively high symmetry; it also emulates a (111) $\Sigma 3$ GB environment [15].

We performed the spin-polarized scalar-relativistic Linear Muffin Tin Orbitals (LMTO) calculations (our method and approximations were the same as in [15]). First, a series of calculations (for six different volumes) were performed with an impurity absent from the supercell, i.e. an empty sphere of the same radius as that of the radius of the impurity's atomic sphere was substituted for the latter. Similar calculations were then performed for each of the impurities: B, C, N, O, Al, Si, P and S. The ESEs were defined as follows:

$$ESE = E(W_6\bullet) - E(W_6\circ) - E(\bullet) \quad (1)$$

where $E(W_6\bullet)$ and $E(W_6\circ)$ are respectively the energies of the supercell with and without the impurity (\circ stands for an empty sphere substituted for the impurity atom), and $E(\bullet)$ is the energy of the free impurity atom. In order to make the calculations more consistent, we have chosen to use, as $E(\bullet)$ s, the values of $E(W_6\bullet) - E(W_6\circ)$ extrapolated to the zero charge density ($n=0$), which would correspond to the energies of impurities in the GB environment with the host crystal lattice infinitely expanded. The ESE energies, Eq.(1), as a function of n , the electron charge density due to W atoms at the impurity site, are presented in Fig. 2.

Plots in Fig. 2 explain an experimentally observed phenomenon known as the "site competition" effect. As one can see, in the range of electron charge density typical of a GB (0.015-0.025 a.u.), B has the lowest energy and thus would tend to displace the other impurities off the GB. Thus, there exists a "site competition hierarchy". In fact, in W, N was found to successfully compete with C [11]; while C competes with P [17].

The plots in Fig. 2 also reveal an important aspect of GB impurity behavior. All the plots have well pronounced minima. The positions of the minima correspond to the electron density at the impurity site due to the surrounding W atoms which would occur if the GB were allowed to relax in

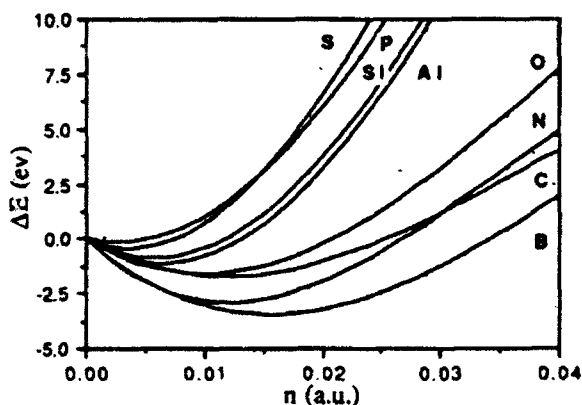


Fig.2. The "environment sensitive embedding energies" vs n , the electron charge density (in atomic units, a.u.)

such a way as to minimize the impurity's energy. The minima positions systematically (except for N) shift towards lower densities with the impurity losing its competitive power. A smaller charge density means a more "loose" GB, less strong and more prone to decohesion. The minimization of the total GB energy (rather than only the energy of the impurity atom) gives the characteristic charge densities which are somewhat higher than those in the minima. However, from this point of view, N, O, S, P, Si and Al are the obvious candidates for being "decohesive", while B and C may be called "cohesion enhancers". In fact, B and C were experimentally found to improve the GB cohesion in W [9, 10, 18, 18-20], while O, Si, P and S, being strong embrittlers [3, 6, 17-21], are believed to weaken the GB cohesion.

As mentioned above, the GB environment we were dealing with was that of the (111) $\Sigma 3$ tilt GB. The GB structure can be represented as a succession of (111) hexagonal planes:

...CBACBACBACBACBABCABCABCABC...

(the GB plane is marked by A). The CBABC atomic stacking of the core of the GB (CL or with an impurity) is just the one emulated by the 8-atom supercell shown in Fig.1. In order to find the GB structure corresponding to a minimum of energy, Eq.(2), the interplanar distances were varied, while the interatomic spacings and the structure within the (111) planes were left unchanged.

The total energy, E , was calculated using a modified EAM approach:

$$E = \sum_R E_{\text{emb}}(n(R)) + 1/2 \sum_{R,R'} V(R,R') + ESE(n(R_{\text{imp}})) \quad (2)$$

where $E_{\text{emb}}(n)$ and $V(R,R')$ are the EAM embedding energy and the pair potential as found for the bulk BCC W (we used the Finnis-Sinclair functions and parameters [22]). The third term is the energy of the impurity atom. R and R' are the positions of the host atoms, R_{imp} is that of the impurity, and $n(R)$ and $n(R_{\text{imp}})$ are the electron charge densities at the site of a host atom and the impurity respectively. The electron charge density at a given site can be taken to be a superposition of the free atom charge densities or found from more sophisticated procedures.

It was found that, like in the case of the Fe GB [23], the interplanar distances oscillate (as a function of remoteness from the GB), the deformation waves decaying by the 10th-12th plane away from the GB. An interesting feature of the CL GB relaxation is that the distance between the 2nd and 3rd planes is a little over a half of the (111) interplanar distance in bulk BCC W (0.550Å vs 0.914Å). Though W does not undergo transformation into the ω -phase, the "misbalance" in interatomic interaction arising due to the GB results in the tendency for plane 3 to nearly collapse into plane 2 (the ω -phase configuration). The site-projected electronic densities of states of the W atoms in planes 1-3 are very similar to that typical of a ω -phase.

The impurity atoms, B, C, N and O result in some "damping" of the relaxation deformation waves, i. e. decreasing the oscillation amplitudes. This damping is most pronounced for B and C. Although the distance between planes 1 and 2 (which is the distance between two W2-atoms across the GB) monotonically increases, the tendency of plane 3 to collapse into plane 2 disappears: in the progression B through O the W2-W3 distance is almost equal to that in the bulk. Except for the W2-W3 distance, the amplitude of the deformation wave increases with Al, Si, P and S. Damping of the

deformation wave may be interpreted as "cohesion enhancement", while the corresponding increase of the deformation wave oscillations may be thought of as resulting in "decohesion".

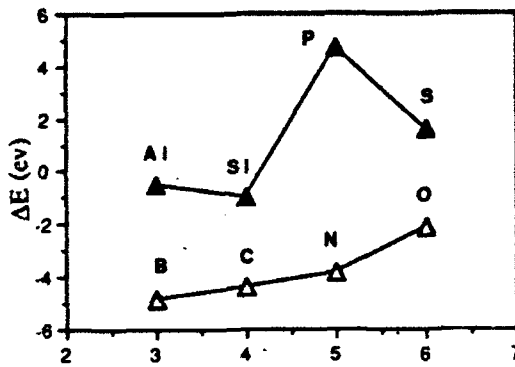


Fig.3. $\Delta E = E_{\text{GB}}(\bullet) - E_{\text{GB}}(\text{CL})$, the energy difference between the GB with impurity \bullet and CL GB, vs the Periodic Chart group number

From a thermodynamic point of view [24], the impurity's embrittling potency depends on the difference between the free energies of the impurity's segregation on the initial GB and on the two free surfaces emerging upon fracture. The higher the difference, the stronger the embrittling potency of the impurity. As a less rigorous but simpler criterion, in Ref.[5] the sublimation energy differences between the host and impurity were calculated in an ideal solution model for over 60 elements. According to Ref. [5], among the elements analyzed, only B, C and Os may be cohesion enhancers in W. In our more rigorous approach, the effects of impurities on GB stability can be analyzed by simply comparing the GB energy differences, ΔE , between the GB with impurities and the CL GB.

The corresponding values for the impurities discussed are plotted in Fig. 3. One can see that the GB stability decreases from B towards O, and the energy difference becomes positive for P and S--the strongest embrittlors. The latter means that GBs with P and S are unstable at OK.

FIRST PRINCIPLES GB SUPERCELL CALCULATIONS

In order to study the electronic structure of the GB (both CL and that with an impurity atom in it) we performed a series of LMTO supercell calculations. A 20-atom supercell was used as a model of the GB (Fig. 4). Again, like in our semi-empirical calculations, the GB is modelled by the succession of (111) hexagonal planes:



The two stacking faults: ...CAC... and ...BAB..., imitate two (111) $\Sigma 3$ tilt GBs. The filled circles in Fig. 4 show impurity atoms (or empty spheres, \bullet , if the GB is CL). There are 8 planes of W atoms between the two GB planes A. The immediate impurity environment is again the trigonal prism of W atoms shown in Fig. 1.

In order to make the GB model more realistic, the interplanar distances were taken to be equal to those obtained from the above semi-empirical relaxation calculations for planes 2 through 5 (on both sides of the GB planes); the distance between two equivalent planes (5) in the middle of the supercell was set equal to the interplanar distance in the bulk (0.914Å).

When a metalloid atom is added into a transition metal crystal lattice, two effects are produced. First, the crystal lattice is expanded, and second, a covalent bond between the impurity atom and the host transition atom is formed[25]. A similar situation takes place in a W GB.

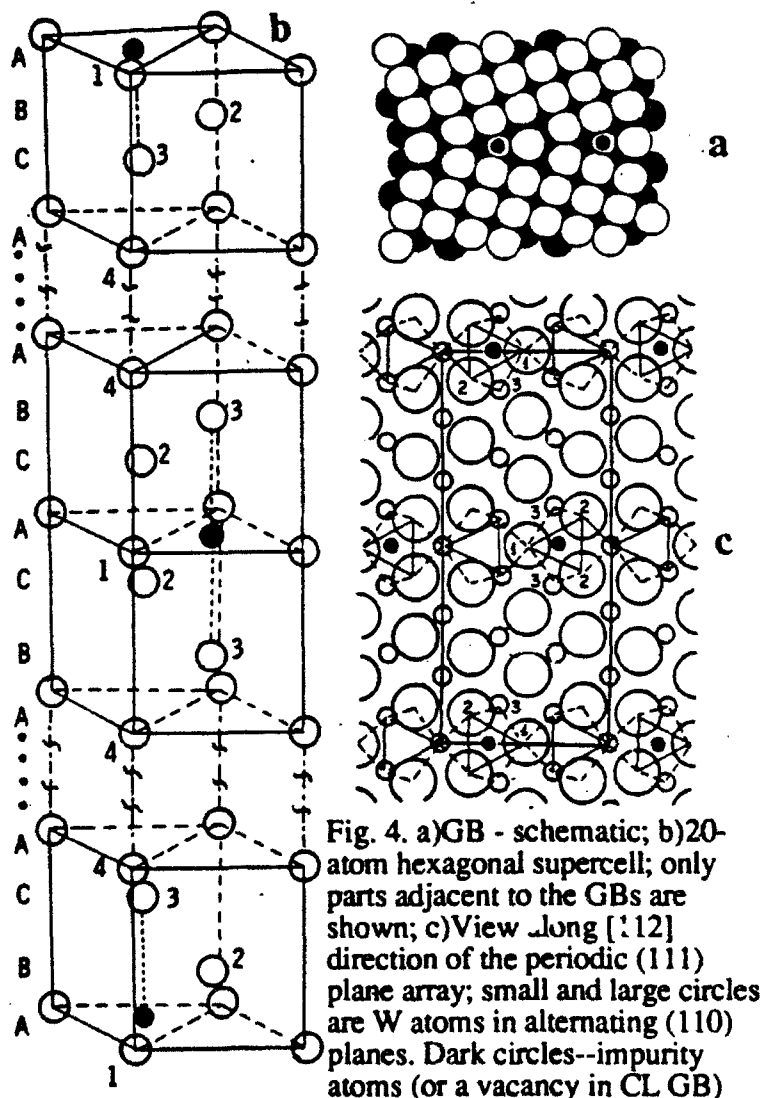
As follows from our calculations, the volume difference between the CL GB and that with an impurity increases monotonically from B through S. From the intuitive point of view, the increase in volume is expected to result in a weakening of interatomic bonding, though, in principle, an impurity may exert a stronger interaction in spite of the lattice expansion.

Table 1 shows the interatomic distances in relaxed GBs. The distance between an impurity atom (or an empty sphere) and W1 atom (2.584Å), is the same in all cases, since we did not allow the atoms within the (111) planes to relax.

The counterpart of the nearest neighbor distance in the bulk BCC lattice (2.741Å) is the distance between two W1 atoms (W1-W1) in the [111] direction. In the CL GB this distance is longer than in the bulk, while the shortest distance is the one between two atoms W2 (W2-W2) across the GB. In the CL GB there is a significant void (occupied by an \bullet); the distance between atoms W3 (W3-W3) across the void (and the GB plane) is quite large: 3.614Å. Thus, in the CL GB the strongest interaction is W2-W2, followed by W1-W1 and W1-W2. With an impurity atom in place of \bullet , the interatomic interaction changes significantly. Now the shortest distance is \bullet -W3, W2-W2

TABLE 1
Interatomic Distances (in Å) in Relaxed GBs

	\bullet -W3	W1-W1	W1-W2	W2-W2
\bullet	1.807	2.841	2.873	2.512
B	2.170	3.056	2.914	2.690
C	2.223	3.090	2.924	2.736
N	2.290	3.133	2.940	2.805
O	2.317	3.150	2.948	2.839
P	2.588	3.345	3.048	3.234
S	2.666	3.426	3.090	3.389



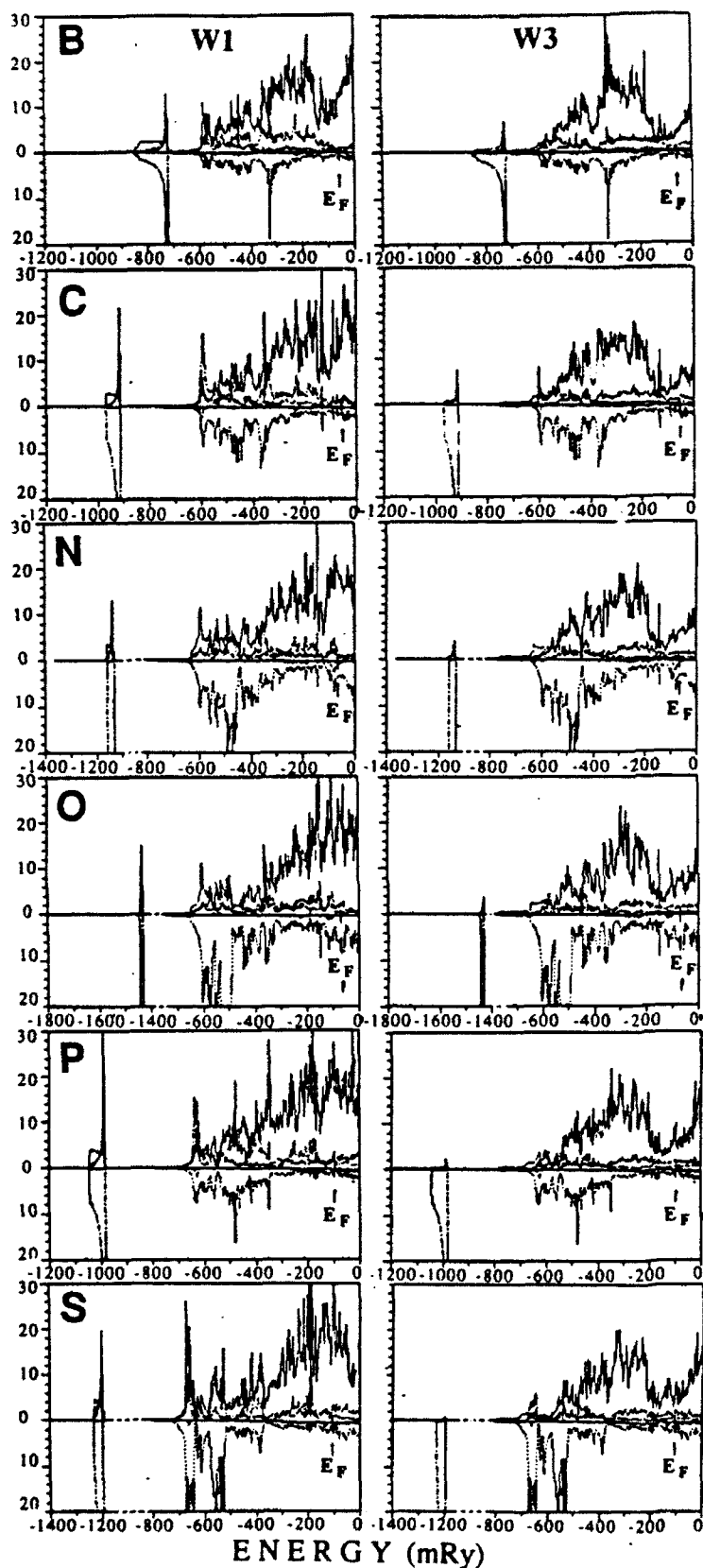


Fig. 5. The site-projected DOSs (states/Ry) for atoms W1 and W3; s --- p d —; Zero energy here and in Fig. 7 corresponds to the E_F of bulk BCC W

being the second, and the interaction between the impurity atom and atom W3 becomes of utmost importance.

Fig. 5 shows the site projected electronic densities of states (DOSs) for atoms W1 and W3 for the CL GB and GBs with different impurities. The lower ("negative") parts of the plots show the site-projected DOSs within the atomic spheres of the corresponding impurities; they are identical in plots for atoms W1 and W3. These plots actually represent the GB electronic band structure, and allow an analysis of interatomic bonding.

When an impurity atom is immersed into the electron-atom system of the host, its electrons become part of the whole system. The atom's electronic states hybridize with the electronic bands of the metal, resulting in forming covalent bonds between the impurity and the host atoms. In fact, the whole electron charge density distribution becomes affected, and interactions among all the atoms disturbed.

As is typically the case for metalloid impurities [15], the impurity s-electrons (2s for B through O, and 3s for P and S) form in W the narrow impurity bands below the bottom of the metal valence band. Even though the corresponding s-levels in the free atoms lie well below the W p- and d-bands, upon alloying, the s electrons do hybridize with those bands, resulting in strongly localized but rather weak ionic type bonds.

The impurities' p-electrons with the energy right inside the W valence bands, create pronounced covalent bonds. The impurity bonding states of predominantly p-type hybridize with W mostly d- and also p-states. Comparison of the DOS plots for atoms W1 and W3 show that the \bullet -W1 hybridization in the GB plane is stronger than \bullet -W3 across the GB, in spite of the fact that the former distances are larger than the latter (Table 1). This means that the W atoms in the GB plane are bound stronger than across the GB. As one can see, the impurity s-p bands are shifting towards the W d-band bottom, thus "switching off" the W bonding d-electrons in the upper part of the d-bands. As a result the hybridization

becomes weaker in the row B through O. In case of B, a significant part of the W d-states are involved. In fact, one can even speculate that the \bullet -W3 hybridization is the strongest, since a pronounced peak of W d-states is involved. For O, P and S, the hybridization of electronic d-states at the bottom of the d-band (the peaks around -600mRy) within the atom W3 sphere almost disappears, while it is still moderate within the atom W1 spheres.

Another important trend can also be seen. Beginning with N and beyond, some anti-bonding states (both in W and \bullet) --to the right of the "troughs" around the Fermi energy, E_F --are progressively filled, resulting in weakening the interatomic bonds. In terms of the charge density, "bonding" means a pile-up of electronic charge in the space between the atoms, while the "anti-bonding" states result in decreasing the charge density. Fig. 6 compares the electron charge densities in atomic spheres of B and O.

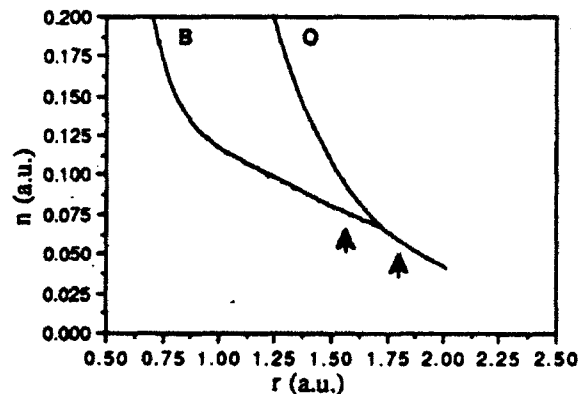


Fig. 6. Electron charge densities in atomic spheres of B and O

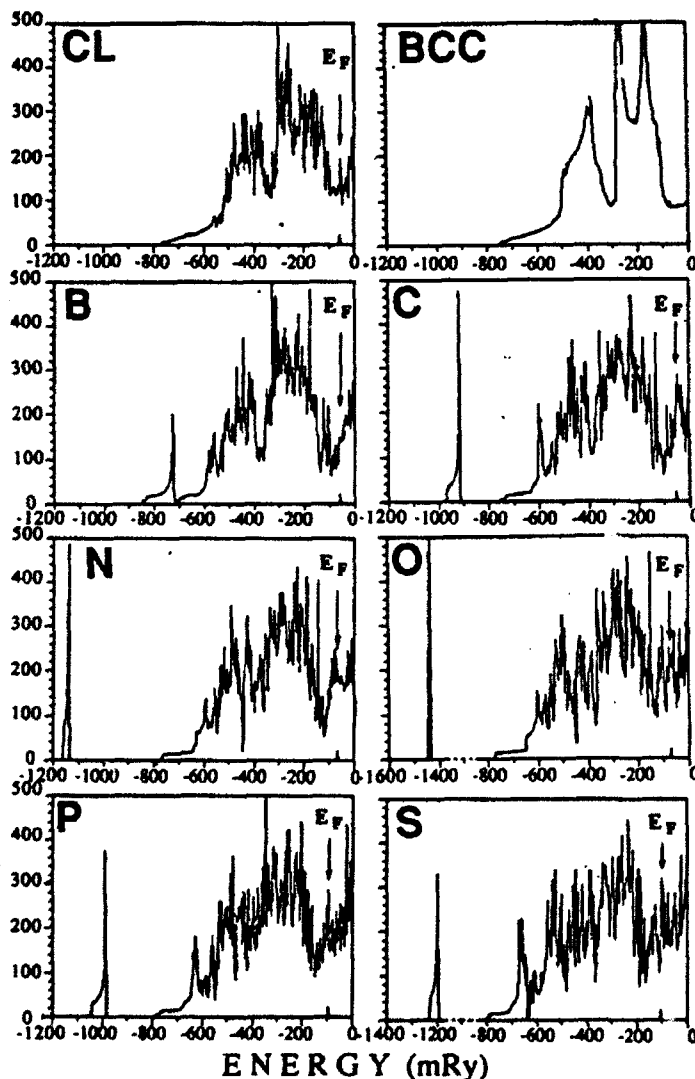


Fig. 7. Total DOSs for BCC W, CL GB and GB with impurities. Arrows show the Fermi energies

Fig. 6 compares the electron charge densities in atomic spheres of B and O. The arrows show the density values corresponding to the so-called "muffin-tin" radii, the radii of touching hard spheres representing B or O and atom W3 (the nearest neighbor to the impurity atoms). One can see that the electron density of B in "the point of contact" with atom W3 is 1.5 times greater than that of O, thus suggesting a higher "bonding capacity" of B, as compared to that of O.

Finally, it is interesting to compare the total DOSs of a CL GB, GBs with impurities and bulk BCC W. Fig. 7 shows the plots. As in the site-projected DOSs, the GBs with impurities demonstrate strongly localized impurity bands. Each of them contain exactly two electrons, as it should be, since the corresponding Brillouin Zones are completely filled. As mentioned earlier, the anti-bonding states (to the right of the troughs around ~ 100 mRy) being almost completely unfilled in bulk W, begin to progressively fill in the GBs. The Fermi energy, E_F , sits on peaks, their heights increasing from B through S. In fact, the E_F peak in the CL GB is higher than that for B. A relative DOS value at E_F is known to be an indication of the system stability. The higher the value, the lower the stability. From this point of view, the stability of the GB is lower than that of the bulk W, while B improves the stability as compared to that of the CL GB.

CONCLUSIONS

Both the semi-empirical and first-principles analysis has shown that B in the W GB plays a dual role. First of all, due to the site-competition effect, it tends to displace the other impurity atoms off the GB thus

"cleansing" it. At the same time, B enhances the intergranular cohesion, thus improving resistance to brittle fracture. A simple estimate shows that 10-50ppm of impurity atoms will saturate the GBs in W. Ideally, the same amount of B would be sufficient to significantly improve the ductility. However, the above analysis disregards a possible chemical activity of B, e.g., forming boron oxides or tungsten borides. The latter would require introducing a multiplying factor to correct for B expended on the chemical activity. Alloying W with B in quantities 10-15 times greater did result in a significant (150C) drop in DBTT [9,12]. This effect was attributed to gettering O by forming boron oxides. In any case, microalloying W with B is extremely promising. The relatively ductile W, being a BCC metal, may be able to develop the adiabatic shear behavior (important for anti-armor applications [26]); the adiabatic shear instability is observed in BCC high-strength steels in conditions of "marginal" ductility [27]. It is also worth noting that at high temperatures microalloying W with B (and possibly with C) would improve resistance to creep. The experimental work directed at elucidating the various aspects of microalloying W is currently in progress at ARL.

ACKNOWLEDGEMENTS

The author is grateful to Dr. R.P.I. Adler and Dr. M. Azrin for their interest and invaluable support. Fruitful discussions with Dr. R. J. Harrison, R. Dowding and G. Zilberstein are also gratefully acknowledged. The LMTO code used in calculations was developed by Prof. N. Christensen.

REFERENCES

1. *Embrittlement of Engineering Alloys* (ed. C. L. Briant and S.K. Banerji), Acad. Press, New York, 1983; *Interfacial Segregations* (ed. W.C. Johnson and J. M. Blakely), ASM, Metals Park, OH, 1979.
2. C. L. Meyers, Jr., G. Y. Onoda, A. V. Levy, and R. J. Kotfila, "Role of The Grain Boundaries in the Ductile-Brittle Transition Behavior of BCC Refractory Metals", *Trans. Metall. Society of AIME*, Vol. 233, 1965, pp. 720-728.
3. J. Joshi and D. F. Stein, "Intergranular Brittleness Studies in Tungsten Using Auger Spectroscopy", *Metall. Trans.*, Vol. 1, 1970, pp. 2544-2546.
4. D. A. Smith and G. D. W. Smith, "Solute Segregations and Grain Boundary Embrittlement of Tungsten", in *The Microstructure and Design of Alloys*, Proc. of the 3rd Intl. Conf. on the Strength of Metals and Alloys, London, 1973, pp. 144-148.
5. M. P. Seah, "Grain Boundary Segregation", *J. Phys. F*, Vol. 10, 1980, pp. 1043-1064; "Adsorption-Induced Interface Decohesion", *Acta Met.*, Vol. 28, 1980, pp. 955-962; M. P. Seah and E. D. Hondros, "Atomistic Mechanisms of Intergranular Embrittlement", in *Atomistics of Fracture*, ed. by R. M. Latanision and J. R. Pickens, Plenum, New York, 1983, pp. 855-888.
6. D. Y. Lee, E. V. Barrera, J. P. Stark and H. L. Marcus, "The Influence of Alloying Element on Impurity Induced Grain Boundary Embrittlement", *Metall. Trans. A*, Vol. 15A, 1984, pp. 1415-1430.
7. Ye. M. Savitskiy and G. I. Burkhanov, *Physical Metallurgy of Refractory Metals* (*Metallovedeniye Tugoplavkikh Metallov*, in Russian), Nauka, 1967
8. See R. Dowding, these proceedings.
9. K. B. Povarova, et al., "Effect of Microalloying on the Low-Temperature Plasticity and Technological Expediency of Vacuum-Melted Tungsten of Technical Purity," *Izvestiya Acad. Nauk SSSR. Metalliy*, No.1, 1990, pp.76-81 (translation: *Russian Metallurgy, Metalliy*, No. 1, 1990, pp. 74-79).
10. A. S. Drachinskii, et al., "Criterion for Optimal Choice of Alloying Elements to Lower the Intergranular Embrittlement in Metals of Group VIA", *Fizika Metallov i Metallovedenie*, No. 2, 1984, pp. 324-329 (translation: *Phys. Met. Metallogr.*, No. 2, Vol. 58, 1984, pp. 102-107).
11. L. S. Burmaka, et al., "On the Competition Between Interstitial Atoms During the Formation of Segregates on Grain Boundaries of Molybdenum and Tungsten", *Fizika Metallov i Metallovedenie*, Vol. 42, No. 5, 1976, pp. 1089-1092 (translation: *Physics of Metals and Metallography*, Vol. 42, 1976, pp.168-171).

12. K.B. Povarova, et al., "Effect of Microalloying on the Ductile-Brittle Transition Temperature of Tungsten", *Izvestiya Acad. Nauk SSSR. Metallurgy*, No.1, 1987, pp.134-141 (translation: *Russian Metallurgy, Metallurgy*, No. 1, 1987, pp.129-136); Yu. O. Tolstobrov and K. B. Povarova, "Effect of Microalloying With Boron on the Structure and Properties of Tungsten", *Fizika i Khimiya Obrabotki Materialov*, Vol. 21, No. 5, 1987, pp. 121-124 (in Russian).
13. K. B. Povarova and Yu. O. Tolstobrov, "The Solubility of Boron in Tungsten", *Izvestia Acad. Nauk SSSR, Metallurgy*, No. 4, 1988, pp. 54-57 (translation: *Russian Metallurgy, Metallurgy*, No. 4, 1988, pp. 52-55); K. B. Povarova and E. K. Zavarzina. "The Effect of Heat Treatment on Structure and Properties of Tungsten Alloys", *Izvestia Acad. Nauk SSSR, Metallurgy* No. 5, 1989, pp. 118-126 (translation: *Russian Metallurgy, Metallurgy*, No. 5, 1989 pp. 112-119).
14. M. Pavlov, Ye. V. Ushakov and Ye. K. Drobysheva, *Cold Brittleness and Structure of Tungsten (Khladnolomkost i Struktura Vol'frama*, in Russian), Nauka, 1984, pp. 1-129.
15. G. L. Krasko and G. B. Olson, "Effect of Boron, Carbon, Phosphorus and Sulfur on Intergranular Embrittlement in Iron", *Solid State Commun.*, Vol. 76, 1990, pp. 247-251; "Effect of Hydrogen on the Electronic Structure of a Grain Boundary in Iron", *Solid State Commun*, Vol. 79, 1991, pp. 113-117.
16. M. S. Dow and M. I. Baskes, "Embedded Atom Method: Derivation and Application to Impurities, Surfaces, and Other Defects in Metals", *Phys. Rev. B*, Vol. 29, 1984, pp. 6443-6453; M. S. Daw, "Model of Metallic Cohesion: The Embedded Atom Method", *ibid*, Vol. 39, 1989, pp. 7411-7452, and references therein.
17. H. Hoffman and S. Hoffman, "An AES Study of Phosphorus and Carbon Segregation in Ti-Fe-Activated Sintered Tungsten", *Scripta Met.* Vol. 18, 1984, pp. 77-88.
18. E. Smiti, et al., "The Influence of Carbon and Oxygen in the Grain Boundary on the Brittle-Ductile Transition Temperature of Tungsten Bi-Crystals", *Scripta Met.*, Vol. 18, 1984, pp.673-676.
19. C. L. White, et al., "Boron Segregation to Grain Boundaries and Improved Ductility in Pt+30Wt.Pct.Rh+8Wt.Pct.W", *Metal. Trans.* Vol. 12A, 1981, pp. 1485-1490.
20. H. Taga, and A. Yoshikawa, *Proc. ICSTIS, Suppl. Trans. ISIJ*, Vol 11, 1971, pp. 1256-1259.
21. T. H. Loi, et al., "Segregation of Phosphorus at the Grain Boundaries of Polycrystalline Tungsten. Relations With the Brittle-Ductile Transition Temperature and the Mode of Fracture", in *Physical Chemistry of the Solid State: Application to Metals and Their Compounds*, ed. by P. Lacombe, Elsevier, New York, 1984, pp. 243-252; "Brittle Fracture of Polycrystalline Tungsten", *J. Mat. Sci.*, Vol. 20, 1985, 199-206.
22. M. W. Finnis and J. E. Sinclair, "A Simple Empirical N-Body Potential for Transition Metals", *Phil. Mag.*, Vol. A50, 1984, pp. 45-56; errata, *ibid*, Vol. A53, 1986, p. 161.
23. G. L. Krasko, "Environment Sensitive Embedding Energies and Grain Boundary Relaxation in Iron", *Proc. of the 1991 MRS Fall Meeting*, Boston (in press).
24. J. R. Rice and J.-Sh. Wang, "Embrittlement of Interfaces by Solute Segregations", *Mat. Sci. and Engineering*, Vol. A107, 1989, pp. 23-40.
25. C. D. Gelatt, Jr., A. R. Williams, and V. L. Moruzzi, "Theory of Bonding of Transition Metals to Nontransition Metals", *Phys. Rev. B*, Vol. 27, 1983, pp. 2005-2013.
26. L. S. Magness and T. G. Farrand, "Deformation Behavior and Its Relationship to the Penetration Performance of High-Density KE Penetrator Materials", *Proceedings of the 1990 Army Science Conference*, 1991, pp.465-479.
27. G. B. Olson, J. F. Mescall and M. Azrin, "Adiabatic Deformation and Strain Localization", *Shock Waves and Strain-Rate Phenomena in Metals*, ed. by M. A. Meyers and L. E. Murr, Plenum, 1981, pp. 221-247.

POST-FABRICATION EVALUATION AND CHARACTERIZATION
OF A COMMERCIAL TUNGSTEN HEAVY ALLOY

John B. Posthill
Research Triangle Institute
Research Triangle Park, North Carolina 27709-2194

Robert J. Dowding and Kenneth J. Tauer
U.S. Army Research Laboratory
Watertown, MA 02172-0001

A particular material which has certain interesting features or is used in a sensitive activity might require evaluation without direct knowledge of its fabrication or processing history. This brief communication demonstrates how certain information can be gleaned about a tungsten heavy alloy without any detailed a priori knowledge of its fabrication. The material so examined is a commercially-produced tungsten heavy alloy with a nominal concentration of 93 wt.% tungsten.

The material in question was received in final manufactured condition as a full-scale kinetic energy (KE) penetrator. Appropriate sections were taken from it for chemical analysis, quasi-static mechanical testing and microstructural analysis. Chemical analysis showed the composition of the major metallic constituents to be: 92.8 wt.% W, 6.0 wt.% Ni, 1.1 wt.% Fe, and 0.15 wt.% Co. Tensile testing at a strain rate of $5 \times 10^{-4} \text{ s}^{-1}$ (ambient temperature) indicated the material to have ultimate tensile (UTS) and yield (0.2% offset) strengths of 187 KSI and 164 KSI, respectively. Elongation was measured to be 14%. Unnotched Charpy impact (5 mm x 5 mm) measurements were found to average to 5.7 ft-lb.

Optical microscopy of polished sections revealed that the W grains were elliptical in nature indicating that the material had been deformed. From the W grain aspect ratios, it was estimated that the amount of area reduction the alloy had undergone (presumably by swaging) was approximately 35% [1]. Fracture surfaces were examined by scanning electron microscopy (SEM). Fractography of the surfaces created by tensile testing and Charpy impact measurements, as well as by hammer fracture, revealed typical fracture features that predominate in tungsten heavy alloy failure; (i) cleaved W grains, (ii) ductile matrix failure, (iii) W-W intergranular grain boundary separation [featureless], and (iv) W-W intergranular grain boundary separation showing precipitation of γ -phase on failed boundaries, Figure 1. Additionally, there were regions of W- γ interphase failure that appeared featureless. This fracture feature has previously been associated with impurity element segregation (i.e., S and P) in other W heavy alloys [2].

Thin foils for examination by transmission electron microscopy (TEM) were prepared by electropolishing. These sections were taken transverse to the length of the penetrator. TEM examination showed that the matrix phase and the W grains had dislocation cell structures that have begun to form as a result of the deformation, Figure 2. Additionally, the precipitation at the W-W grain boundaries was confirmed to be Ni- and Fe-containing fcc γ -phase by both selected-area electron diffraction (SAED) and energy dispersive X-ray spectrometry (EDS), Figure 3. This has been identified and confirmed in other tungsten heavy alloys previously [3]. Furthermore, fine scale precipitation was observed in the interior of the W grains, Figure 4. These precipitates are most easily observed when the diffracting conditions used enhance their $\langle 100 \rangle$ strain contrast. The precipitates are very much like those observed previously in tungsten heavy alloys [4,5]. They are platelets that lie on $\{100\}$ planes and are approximately 3.5 nm in diameter. Both W-W grain boundary precipitation

and fine scale precipitation are indicative of post-deformation heat treatment, such as aging. The electropolished TEM thin foil makes an excellent surface from which to obtain further SEM data. Figure 5 shows how these samples are used in conjunction with a high resolution SEM to obtain more statistically valid information; in this case W-W grain boundary precipitation is shown. Also, inclusions that contained: Al, K, Ca, Ti, Cr, and Mn were identified with the aid of EDS, Figure 6.

In summary, it is believed that this nominally 93 wt.% W heavy alloy has been swaged and aged to strengthen it beyond its as-sintered strength. It is believed that improvements to this alloy could potentially be made by reducing the concentration of impurities that contribute to inclusion formation and W- γ separation. Several diagnostic techniques have been demonstrated which can find utility in uniquely characterizing commercially manufactured tungsten heavy alloys.

REFERENCES

1. A.R. Bentley and M.C. Hogwood, "The Effect of Mechanical Deformation and Heat Treatment on the Microstructural Characteristics of Two Tungsten Heavy Alloys", these proceedings.
2. B.C. Muddle and D.V. Edmonds, *Metal Science*, 17, 209, 1983.
3. J. B. Posthill, M.C. Hogwood and D.V. Edmonds, *Powder Metallurgy*, 29, 45 (1986).
4. J. B. Posthill and D.V. Edmonds, *Mater. Res. Soc. Symp. Proc.*, 21, 811 (1984).
5. J.B. Posthill, *Proc. 42nd Ann. Meet. Electron Microscopy Society of America*, Ed. G.W. Bailey, 488 (1984).



FIGURE 1. SEM fractograph for the same surface showing a variety of different types of tungsten heavy alloy failure: (A) extensive W grain boundary cleavage; (B) another area showing W-W failure with precipitation on boundaries [e.g. 1], ductile matrix failure [e.g.2], and featureless W- γ separation [e.g.3]; (C) higher magnification showing two separated W-W boundaries with precipitation; and (D) higher magnification showing W- γ separation [1] and largely featureless W-W boundary failure [2].

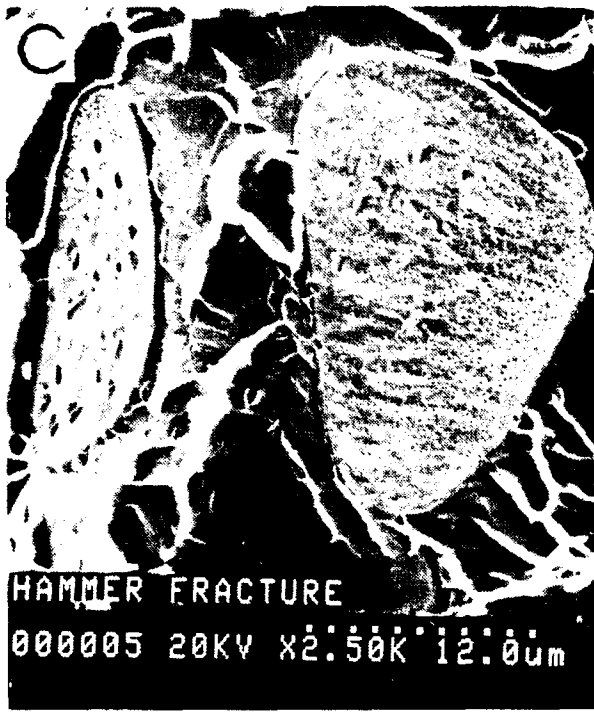


FIGURE 1, C and D

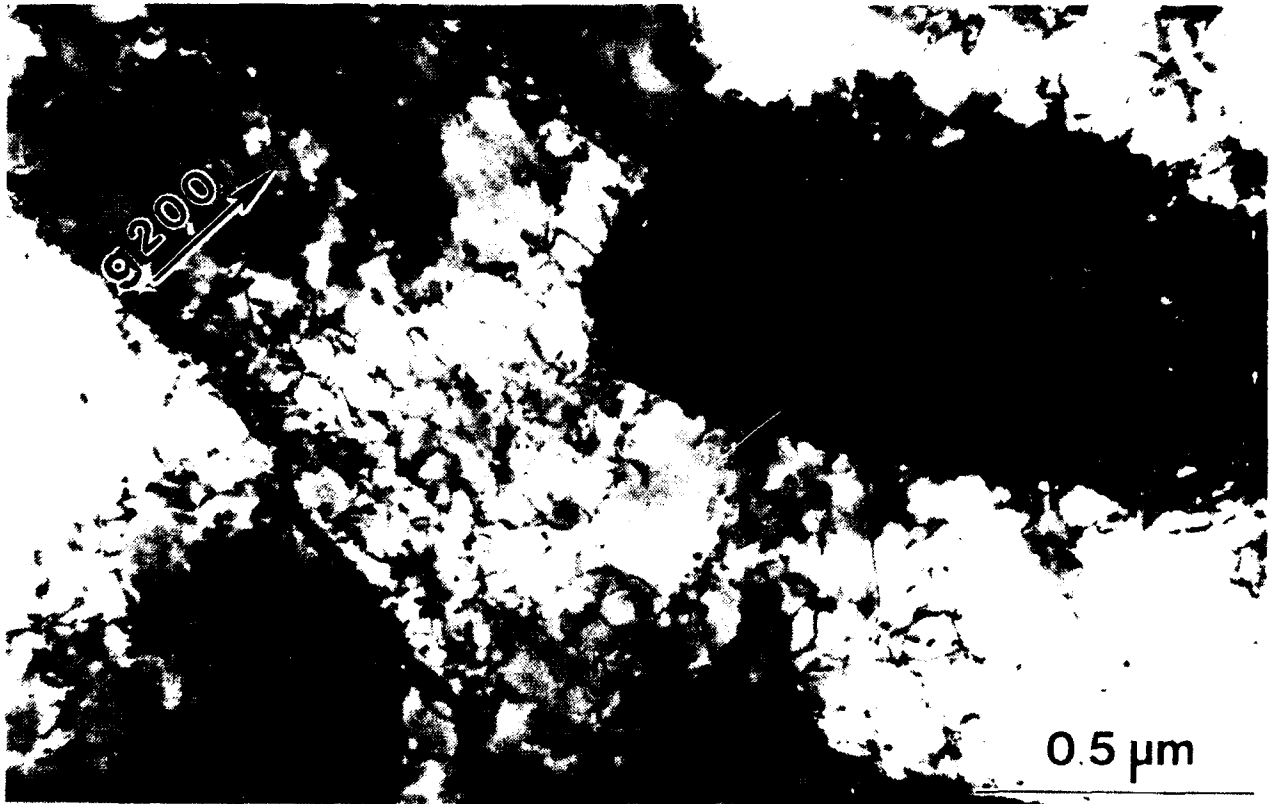


FIGURE 2. Low magnification TEM showing dislocation cell structures in a W grain formed as a result of post-sintering deformation.

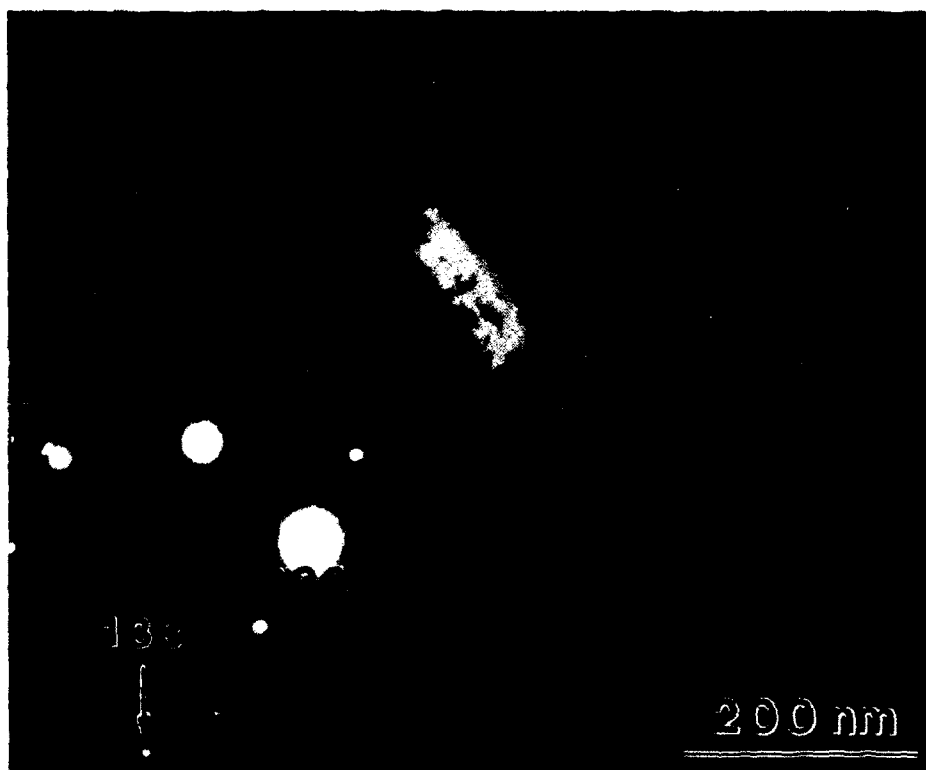


FIGURE 3. TEM results for a W-W grain boundary: (A, top) bright field, (B, bottom) dark field using a matrix phase 133 reflection (inset) showing interfacial γ precipitation, and (C, next page) EDS from precipitate showing substantial Ni, Fe and W.

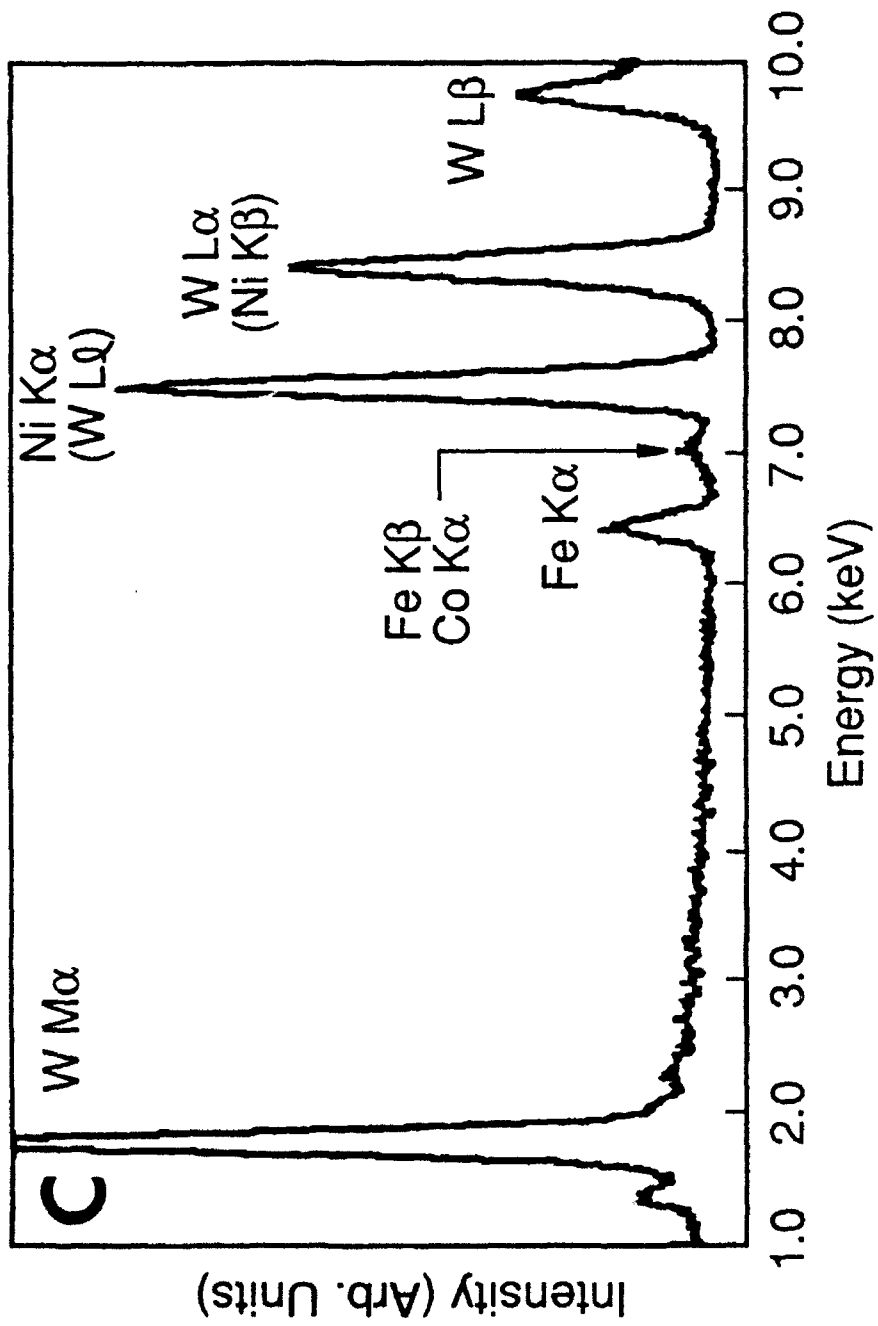


FIGURE 3, C



FIGURE 4. Dark field TEM images of the interior of a W grain: (A) two-beam image that shows the ~ 3.5 nm diameter precipitates to have black/white lobe contrast and (B) weak beam image of the same area that shows the precipitate strain contrast to be light on a dark background.

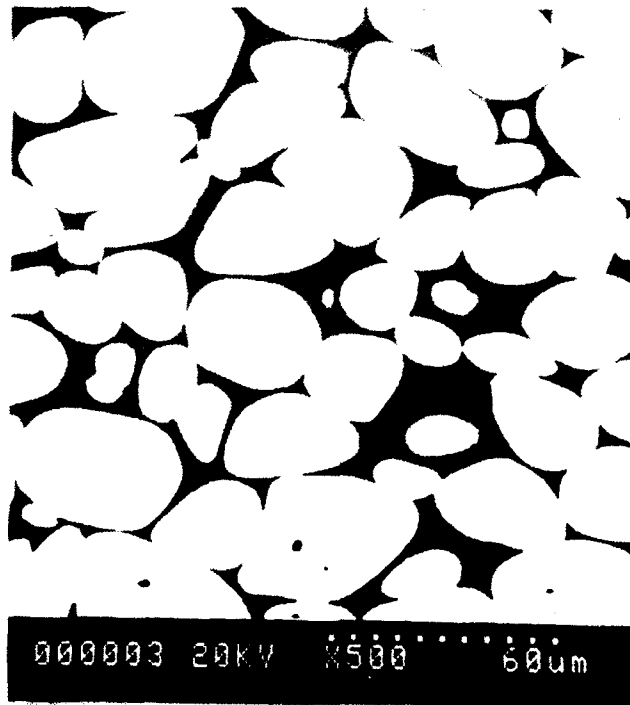


FIGURE 5. Backscattered electron SEM images from the electropolished thin foil: (A) low magnification showing several W grains, which appear light, and (B) higher magnification of a W-W grain boundary which has significant interfacial γ precipitation.

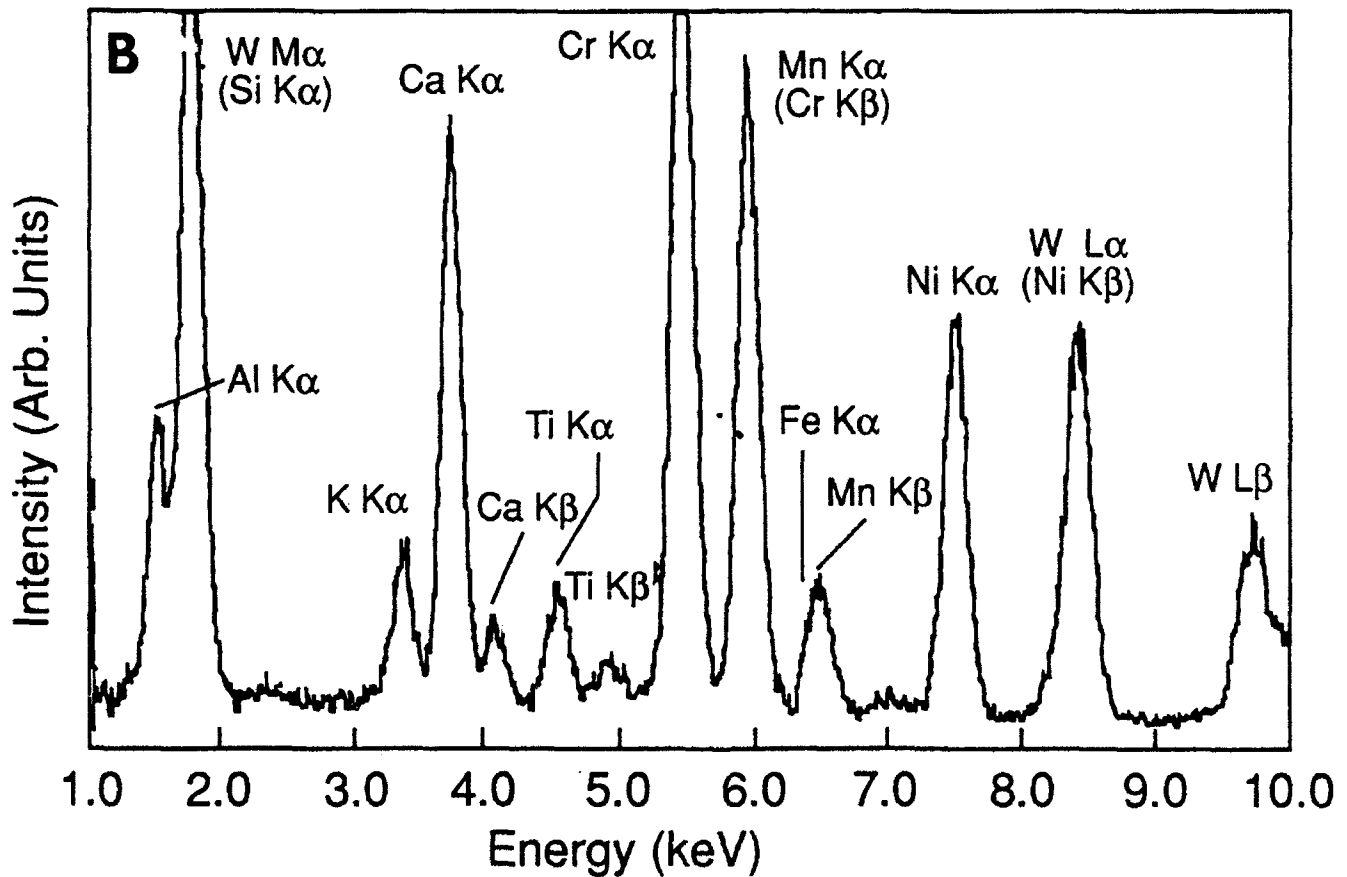
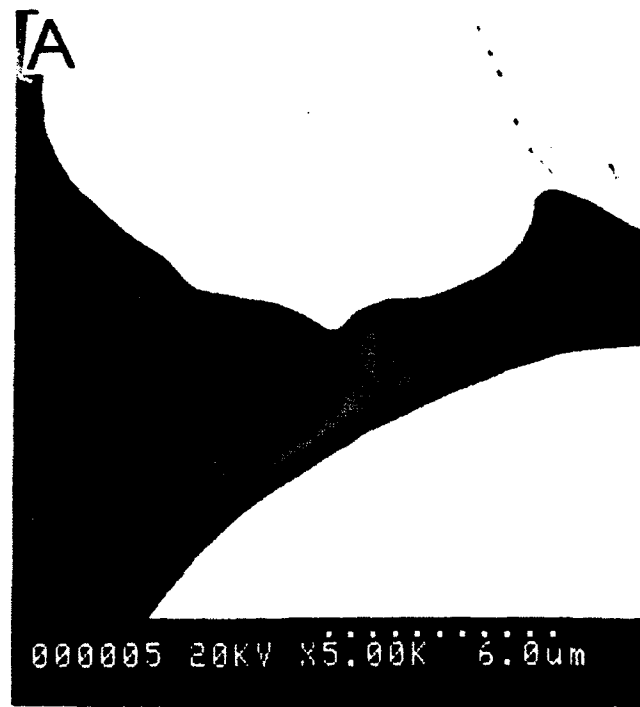


FIGURE 6. Additional SEM results from the electropolished sample showing an inclusion: (A) backscattered electron image, inclusion appears dark due to lower than average atomic number, and (B) EDS from inclusion showing the presence of several impurity elements. It is very likely that the inclusion is a complex oxide.

YIELD PROPERTIES OF TUNGSTEN AND
TUNGSTEN HEAVY ALLOYS

KENNETH F. RYAN

AND

ROBERT J. DOWDING

U.S. ARMY RESEARCH LABORATORY
MATERIALS DIRECTORATE
WATERTOWN, MA 02172-0001

Abstract

This report describes the progress made in dynamic thermo-mechanical investigations, using the Gleeble[®] 1500, of the yield properties of tungsten heavy alloys. This study describes properties of tungsten heavy alloy at elevated temperatures and strain rates, that can be useful in the modeling of long rod kinetic energy penetrator behavior.

Introduction

Tungsten heavy alloys have application as long rod kinetic energy (K.E.) penetrators if some of their properties can be improved. The goal is that they perform as well as those made from depleted uranium (DU). Penetrator applications require the highest level of toughness, strength, hardness, and ductility. Commonly, the most useful heavy alloy compositions are based upon the W-Ni-Fe ternary, with tungsten contents ranging up 97 wt pct. The balance is nickel and iron most often in a ratio of 7:3. Recent work indicates that the toughness of 8:2 nickel:iron ratios is greater than the traditional 7:3 but these have not been ballistically tested on a widespread basis [1]. Ballistic testing at the Materials Directorate of the Army Research Laboratory (formerly the Army Materials Technology Laboratory) has employed the depth of penetration (DOP) test for many tungsten alloys; most predominately those with approximately 90-93 % tungsten, with a matrix composition that contained nickel, iron, and/or cobalt. A full description of the DOP test can be found in Woolsey, et al. [2]. These results revealed that density is the only apparent driver of performance in this test. This work also demonstrated that the mechanical properties have little influence over performance in the DOP test [3]. This work supported the observations of Ekbohm, et al., who stated that strength was not a primary factor in penetration of homogenous targets [4].

GTE Sylvania (Towanda, PA) performed an extensive study on the interrelationship between chemical composition, thermo-mechanical processing history, microstructure and ballistics performance of tungsten heavy alloys. Among the significant findings of that program was that the optimum mechanical properties were attained when the nickel:iron ratio of W-Ni-Fe alloy was 8:2, instead of the traditional 7:3 which has historically been thought to be better. The 8:2 ratio had superior mechanical properties and in some cases showed slightly improved ballistic properties. In general though, no strong correlation could be drawn between the mechanical properties and ballistic performance [1].

The problem with all previous efforts to correlate mechanical properties to ballistic properties has been the use of quasistatic testing rather than testing at elevated strain rates. There has been a move lately to change this approach and evaluate the ballistic potential of penetrator alloys with high strain rate test procedures [5-8] largely employing the split Hopkinson bar apparatus, in both compression and torsion. Along with this change has been the realization that to be able to model material response of a penetrator using computer codes requires that the properties of the relevant tungsten alloy are needed rather than the properties of pure tungsten.

Previous research by Bose, et al., involved generating data on mechanical property variations with test temperature and strain rate for a common tungsten heavy alloy with a well characterized microstructure and processing history [9]. These results were gathered using tension specimens over a range of temperatures and strain rates. Data of this type and the data to be presented here can be very useful in developing materials models for ballistic interactions.

A microprocessor controlled, dynamic, thermo-mechanical test machine called the Gleeble[®] 1500, was used to determine the mechanical response of a commercially available 91% tungsten heavy alloy. This type of experimental testing can provide some of the constitutive data necessary for developing modeling and processing simulations. The ultimate objective is to determine the processing/properties/microstructure required to optimize the performance of tungsten heavy alloys for use as kinetic energy penetrators.

Evaluation of the data from elevated temperature deformation experiments depends on the choice of constitutive equations. These equations hopefully are the ones that most accurately express the material's response. It is desirable for such a constitutive model to be based on physical processes that occur within the alloy over wide ranges of temperatures and strain rates, and yet the model must contain measurable parameters from easily performed thermo-mechanical tests [10]. The present approach to describing constitutive relations for metal deformation is based on unifying the microscopic physical processes occurring during deformation [10].

The choice of model significantly affects the simplicity of the test and the number of material constants that must be determined [11]. The Gleeble 1500 is a sophisticated system to help generate the data required to describe the temperature dependent, elevated strain rate, stress-strain behavior of these tungsten heavy alloys. The experimental data can be fitted algebraically into the classic strain rate dependant equations and present a greater understanding of the material's flow behavior in terms of either strain, strain rate or temperature. Often complicated microstructural changes can occur during high temperature deformation processing. These include: strain hardening, strain aging, recovery and recrystallization. Because of this it is very difficult, if not impossible to describe the complete elevated temperature deformation behavior using a single relationship [12].

Background Theory

Many attempts have been made to fit mathematical equations to describe the steady state stress-strain rate material behavior. The simplest, and hence, most common is a power law expression of the form;

$$\sigma = A\epsilon^m \quad \text{equation 1}$$

where constant A is the stress at a strain rate of one obtained at constant strain and temperature, and m is the strain rate sensitivity as determined by the slope of a log-log plot of this equation [13]. This power law expression will most often adequately describe the dependance between flow stress and strain rate. A similar relationship can be derived for stress-strain behavior obtained at constant strain rate and temperature. By experimental observation during this study, we've found the expected relationship where increasing the strain rate increases the material's flow stress. The strain rate sensitivity of most metals is usually low at room temperatures, and increases with increasing temperature; especially at temperatures greater than half the melting point [14]. The temperature range investigated here is well below the melting temperature (T_m) of pure tungsten but is much above $0.5 T_m$ of the multi-

component matrix phase. This can be expected to cause difficulty in interpreting the data of this two-phase composite.

The temperature dependence of the flow stress at constant strain and strain rate can be represented by the relationship known as the Arrhenius equation:

$$\sigma = C \exp(Q/RT) \quad \text{equation 2}$$

Where Q = activation energy, R = the universal gas constant, T = test temperature (°K) and C = a material dependent constant. A plot of $\ln \sigma$ versus $1/T$ will yield a straight line with a slope of Q/R . This allows the simple calculation of the activation energy at all temperatures and strain rates and is obtained from the material's flow stress behavior. The magnitude of the activation energy is indicative of the metallurgical processes occurring during deformation, such as, strain aging or recrystallization. Previous hot working studies performed by Tuler provide a perception that thermally activated processes assist deformation and reduce the flow stress at elevated temperatures [14].

Experimental Procedure

Cylindrical specimens 0.245" in diameter and 0.368" long (L/D=1.5) were machined from a 91% tungsten heavy alloy purchased from a commercial source. The ends of these compression specimens were ground flat and parallel within $\pm 0.0005"$. Additionally, they were designed to minimize the possibility of buckling when loaded on end. The quasistatic properties and the chemical content of the major constituents of the tungsten heavy alloy chosen for this testing are presented in Table 1.

The Gleeble 1500 test set-up can be seen in Figure 1. The specimen was compressed between two tungsten carbide anvils with graphite as a lubricant to prevent excessive barreling of the specimen during testing. The temperature range for the compression testing was 500° to 1000° C and the heating was accomplished by electrical resistance and monitored by a thermocouple. The average strain rates were in the range of 10^{-2} to 10^{-1} sec^{-1} and the total compressive strain applied was 20%. These strain rates bridge the gap from quasistatic to dynamic. Figure 2 graphically describes the test procedure used for this work. Note that the 1200° C anneal prior to compression was required since the supplied material was previously swaged. The cooling rates to each of the test temperatures varies because free cooling to those temperatures was used and no attempt was made to control the rate.

TABLE 1
ROOM TEMPERATURE, QUASI-STATIC MECHANICAL PROPERTIES
AND
CHEMICAL ANALYSIS OF TUNGSTEN HEAVY ALLOY

0.2% YIELD STRENGTH (MPa)	UTS (MPa)	REDUCTION IN AREA (%)	ELONGATION (%)
1167	1178	16.8	11.9
TUNGSTEN (wt%)	NICKEL (wt%)	IRON (wt%)	COBALT (wt%)
90.73	4.55	1.97	2.75

Results and Discussion

Figure 3 shows the thermo-mechanical response of the 91% tungsten heavy alloy at strain rates in the range of 1.6 to $1.8 \times 10^{-2} \text{ sec}^{-1}$. The figure shows the expected result that the yield strength and flow strength decrease with increasing test temperature. Figure 4 displays the strength at a total strain of 0.002 versus test temperature for each of the strain rates used. Also plotted is data for room temperature compression of the as-annealed specimens. The 0.002 strength data was obtained directly from the data acquisitions and not graphi-

cally from the plots shown in Figure 3. This results in a more accurate interpretation of the yield data.

Figure 5 describes the temperature dependence of flow stress of the heavy alloy at the two temperature extremes and the two average strain rates examined in this work. This figure shows the expected result that yield and flow stress increases with increasing strain rate.

Figure 6 summarizes the data obtained in terms of equation 1 where the slope of the curve represents the strain rate sensitivity (m). The strain rate sensitivity of metals increases with increasing temperature and is an indicator of changes in deformation behavior. In a composite material such as this heavy alloy, the elevated deformation behavior is complicated by the differing properties of the two phases. Whereas the matrix has a melting point of approximately 1453° C the tungsten particles melt at over 3300° C. The strain rate sensitivity is said to increase significantly over 0.5 T_m . The strain rate sensitivity as determined here is somewhat constant up to 800° C but apparently increases at 1000° C. This may be because the temperature exceeds 0.5 T_m of the matrix by a significant degree. Certainly more data must be obtained to determine if this observation is correct.

Figure 7 is an Arrhenius plot based on equation 2. The slope of the line is the activation energy (Q) of the deformation event at the strain rates given. It is apparent from an examination of this data that there are two deformation regimes; one below 800° C and one above. The activation energies below 800° C were calculated to be 4.33 and 5.02 kJ/mole for the strain rates 1.75×10^{-2} and $1.84 \times 10^{-1} \text{ sec}^{-1}$ respectively. Above 800° C the activation energies were found to be 27.44 and 34.03 kJ/mole respectively. Since the strain rates used here are relatively close, only one order of magnitude different, the activation energies are nearly identical.

Summary and Conclusions

Cylindrical compression tests were conducted on a 91% tungsten heavy alloy in the temperature range 500-1000° C to a total strain of 20% using two average strain rates of 1.84×10^{-2} and $1.75 \times 10^{-1} \text{ sec}^{-1}$. The alloy exhibited the expected strain and strain rate hardening, as well as, thermal softening. The strain rate sensitivity at 1000° C was found to be slightly higher than at lower temperatures but this observation needs to be verified with additional data. Very little variation in the activation energy was noted for the two strain rates examined. This was attributed to the small difference between them. More testing is required to verify data obtained and to extend to envelope of information.

References

1. J.R. Spencer and J.A. Mullendore, "Relationship Between Composition, Structure, Properties, Thermo-Mechanical Processing and Ballistic Performance of Tungsten Heavy Alloys", U.S. Army Materials Technology Laboratory, Watertown, MA 02172-0001, MTL TR 91-44, November 1991.
2. P. Woolsey, D. Kokidko and S.A. Mariano, "Alternative Test Methodology for Ballistic Performance Ranking of Armor Ceramics", U.S. Army Materials Technology Laboratory, Watertown, MA 02172-0001, MTL TR 89-43, April 1989.
3. R.J. Dowding, K.J. Tauer, P. Woolsey and F.S. Hodi, "The Metallurgical and Ballistic Characterization of Quarter-Scale Tungsten Alloy Penetrators", U.S. Army Materials Technology Laboratory, Watertown, MA 02172-0001, MTL TR 90-31, May 1990.
4. L. Ekbohm, S. Bogegård, L. Holmberg and L. Westerling, Proceedings 9th International Symposium on Ballistics, pp 2-447 to 2-456, 1986.
5. D. Chaiat, Proceedings of 1986 P/M in Defense Technology Seminar, MPIF, Princeton, NJ, pp 1-13, 1986.
6. A. Bose, S.C. Yang and R.M. German, Proceedings of 1991 P/M Conference and Exhibition, Vol. 6, Chicago, MPIF, Princeton, NJ, 1991, pp 425-437.
7. A. Bose, H. Couque and J. Lankford, Jr., Proceedings of 1992 P/M World Congress, San Francisco, MPIF, Princeton, NJ, in press.
8. T. Weerasooriya, P.A. Beaulieu and R. Swanson, these proceedings.
9. A. Bose, D. Sims and R.M. German, Metallurgical Transactions A, vol 19A, March 1988, pp 487-494.

10. A.K. Ghosh, *Acta Metallurgica*, vol 28, Pergamon Press, 1980, pp 1443-1465.
11. G.A. Henshall and A.K. Miller, *Acta Metallurgica*, vol 37, Pergamon Press, 1989, pp 2693-2704.
12. K.P. Rao and E.B. Hawbolt, *Transactions of the ASME, Journal of Engineering Materials and Technology*, vol 114, 1992, pp 116-123.
13. G.E. Dieter, *Mechanical Metallurgy*, 2nd Ed., McGraw-Hill, Inc., 1976.
14. J.T. Beals, C. Demetry and F.R. Tuler, "High Temperature Deformation of Silicon Carbide-Reinforced 6061 Aluminum Metal Matrix Composites", Worcester Polytechnic Institute, Worcester, MA, Proj. No. FRT-8782, 1988.

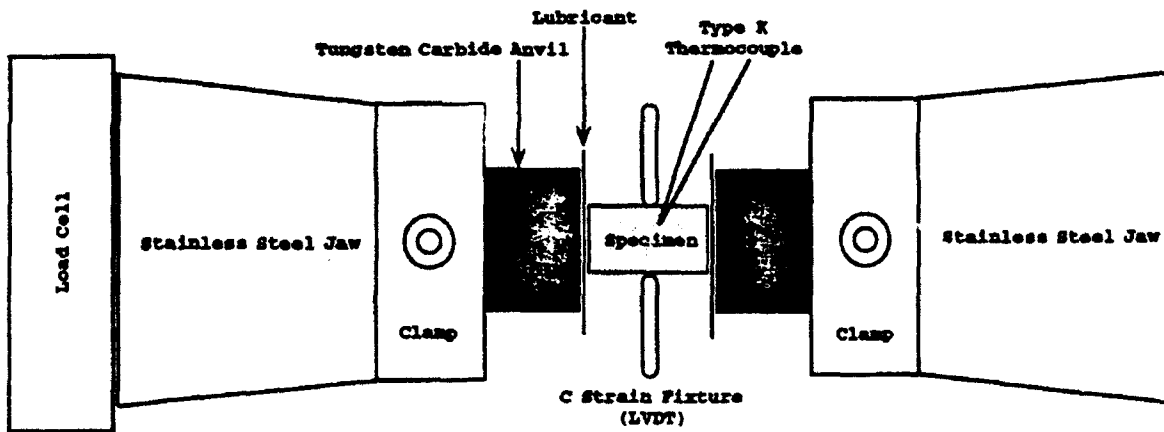


Figure 1 Schematic Drawing of the Gleeele 1500 Compression Testing Equipment

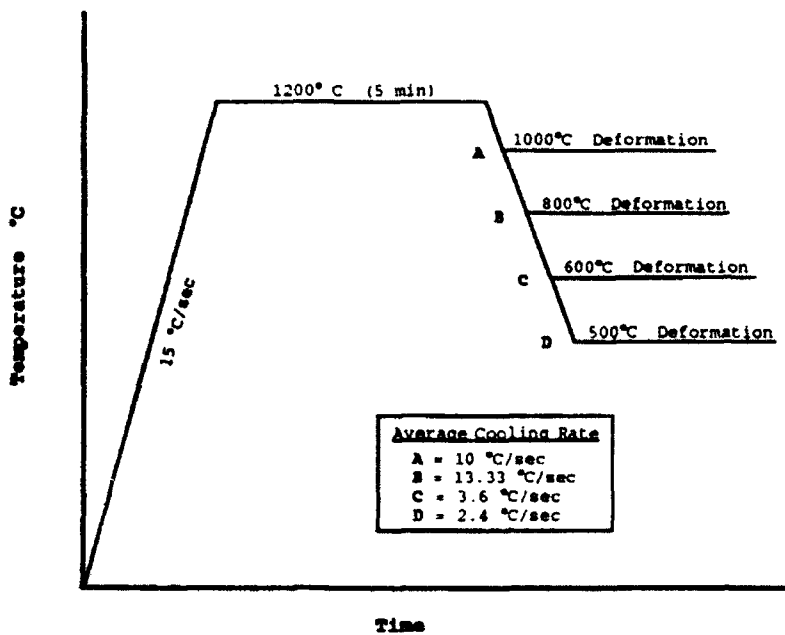


Figure 2 Thermal Profiles for Specimens Prior to Deformation, Includes 1200°C Stress Relief and Free Cool, in Vacuum to the Test Temperature. Heating and Cooling Rates are Shown.

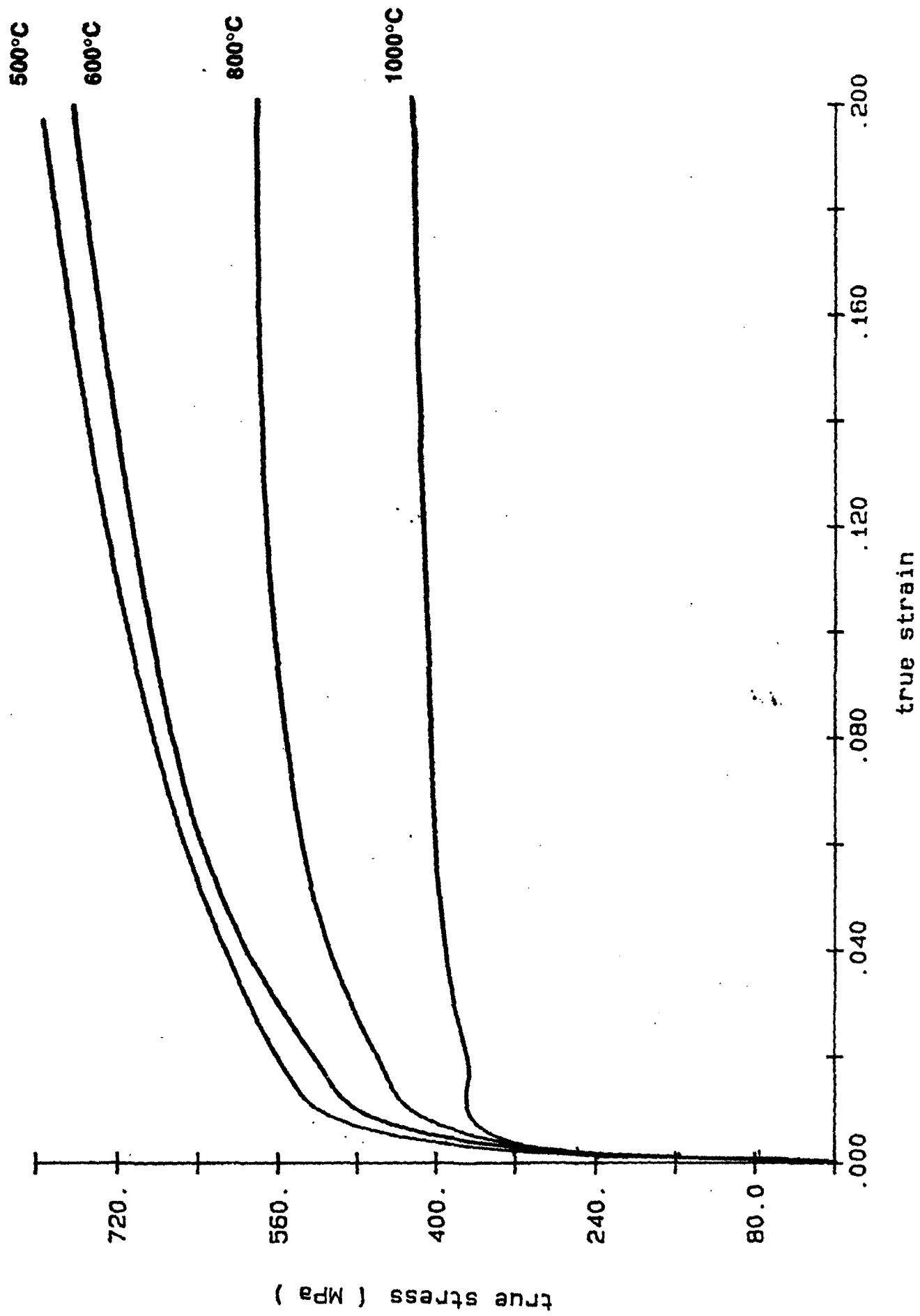


Figure 3 Thermo-mechanical Response at a Constant Strain Rate In the Range ($1.6 - 1.8 \times 10^{-2} \text{ sec}^{-1}$)

True Stress at 0.002 Total Strain vs. Test Temperature

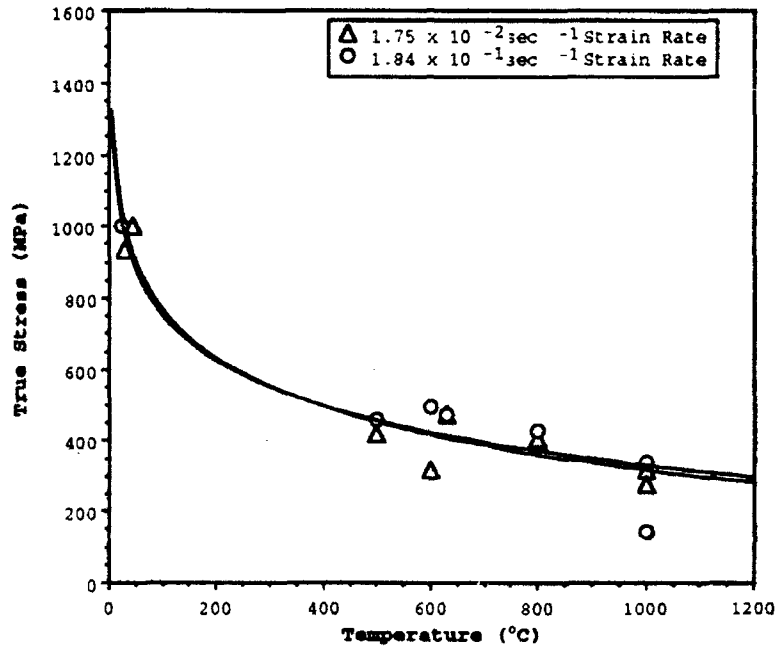


Figure 4 True Stress at 0.002 Total Strain at Two Different Average Strain Rates

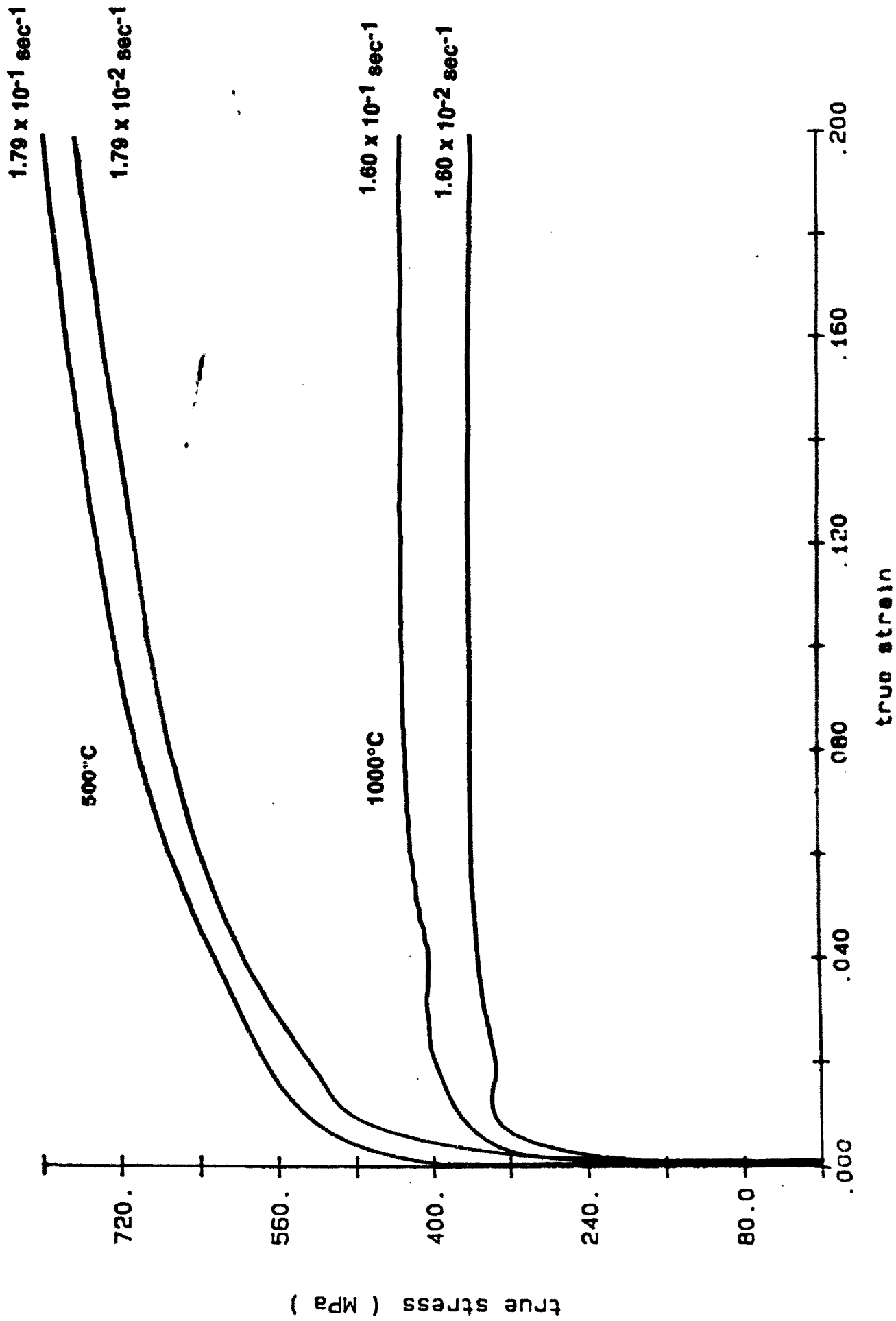


Figure 5 Temperature Dependence at 500°C and 1000°C

Power Law Plot of Flow Stress at 0.1 True Strain
vs. Average Strain Rates at Test Temperatures

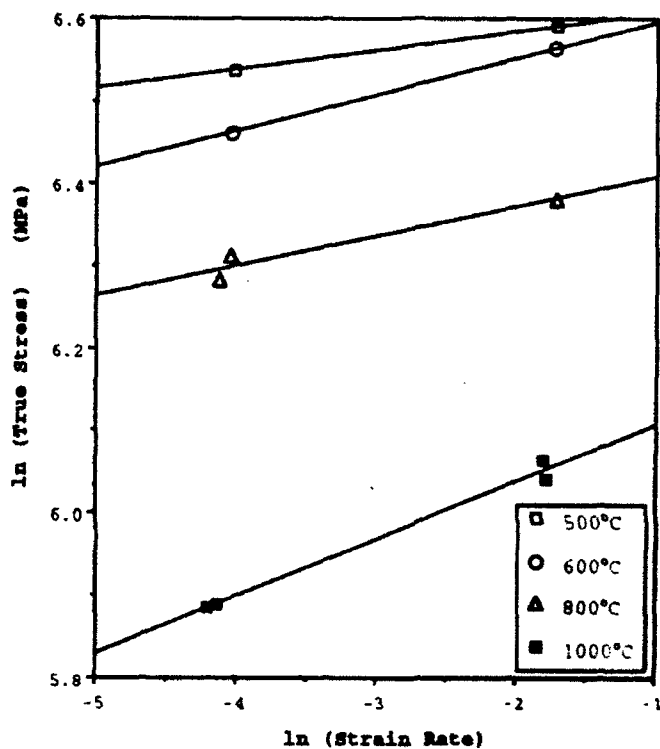


Figure 6 Power Law Plot of Flow Stress
Versus Average Strain Rates at
Various Test Temperatures

Arrhenius Plot of Flow Stress at Strain of 0.1
Versus Reciprocal Temperature

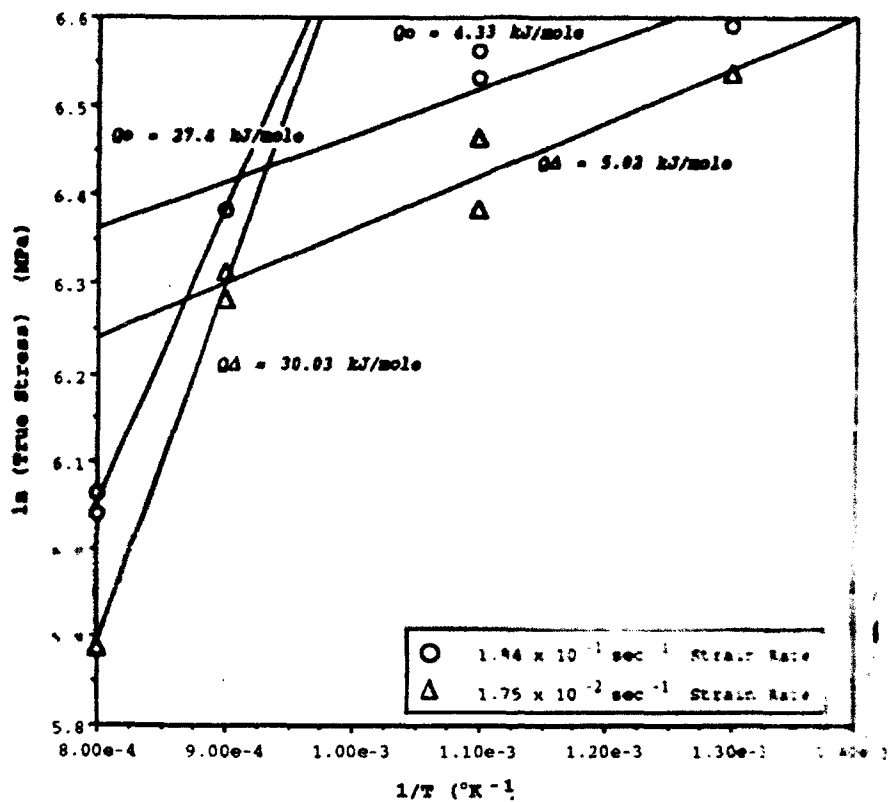


Figure 7

Arrhenius Plot of True Stress
Versus Reciprocal Temperature

**BALLISTIC PERFORMANCE OF A COATED POWDER
TUNGSTEN ALLOY**

KENNETH J. TAUER, ROBERT J. DOWDING

AND

PATRICK WOOLSEY

**U.S. ARMY RESEARCH LABORATORY
MATERIALS DIRECTORATE
WATERTOWN, MA 02172-0001**

Abstract

The results of a recent tungsten alloy development program undertaken by the U.S. Army Materials Technology Laboratory to produce improved penetrator material are detailed. The objective of the program was to impart strength and toughness increases in the alloy by eliminating tungsten grain contiguity in the final microstructure. To achieve this end, a Ni+Fe coating was applied to tungsten powder, followed by dynamic consolidation using the Ceracon[®] process, in order to retain the coating. Physical, mechanical and microstructural features of the resultant alloy were characterized. Ballistic performance data were obtained for penetrators fabricated from this material in both semi-infinite penetration and plate perforation modes. The results for this alloy are compared with results obtained with commercial alloys having similar tungsten content.

Introduction & Background

Tungsten heavy alloys have been considered as a substitute for depleted uranium as kinetic energy penetrators for a number of years. Both materials have essentially equivalent high densities and comparable physical properties. Both are also in sufficient supply and of comparable price, and the primary consideration favoring WHA is an environmental one. With increasing importance being placed on environmental concerns, including those related to degradation, as well as those resulting from handling and use, the preference for WHA has mounted and correspondingly, effort has been directed to develop composition and thermo-mechanical processing which will bring the ballistic performance of the WHA to equal or better that of DU. Intuitively, and directed by computer solutions of the ballistic encounter, researchers have directed their efforts toward improved physical and mechanical properties. For many years efforts to increase ultimate strength, hardness impact strength, toughness, transverse strength, etc. have yielded favorable results. However, these improvements generally did not result in significant improvement in ballistic performance. As a result of this lack of correlation, efforts were, and are, directed toward improving these properties at higher strain rates, at which the ballistic encounter takes place. Moreover, the variation of the properties with strain, strain rate and temperature are of major concern in understanding a material behavior in a ballistic encounter. Due to the essentially adiabatic behavior in ballistic events, the temperature dependence of properties probably takes on a special importance.

Recently Magness and Farrand¹ have deduced, from an extensive study of the penetration of various WHA and DU quarter scale penetrators, that there is a significant difference in the diameter of the resulting hole in the armor from equivalent diameter projectiles. They ascribe this difference to an increased

mushrooming of the interaction zone of the WHA penetrator, while the DU penetrator is prevented from build-up of a large mushroom-like head by a series of sequential adiabatic shear zones which allow for and cause a sloughing off of the accumulating material of the penetrator in the ballistic interaction zone. A generation ago, this effect was described as a self-sharpening penetrator, without further explanation. Recent efforts have been directed to introducing adiabatic shear tendencies into WHA.

In discussing these two materials, WHA and DU, and reasoning and planning by analogy from one to the other, the significant differences between the two materials must be kept in mind. WHA are two-phase materials of very different properties which may be logically called composites. In contrast to DU, which is a monolithic alloy, the matrix of the tungsten heavy alloy is a ternary or quaternary of iron, cobalt and nickel of varying compositions saturated at its melting temperature with tungsten which is generally in the range of 25 weight percent. The crystallographic structure is face centered cubic. Metallurgically it is, at room temperature one of the following; a) supersaturated solution of W in the matrix composition, or b) micro-precipitated W in the matrix, or c) macro-precipitated W in the matrix depending of the rate of cooling. The tungsten phase consists of essentially pure tungsten single crystals of size in the range 20-40 micrometers which exhibit remarkable ductility in the ballistic encounter and also in hydrostatic extrusions. The tungsten grains thus behave as nearly pure, defect free, and notch free single crystals. The net result is that WHA is a composite of vastly differing components in density, melting temperature, ductility, strain hardening characteristics and ageing characteristics. These two components are made into a cohesive material by the tungsten-matrix grain boundary energy of cohesion. This variable is subject to modification, which provides the basis for the approach reported here.

A method of coating the tungsten powder with the matrix composition at increased purity or with specified adulterants has been developed through Small Business Innovative Research (SBIR) contracts with Ultramet². Figure 1 shows the basis system of fluidized bed coating for CVD matrix materials on tungsten. This system is available to tailor the W-matrix grain boundary energy by the removal of undesirable elements which congregate at the grain boundaries or the introduction of desirable elements in part per million range for beneficial effects on the grain boundaries. Thus an approach is available to tailor the grain boundaries to, for example, varied overall ductility or frangibility levels to prevent the build-up of a mushroom head³. This could be an alternative, in the case of a composite, to the introduction of adiabatic shear instability. Always, properties must be sufficient to allow for the launch of the projectile system.

Description of Material & Processing

The very large number of combinations of compositions, processing, purity and subsequent deformation and aging requires a method of screening ballistic performance against a variety of targets. A common method is the quarter scale test in which a 65 gram (1000 grain) penetrator with a length to diameter (L/D) ratio of ten, fifteen or twenty is fired at representative velocities against suitable representative quarter scale targets. Results reported here include those performed at AMTL, and also results of 24 gram penetrators with an L/D of eight tested at Alliant Techsystems against both monolithic and multiple high obliquity spaced targets.

The starting materials and processing are a departure from the normal path of mixing powders followed by pressing and liquid phase sintering. In this process, commercial tungsten powders in the 10 micron range, which may or may not be screened to more uniform size fractions, are CVD coated with the matrix alloy. Figure 1 diagrams the process, which is a development of Ultramet in Pacoima, California. The process is being continually improved, thus giving finer control of compositions, purity of the matrix coat and/or additions of minority or parts per million components to tailor the tungsten grain-matrix bond strength. The principal virtue of the coated powder method is the ability to control the extent of contiguity and to control grain wetting, dihedral angles and bond strength. The method of consolidation; similarly, represents a departure from the normal and is primarily an effort to prevent the growth of the tungsten grains which in normal liquid phase sintering grow from the starting size of five to fifteen microns and of irregular shape to thirty to forty micron single crystal type of nearly spherical grains. These latter exhibit an exceptionally large ductility in the ballistic encounter, which leads

to large mushroom heads in the penetrator interaction zone. This is assumed to represent an excessive expenditure of penetrator energy per unit distance of penetration. To prevent this, consolidation is therefore effected at a moderate temperature, i.e. significantly less than liquid phase temperature, and by a higher strain rate method. An idealized process would have a processing temperature below the liquid phase temperature but would provide the increase in temperature caused by the localized deformation for the rapid consolidation to elevate the temperature above the liquid phase temperature. This process has been developed by Ceracon® of Sacramento, California; it is also being continually improved in control of parameters. A virtue of the elimination of the major tungsten grain growth during the LPS is the usual gain in property improvements for fine grained materials. Figure 2 diagrams the Ceracon process. The consolidation process is quasi-isostatic by virtue of the ceramic pressure transferring medium. Initial samples generally exhibited more porosity than typical LPS samples. It remains to be determined whether this can be utilized in efforts to reduce the tendency to mushrooming by the WHA penetrators.

Procedures and Results

The CVD coated tungsten powders were consolidated by three different methods, namely a) traditional CIP in the 30 ksi range followed by LPS⁴, b) HIP processing of the coated powders sealed in evacuated steel cans and heated to solid state sintering temperatures under pressures in the 40 ksi range, and c) the Ceracon process in which the green coated powder compacts are treated under pressures to 210 ksi at temperatures to 1000°C, where a ceramic particulate acts as pressure transmitting medium resulting in a quasi-isostatic pressure condition⁵.

The Ceracon process differs from the previous two by the availability of higher pressures and higher temperatures, and by significantly shorter processing times, i.e. processing times are in the range of minutes rather than hours. The traditional LPS did not result in 100% dense samples, primarily because of the uniformly sized tungsten powders used in the coating process. This could be overcome by a range in size or addition of uncoated powders to the coated powder sample. The HIP samples require additional work to optimize processing parameters to obtain desired microstructure and properties. In general, liquid phase temperatures result in extensive tungsten grain growth and a matrix saturated with dissolved tungsten. The Ceracon process can reduce or eliminate these two by having temperatures slightly below liquid phase and short processing times. EDX scans of Ceracon-processed coated powders show little or no dissolved tungsten in the matrix. This almost certainly will change the strain hardening and the ageing characteristics of the matrix, and offers an additional parameter to adjust the material response. Also, at the present state of development, the Ceracon process yields a volume dependent porosity, so that the surface of processed samples have a 0.5 to 1.0 volume percent porosity. In principle the surface porosity can be machined away, but zero porosity throughout processed samples would be preferable. It is not inconceivable that porosity can be used as an ally in reducing the mushrooming tendency of WHA, perhaps enhancing the propagation of incipient shear instabilities. In a composite such as WHA, one cannot expect to get both phases to shear locally under the same conditions. Thus we must focus on one, probably the matrix, and mitigate the delocalizing effect of the tungsten grains so that the instability can propagate. To this end, a decrease in tungsten grain size would decrease the blunting effect of the grains on matrix shear bands. Similarly, properly elongated tungsten grains, those with the grain long direction parallel to shear fracture direction will aid shear band propagation (i.e. decrease the blunting effect of tungsten grains).

The metallographic structure of the CVD coated powders consolidated by the Ceracon process are shown in Figures 3 and 4. Figure 3 demonstrates the uniformity of matrix distribution, and Figure 4 demonstrates that at higher magnification, areas which appear to have tungsten-tungsten contact show matrix between the grains.

Mechanical testing of the Ceracon samples consisted of three point flexural tests, un-notched Charpy tests and tensile tests. Data from the flexural test are listed in Table I and yield some of the highest values in combined ultimate strength and deflection as compared to conventionally processed materials. Ultimate strengths in excess of 300 ksi are recorded with significant deflection. Un-notched Charpy's in the miniature 5mm square configuration did not meet conventional values of equivalent samples of LPS

material. Values were in the range of 1.3 to 1.5 ft-lbs, compared to the usual 5 to 10 ft-lbs of LPS samples. Perhaps the residual porosity of the coated Ceracon consolidated samples resulted in lower energy absorption. Tensile strengths and elongation were also low compared to conventional material, particularly evident with elongation in the range of 1% and UTS at 145-150 ksi. Again, residual porosity probably results in the low elongation, and it remains to be determined whether a) it can be eliminated by optimized processing, and b) whether it is desirable to eliminate it at all.

Ballistic testing gave indeterminate results. Against semi-infinite monolithic RHA in depth of penetration (DOP) tests, the coated material yielded results, as shown in Figure 5, essentially equivalent to the baseline results obtained with conventionally processed WHA materials. A complete description of the DOP test can be found in Woolsey, et al⁵. This result is in accordance with results as summarized by Magness¹ and others^{6,7} that in such a test, properties other than density and velocity have a minimum effect. However, in limited testing at Alliant Techsystems, the Ceracon-consolidated coated powders were compared to two commercial WHA materials, one domestic and one foreign, and exceeded both of these in a DOP test by 11 and 13% respectively.

Against multiple high obliquity targets as tested by Alliant Techsystems⁸, the Ceracon-consolidated coated powders did not equal equivalent conventional WHA in resistance to high strain rate deformation and fracture. The measure of performance in these tests was the penetrator residual mass after penetration of the multiple layer targets. Using this measure, the coated powder was different in that, while the residual mass was very similar to the two commercial WHA, there were significantly more residual pieces, indicating more extensive material fracture from impact loading. This is very probably due to the residual porosity found in these samples. It remains to be seen if optimized parameters of time, temperature and pressure in the Ceracon process will eliminate this porosity, or whether in fact, the porosity can be utilized to reduce the mushrooming.

Summary and Conclusions

1. The CVD method for coating matrix materials onto tungsten powder particles has been established to deposit the matrix in the desired amount, in either a state of purity or with additional trace elements to tailor the grain boundary strength for specific material response.
2. A uniform size powder is most easily handled in the fluidized-bed CVD processing, but LPS consolidation is most easily affected by a distribution of sizes.
3. The solid state consolidation process developed and registered by Ceracon is conducted generally below liquid phase temperatures, at high pressures in the range of 200 ksi which are rendered pseudo-isostatic by a particulate ceramic pressure transmitting medium, and at short times, namely several minutes rather than an hour or more.
4. The results of consolidation via the Ceracon process are: a) the CVD matrix remains essentially in the region surrounding the grain where it was deposited, therefore reducing the contiguity of the consolidated sample, b) Tungsten grain size remains, because of short times and lower than liquid phase temperatures, essentially equal to that in the starting powder, and c) Limited dissolution of tungsten into the matrix takes place, again due to short processing times and low temperatures.
5. The consolidated samples had a residual porosity of approximately one volume percent; this was detrimental to multiple high obliquity target performance but did not apparently degrade the penetration efficiency against a monolithic target.
6. Post-mortem analysis of the Ceracon-consolidated CVD coated powder material fired in DOP tests demonstrated behavior similar to that observed for WHA consolidated by more conventional methods; namely, the existence of a highly deformed region within a few millimeters of the penetrator target boundary, separated by a sharp boundary from the completely undeformed penetrator material directly behind the highly deformed region. This is shown in Figures 6 and 7.

7. In the DOP test results, the residual length, mass, and mushroom diameters of these penetrators fall within the statistical spread exhibited by the commercial WHA.

8. It remains to be established whether residual porosity and/or manipulation of grain boundary energies by the elimination or addition of trace elements in the CVD coating process can be used to reduce or eliminate the mushrooming tendency of the WHA in the ballistic encounter.

References

1. L.S. Magness and T.G. Farrand, "Deformation Behavior and its Relationship to the Penetration Performance of High-Density KE Penetrator Materials", Proceedings of the 1990 Army Science Conference, Durham, NC.
2. B.E. Williams, J.J. Stiglich and R.B. Kaplan, "Coated Tungsten Powders for Advanced Ordnance Applications, Phase II", USAMTL TR 92-35, 1992.
3. B.E. Williams and J.J. Stiglich, "Adiabatic Shear Behavior in Titanium, Hafnium and Hafnium-Coated Tungsten Powders for Kinetic Energy Penetrators", USAMTL TR 92-36, 1992.
4. S. Mulligan and R.J. Dowding, "Sinterability of Tungsten Powder CVD Coated with Nickel and Iron", USAMTL TR 90-56, 1990.
5. P. Woolsey, S. Mariano and D. Kokidko, "An Alternative Test Methodology for Ballistic Performance Ranking of Armor Ceramics," USAMTL TR 89-43, April 1989.
6. R.J. Dowding, K.J. Tauer, P. Woolsey and F.S. Hodi, "The Metallurgical and Ballistic Characterization of Quarter-Scale Tungsten Alloy Penetrators", U.S. Army Materials Technology Laboratory, Watertown, MA, 02172-0001, MTL TR 90-31, May 1990.
7. P. Woolsey, F.S. Hodi, R.J. Dowding and K.J. Tauer, "Performance-Property Relationships in Tungsten Alloy Penetrators", these proceedings.
8. T. Steigauf, Alliant Techsystems, private communication, June 1992.

Acknowledgements

The authors would like to extend their thanks to the many individuals who assisted in the performance of this work. They particularly appreciate the contributions of Dr. Jack Stiglich of Ultramet Co. for providing much material property information, and Mr. Thomas Steigauf of Alliant Techsystems for developing and providing much of the ballistic test information.

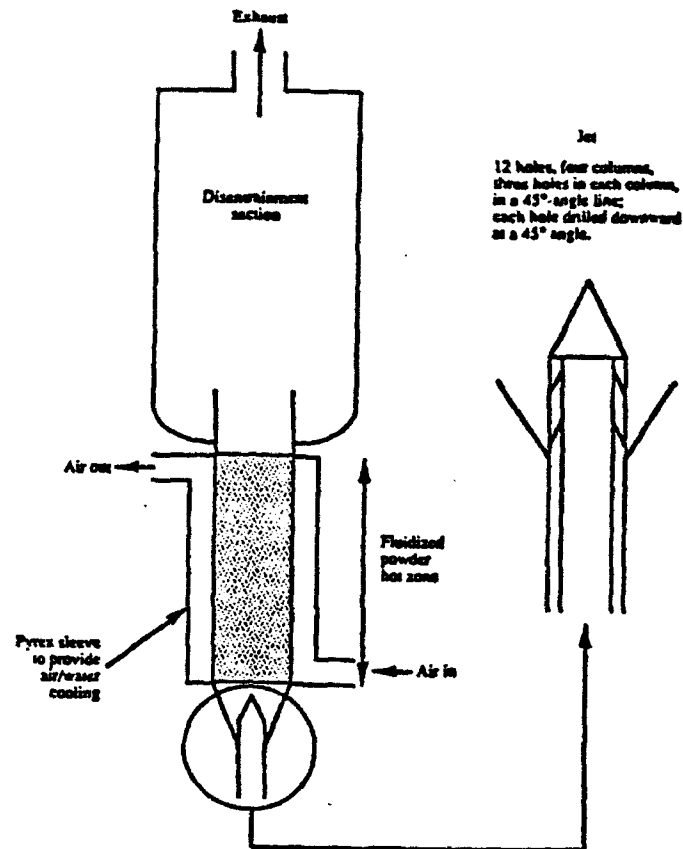


Figure 1. Schematic of Fluidized-bed CVD apparatus.

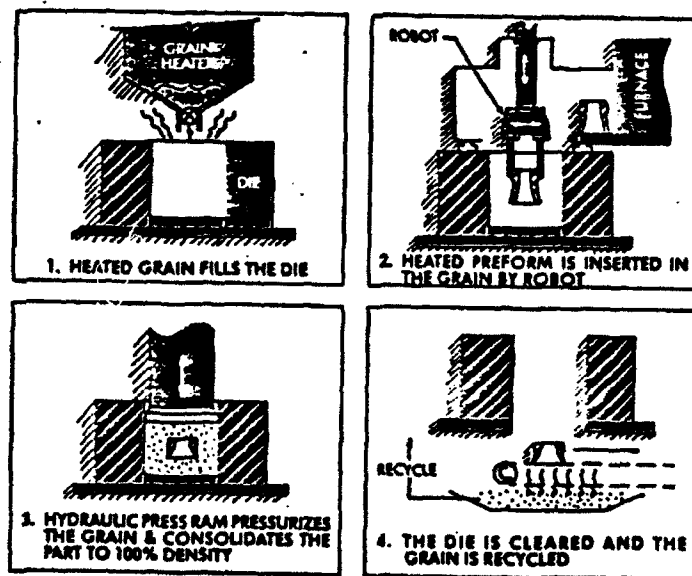


Figure 2. Schematic of Ceracon[®] consolidation process.

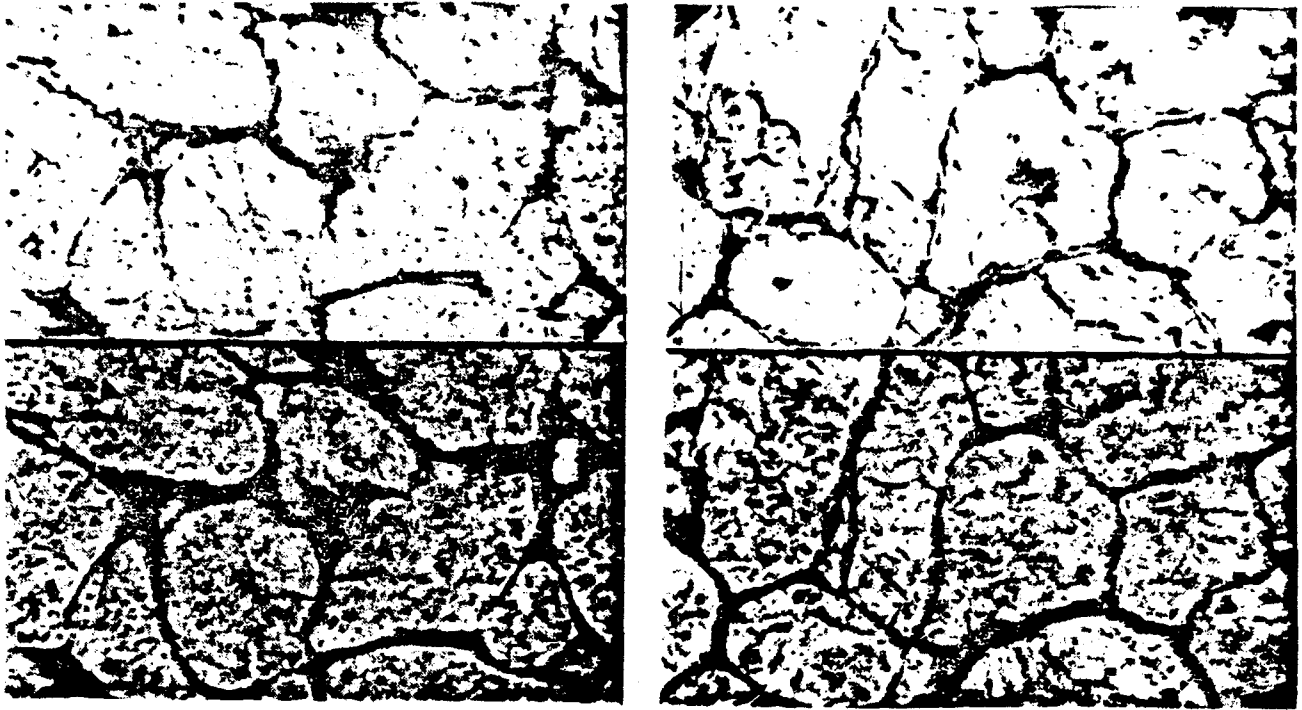


Figure 3. SEM micrographs of coated tungsten powder, W-3.5Ni-1.5Fe, consolidated by Ceracon. Secondary electron image (top), backscattered electron image (bottom).

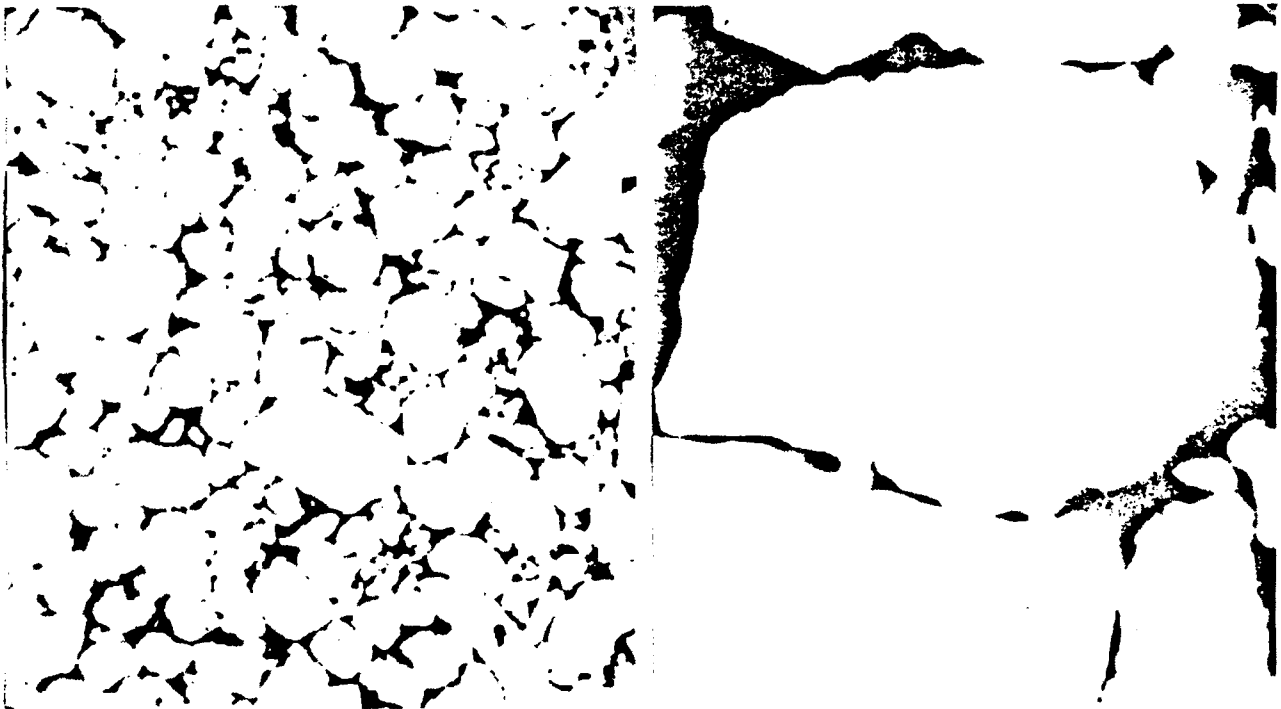


Figure 4. SEM micrographs, large billet consolidation. The right hand micrograph shows matrix between the tungsten grains that is not apparent at lower magnification.

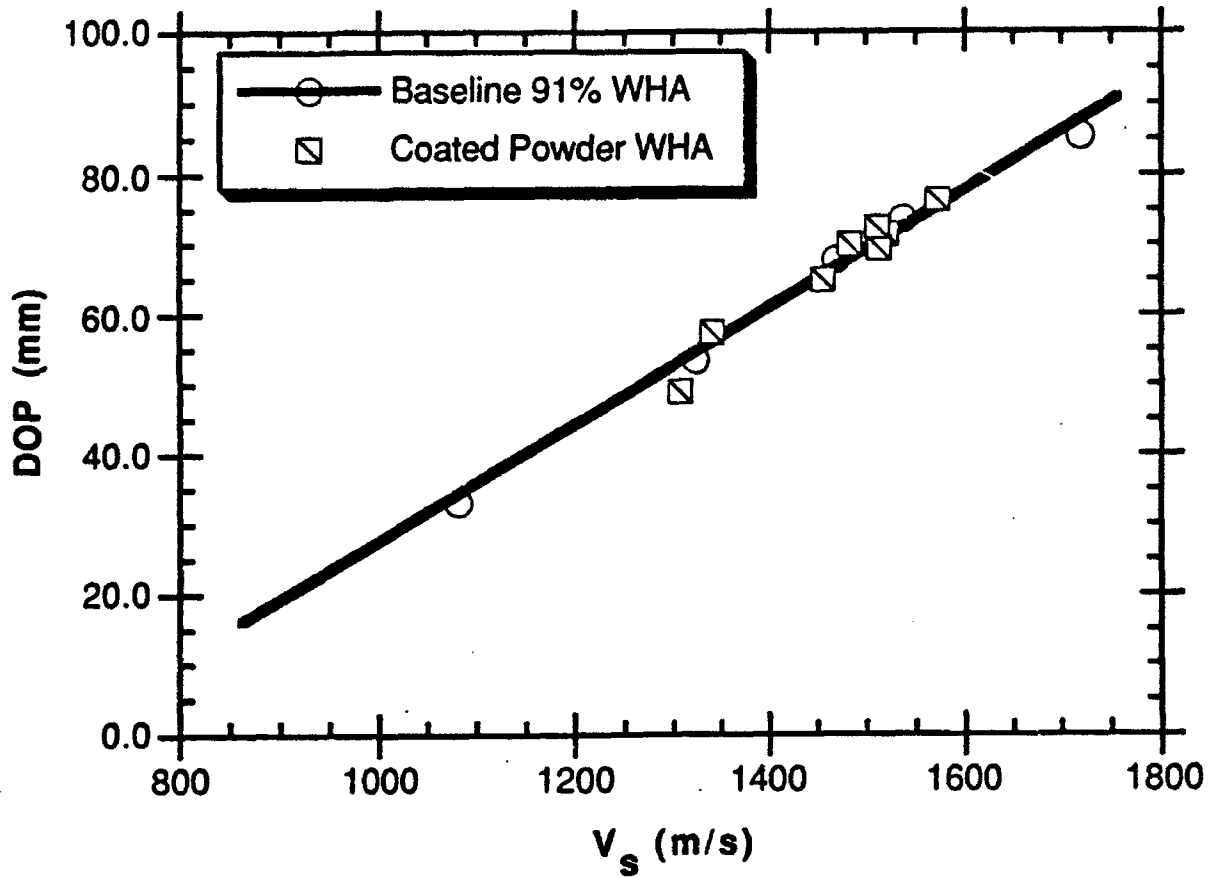


Figure 5. Ballistic depth of penetration test results shown in comparison to the baseline 91% tungsten alloy.

Length (in) (mm)	0.5625 14.288						
Width (in) (mm)	0.1488 3.780	0.1492 3.790	0.1494 3.795	0.1490 3.785	0.1490 3.785	0.1490 3.785	0.1500 3.810
Depth (in) (mm)	0.1260 3.200	0.1255 3.188	0.1260 3.200	0.1250 3.175	0.1250 3.175	0.1250 3.175	0.1230 3.124
Composition: %W %Ni %Fe	94.0 4.3 1.7						
Consolidation	Ceracon						
Measured Density (g/cm ³)	17.95	17.95	17.95	17.51	17.80	17.95	17.95
Theoretical Density (g/cm ³)	17.95	17.95	17.95	17.95	17.95	17.95	17.95
Percent Dense	100.0	100.0	100.0	97.5	99.2	100.0	100.0
Deflection (in) (mm)	0.024 0.610	0.018 0.457	0.020 0.508	0.010 0.254	0.013 0.330	0.016 0.406	0.024 0.610
Maximum Load (lbf) (N)	889 3954	801 3583	785 1492	887 2987	810 3603	949 4221	823 3661
Ultimate Stress (ksi) (MPa)	318 2193	288 1986	279 1924	242 1669	294 2027	344 2372	306 2110

Table I. Flexural test results for coated powder consolidated by Ceracon.

DEFORMATION AND FAILURE BEHAVIOR OF 93W-5Ni-2Fe AT DIFFERENT SHEAR STRAIN RATE LOADING

Tusit Weerasooriya and Patricia A. Beaulieu

Materials Dynamic Branch
Army Research Laboratory
Watertown, MA 02172

ABSTRACT

A tungsten heavy alloy containing 93% W (Teledyne 93W-5Ni-2Fe alloy swaged to 17%) was tested in torsion from quasi-static to high strain rates of loading. High strain rate tests were conducted using a Torsional Split Hopkinson Bar apparatus. The results from these tests show that the yield and failure strengths of this alloy increase with increasing strain rate. The strain to failure decreases with increasing strain rate. At a strain rate of 600 s^{-1} , flow stress decreases with increasing strain, indicating thermal softening dominating over both strain and strain rate hardening of the material at high strain rate of deformation. The instability that leads to the initiation of failure at high rates is due to the formation of a localized shear band. The width of the intense shear zone of deformation decreases with increasing shear strain rate reaching a limiting width of one to two grains at high strain rates. As the shear strain rate is increased, there is a reduction in the number of cleavage and brittle grain boundary fracture zones. The results under dynamic conditions show that the 93% W alloy deforms and fails quite differently compared to that under slow rates of shear loading.

INTRODUCTION

Tungsten heavy alloys are used in many applications for their mechanical and physical properties such as high density, high strength, good ductility, and good corrosion resistance.¹⁻³ Tungsten heavy alloys such as 93W-5Ni-2Fe are of interest to the Army as kinetic energy penetrators (as a replacement for depleted uranium) for defeating armor, because of the high density and excellent mechanical properties. Usually, these mechanical properties are obtained at slow loading rates. Since these alloys are going to be used under dynamic loading conditions by the Army, it is essential to evaluate their mechanical properties and failure behavior under high strain rate loading conditions. Unfortunately, there is very little mechanical property and failure behavior data available for these alloys under dynamic loading conditions.⁴⁻⁶ Almost all of this available data in the literature have been obtained under uniaxial compressive loading conditions.

There is almost no information available under high shear rate loading conditions for tungsten heavy alloys (WHA). Therefore, this work was undertaken at the Materials Directorate at the Army Research Laboratory (ARL) to study and understand the differences in the deformation/failure behavior of a standard penetrator tungsten heavy alloy (93W-5Ni-2Fe) under quasi-static to high strain rate shear loading conditions. This material was chosen to be used as the base line (reference) material for future studies on other WH alloys. In this study, information on how the failure process interacts with the microstructure were obtained for different shear loading rates.

EXPERIMENTS

Material

The 93%W alloy that was used for the experiments in this report was obtained from Teledyne. Chemical composition and some of the mechanical properties of this alloy from the manufacturer are:

W	92.85%
Ni	4.9%
Fe	2.25%

Density = 17.69 - 17.76 g/cc
Hardness = HRC 39-40
UTS = 1103 MPa (160,000 psi)
Elongation = 13%

This alloy was processed by Teledyne using the following procedure. A mixture of W, Ni, and Fe powder was isostatically pressed to 207 MPa (30,000 psi) in a Drybag press. Pressed material was then sintered in a hydrogen atmosphere in a molybdenum furnace at about 1520°C. The hydrogen atmosphere was used to reduce powder surface oxides. The sintered material was vacuum annealed at about 1000°C for 10 hours to remove the absorbed hydrogen. The annealed material was heated in an inert gas atmosphere to about 1100°C and soaked for about an hour. It was then water quenched to give better dynamic impact properties. The bars were then machined and swaged to 17%.

Figure 1 shows the microstructure of this alloy taken in the longitudinal direction. Microstructure in the transverse direction is similar to the one in the longitudinal direction. Swaging to 17% does not seem to affect the microstructure of the alloy. As shown in the figure, microstructure consists of two phases: nearly pure W spherical grains of bcc crystal structure and W-Ni-Fe matrix of fcc crystal structure. Matrix material provides the ductility for the W alloy with these brittle W grains. The size of W grains are approximately 27 μm and are mostly surrounded by a thin layer of matrix material. However, some of W grains are in contact with the adjacent W grains.

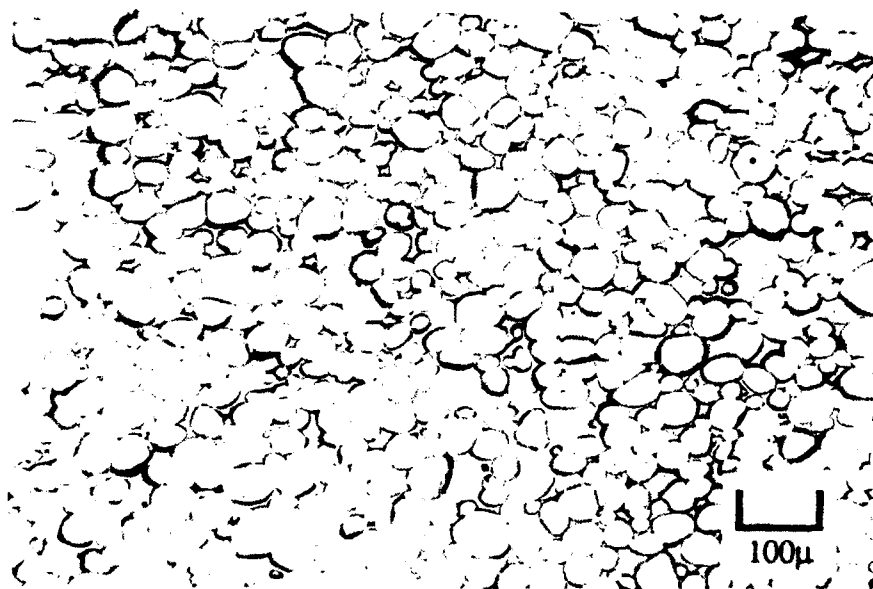


Figure 1. Microstructure of 93W-5Ni-2Fe Tungsten Heavy Alloy swaged to 17%.

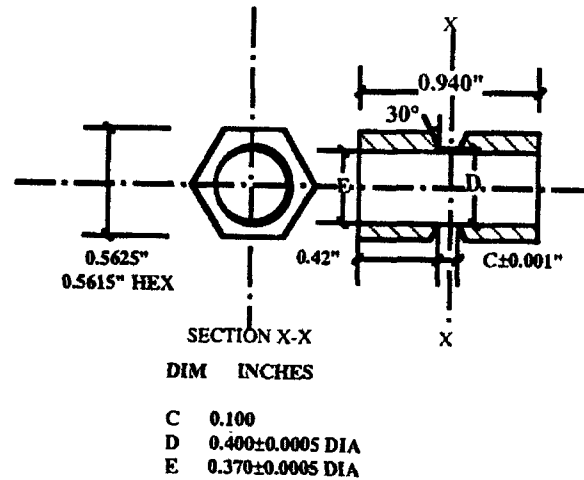


Figure 2. Specimen geometry.

Specimen Geometry

Geometry of the test specimen is shown in Figure 2. The gage section of the test specimen is a thin wall tube (0.38 mm wall thickness) of 0.254 mm gage length and outside and inside diameters of 10.16 and 9.40 mm, respectively. The wall thickness corresponds to an average of 14 W grains. Hexagonal flanges with 60° shoulders are machined at both ends of the thin tubular gage section, which are used to attach the specimen to the elastic input and output bars of the test system. Before testing the specimens, a fine line is scribed parallel to the axis of the specimen on the inside wall of the specimen to obtain approximate strain of the specimen after the testing.

In this short gage length specimen, an almost homogeneous state of strain is achieved after a few reflections of the loading shear stress pulse. In a specimen with a similar gage area, but end flanges with sharper (90°) shoulders, the plastic zone starts at the flange-gage section interface. Although the plastic zone starts at this interface, it is contained until it spreads gradually through the specimen and engulfs the whole gage section.⁷

Torsional Experiments

High Rate Tests

High rate tests described in this report were conducted using a torsional Split-Hopkinson Bar. Our torsional Hopkinson bar is described by Weerasooriya⁸ in detail. It consists of two bars of diameter 25.4 mm and made of 7075-T6 aluminum. The hexagonal flanged thin wall specimen is attached between the two bars. A torque is stored between the non-specimen end of the input bar and the clamp. High strain rate of loading is applied to the specimen by the sudden release of the stored-torque by breaking the clamp. The position of the clamp determines the duration of the stress pulse. This incident torsional stress pulse travels towards the specimen after its release; at the specimen, part of the pulse transmits through the specimen to the output bar and the remainder reflects back to the input bar. From the incident, reflected and transmitted pulses that are obtained from the strain gages mounted on the input and output bars, the stress, strain and strain-rate can be inferred as a function of time. More details of the apparatus, data acquisition and reduction procedure is given by Weerasooriya.¹¹ When the shear bands initiate, the above strain and strain-rate represent average values in the gage section.

Slow Rate Tests

Slow rate tests were also conducted using the torsional Hopkinson bar set-up which was modified for this purpose. A servomotor with a reducer (3600:1) was attached to the non-specimen end of the output bar. During slow rate testing, the input bar was held stationary using the clamp of

the torsional Split-Hopkinson bar. Linear Variable Differential Transformers (LVDTs) were attached to both input and output bars. Relative rotational displacement between the ends of the gage area was measured using these LVDTs during the slow rate testing. Engineering shear strain of the specimen was calculated using the relative angular displacement. Shear stress was calculated using the thin wall tube assumption for the gage section of the specimen.

After testing all the specimens were examined with optical and scanning electron microscopes.

RESULTS AND DISCUSSION

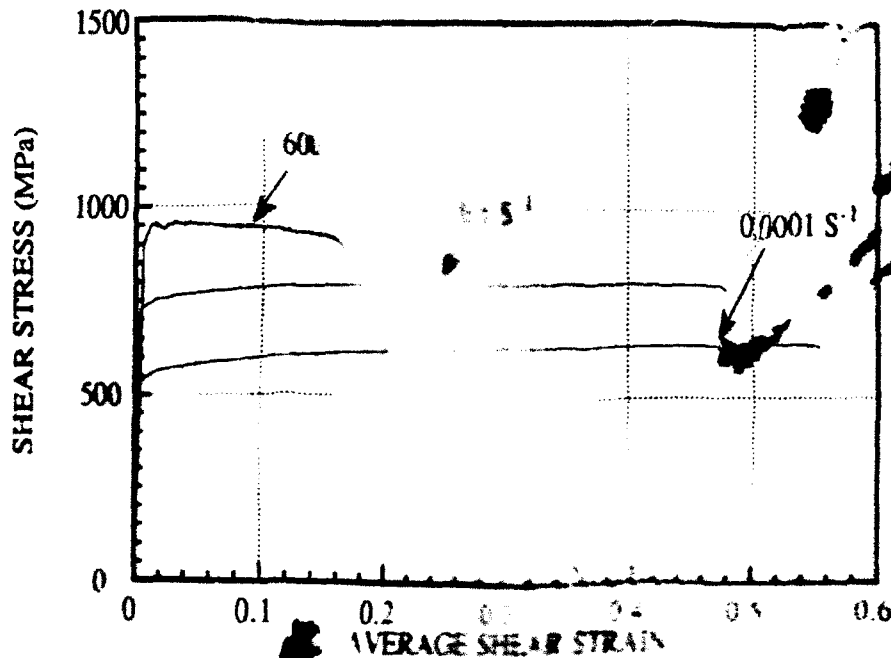


Figure 3. Shear stress-strain for 93% W alloy at different strain rates.

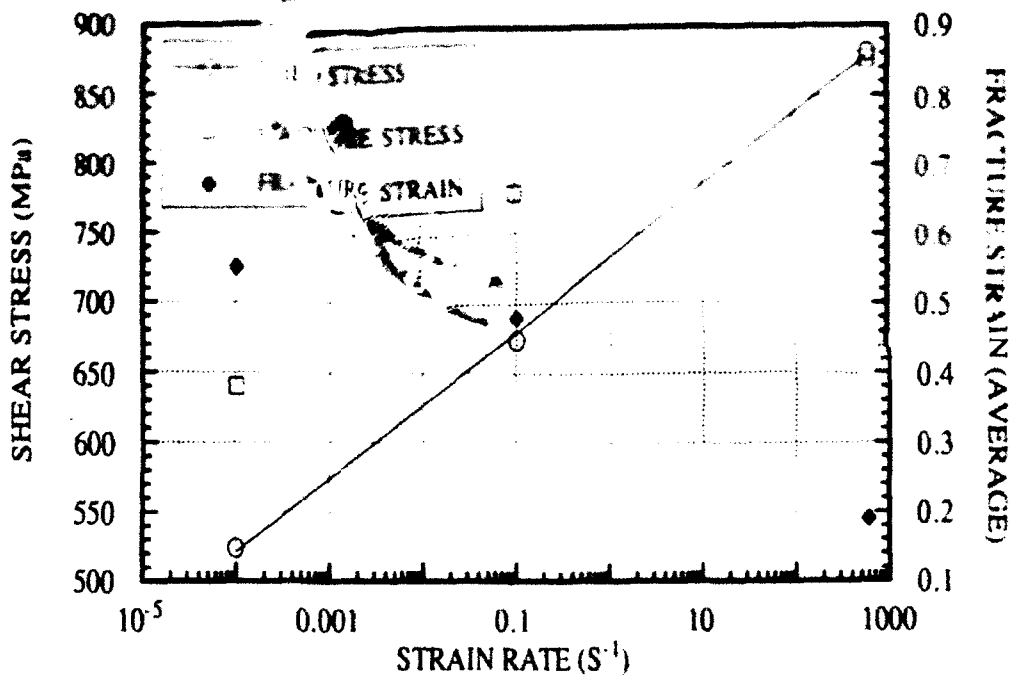


Figure 4. Yield stress, fracture stress and fracture strain as a function of strain rate for 93% W alloy.

Shear stress versus engineering shear strain results for the three different strain rates (0.0001, 0.1, and 600 s⁻¹) are given in Figure 3.

Shear stress - shear strain behavior is strain rate sensitive for this material. Figures 4 shows yield stress and failure strength as a function of logarithmic strain rate, respectively, from the constant strain rate tests. These plots show that both yield and failure strengths increase with strain rate. From the observed linear behavior between the yield stress and the logarithmic value of shear strain rate in Figure 4, the following relationship can be obtained relating the shear strain rate ($\dot{\gamma}$) to the yield stress (τ_y):

$$\tau_y = 23 \log_e(\dot{\gamma}) + 732$$

where τ_y is given in MPa and $\dot{\gamma}$ is given in s⁻¹. Total shear strain to failure is plotted as function of logarithmic strain rate in Figure 4. As shown in this figure, total shear strain to failure decreases with increasing strain rate.

For slow strain rates (0.0001 and 0.1 s⁻¹), flow stress increases with increasing shear strain (work hardening). In contrast, at high strain rate of 600 s⁻¹, flow stress decreases with increasing shear strain (softening). This indicates that the thermal softening is dominating over strain hardening and strain-rate hardening during deformation at high strain rates. The difference in deformation at high strain rate is due to adiabatic heating of the material. Strain to failure at strain rates of 0.0001 and 0.1 s⁻¹ are approximately 55% and 48%, respectively. Strain to failure at 600 s⁻¹ strain rate is approximately 19%.

Figures 5a-b show the micrographs taken in the vicinity of the fracture surface of the failed specimens at strain rates of 0.0001 and 0.1 s⁻¹, respectively. Closer to the fracture surface, originally spherical W grains have deformed to ellipsoidal shapes. The band of this intense shear zone containing elliptical W grains is approximately 2.14 mm (here the band is defined as two times the width of the zone in the figure) wide for 0.0001 s⁻¹ rate and 1.4 mm wide for 0.1 s⁻¹. These ellipses have aligned their major and minor axes 45° to the shear direction. The directions of the major and minor axes correspond to the directions of maximum tensile and minimum compressive principal stresses, respectively. Fracture path is mostly of intergranular, but if a large W grain is blocking the path, fracture will go through the grain splitting the W grain by the cleavage mechanism. This can be seen more clearly in the scanning electron micrographs of the fracture surfaces given in Figures 6a-b. Intergranular and cleavage facets can clearly be observed. Fracture surface from 0.0001 s⁻¹ strain rate test shows dimples, typical of ductile fracture, after initial intergranular separation. This indicates that the cavities formed along the grain boundaries coalesce together by the ductile mechanism of fracture of the matrix material separating them. However, the areas showing this typical ductile failure decreases with increasing strain rate.

Figure 5c shows the microstructure at the vicinity of the fracture surface of a failed specimen which was tested at the strain rate of 600 s⁻¹. In this case, in the layer of W grains adjacent to the fracture surface, highly deformed W grains which are of elliptic shape with their major axes aligned 45° to global shear direction can be observed. In contrast to the slower strain rates, here the width of the intense shear zone is much smaller - shear localization (width of two grains). Figure 6c shows a typical fracture surface of a failed specimen after it has undergone deformation at high rate. Grain boundary facets can be observed as for lower rate tests. Cleavage and ductile dimple-like failure are not present as seen in lower rate tests. Most of the fracture surface is covered with smooth facets. These areas may correspond to W grains that have flowed like a fluid (extruded) during final deformation just before the failure. It is not possible to fully explain these areas without any further analysis of the material in these locations.

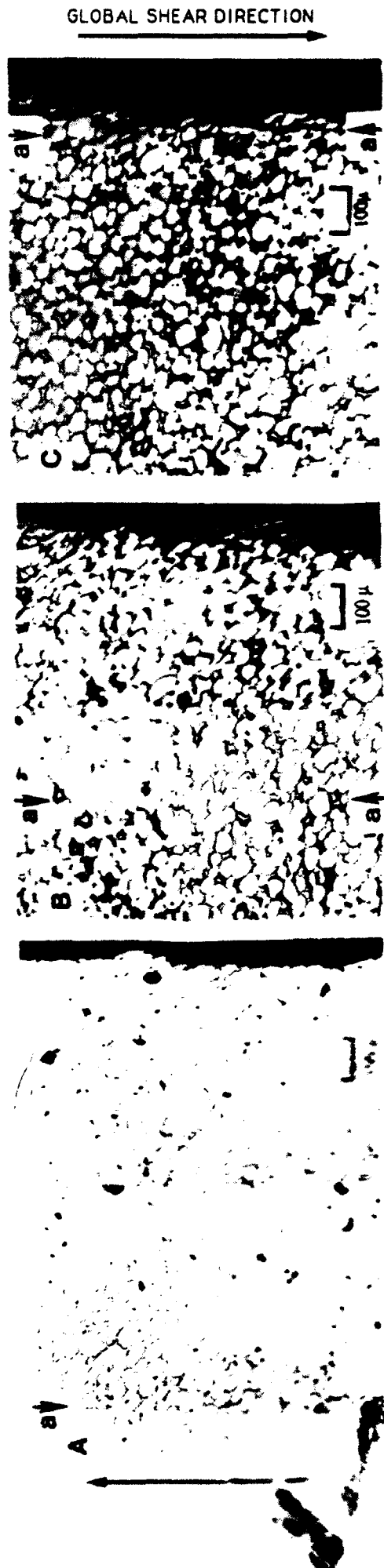


Figure 5. The details at the vicinity of fracture in failed specimens. Line a-a approximately represents the end of the intensely deformed region. The tests were conducted at room temperature at a shear strain rate of a). 0.0001 s^{-1} and failed at a global shear strain of 55% b). 0.1 s^{-1} and failed at a global shear strain of 48% and c). 600 s^{-1} and failed at a global shear strain of 19%.



Figure 6. Typical fracture surfaces of failed specimens strained at a rate of a). 0.0001 s^{-1} , b). 0.1 s^{-1} and c). at 600 s^{-1}

SUMMARY AND CONCLUSIONS

Torsional tests were conducted to study the deformation and failure behavior of 93W-5Ni-2Fe alloy at different strain rates. Tests were conducted at low to high shear strain rates: 0.0001, 0.1 and 600 s⁻¹. High rate tests (600 s⁻¹) were conducted using a Torsional Split Hopkinson Bar apparatus. After testing, all the specimens were analyzed using optical and scanning electron microscopes.

From these constant strain rate test results, yield and failure strengths increased with increasing strain rate; failure strain decreased with increasing strain rate. At 600 s⁻¹ shear strain rate, flow stress decreased with strain, thus indicating thermal softening dominating over strain and strain-rate hardening of the material at high strain rates. The failure at high rate was due to the instability from the formation of a shear band. Results indicated that the high strain rates promoted the formation of shear bands. The width of the intense shear zone of deformation decreased with increasing shear strain rate reaching a limiting width of two grains (localized) at high strain rates. Therefore, the width the shear band is controlled by microstructure of the W alloy. As the shear strain rate is increased, there was a reduction in the number of cleavage and brittle grain boundary fracture zones. The results under dynamic conditions showed that the 93% W alloy deformed and failed quite differently compared to that under slow rate of loading. Thus, the materials that are used under dynamic loading conditions should be evaluated under high rate loading conditions.

Expanded version of this paper with a detailed study of the mechanism of formation of the shear band and its interaction with the microstructure has been submitted to the journal of Material Science and Engineering.⁹

ACKNOWLEDGMENT

We are grateful for Ronald Swanson of MTL for all the help provided during the course of the work described in this report.

REFERENCES

1. L.M. Ekbom, "Tungsten Heavy Metals", Scand. J. of Metall., v. 20, 1991, p. 190-197.
2. A. Bose and R.M. German, "Sintering Atmosphere Effects on Tensile Properties of Heavy Alloys", Met. Trans. A, 19A, 1988, p. 2467-2476.
3. R.J. Dowding, "Tungsten Heavy Alloys: A Tutorial Review", 1991, P/M in Aerospace and Defence Technologies, MPIE, Princeton, NJ, 1991, p. 109-116.
4. L.W. Meyer, H. D. Kunze and E. Staskewitsch, "Dynamic Strength and Ductility of a Tungsten Alloy for KF Penetrators in Swaged and Unswaged Condition Under Various Loading", The Proc. of the 7th International Symposium on Ballistics, The Hague, 1983, p. 289-293.
5. R. Tham and V. Stilp, "Yield Strength and Flow Stress Measurements of Tungsten Sinter Alloys at Very High Strain Rates", Journal De Physique, Tome 49, No. 9, C3-85, 1988.
6. B.P. Zhang, L. Zheng, Q.Y. Peng and Y.M. Xiong, "Dynamic Behavior of Tungsten Sintered Alloys at High Strain Rates up to 10⁵ s⁻¹", to be published.
7. E.K.C. Lee, "An Elastic-Plastic Stress Analysis of the Specimen Used in the Torsional Kolsky Bar", J. Appl. Mech., v. 47, 1980, p. 278.
8. Tusit Weerasooriya, "The MTL Torsional Split-Hopkinson Bar", U. S. Army Materials Technology Laboratory, MTL TR 90-27, 1990.
9. Tusit Weerasooriya and Patricia A. Beaulieu, "Effects of Strain Rate on the Deformation and Failure Behavior of 93W-5Ni-2Fe Under Shear Loading", submitted to Mat. Science and Eng. A.

PERFORMANCE-PROPERTY RELATIONSHIPS IN TUNGSTEN ALLOY PENETRATORS

**Patrick Woolsey, Robert J. Dowding, Kenneth J. Tauer,
and Frank S. Hodi**

**Materials Directorate
U.S. Army Research Laboratory
Watertown, MA 02172-0001**

ABSTRACT

The physical, mechanical, and microstructural features of six lots of commercially produced tungsten heavy alloy penetrators, having compositions in the range from 91% to 97% W and a broad range of quasi-static properties, were determined. Ballistic performance data were obtained for penetrators fabricated from each of these alloys using the residual penetration test method. This technique determines performance on the basis of penetration depth in a semi-infinite rolled homogeneous armor (RHA) steel block. When the results of the ballistic tests were correlated with the measured physical and mechanical properties, and other metallurgical aspects, it was concluded that mechanical properties have no significant influence on the penetration mechanism exhibited by tungsten heavy alloy rods.

INTRODUCTION

Development of tungsten heavy alloys (WHA) for use in long rod kinetic energy (KE) penetrators has drawn considerable attention over the past several years. With the presently increased emphasis on environmental considerations, it is becoming even more desirable to find a reasonable substitute for the widely used depleted uranium (DU) alloys used for many current penetrators. The basic question which remains to be addressed is thus one of determining the most favorable substitute material. Although tungsten heavy alloys have been widely employed in the fabrication of advanced KE penetrators both in model-scale and full-scale, they have not yet matched the depleted uranium in ballistic performance. Several series of model-scale tests have been conducted at the U.S. Army Research Laboratory's Materials Directorate (ARL-MD), employing WHA materials with a wide range of mechanical properties, in order to determine if recent improvements in alloy design have affected the terminal ballistic performance of these materials.

Long rod penetrators are eroding projectiles. They penetrate targets by a quasi-hydrodynamic process, wherein the stresses imposed upon both penetrator and target materials are significantly greater than their yield strengths. Yielded penetrator material is essentially extruded backward, in conjunction with failed target material. The classic analysis of this system for a 1-dimensional case has been done by Tate¹; a thorough review and discussion of the models commonly employed for this type of penetration has been given by Anderson et al.² However, these models do not fully account for the differences in

performance between penetrator materials encountered from empirical results. The behavior of the penetrator materials in particular is not fully understood at the stress levels and strain rates prevalent during a ballistic event. Magness³ has advanced a model which explains penetration performance upon the adiabatic shear susceptibility of a penetrator material. His paper compared a number of tungsten and DU alloys, with the metric for penetration efficiency being ballistic limit velocity. In a ballistic limit test, the striking velocity of the projectile is varied from no perforation to complete perforation of the armor plate. This allows effects related to the failure of the rear surface of the target to influence the event. An earlier study performed at ARL-MD with several WHA penetrators⁴ used a semi-infinite target, which approximately negates the influence of rear surface effects upon the penetration event. Thus, one might expect some additional differentiation between materials on the basis of only thick target penetration capability in such a configuration. Comparisons of these results with Magness' model showed, however, that for the WHA materials studied, the model appeared to be valid.

The alloys tested previously were of moderate strength levels and low toughness, and had Ni-Fe or Ni-Fe-Co matrixes. The current availability of alloys with improved mechanical properties prompted an expansion of the test program to include representatives of these materials in order to determine whether the original conclusions remain valid.

PENETRATOR MATERIALS

The penetrator materials selected for this study are detailed in Table 1, along with their nominal compositions. Materials having a designation of X-27 or X-21 are commercial products obtained from Teledyne Firth Stirling. The W-2 alloy is a product of Kennametal. The number in parentheses following the alloy designation indicates the year in which the penetrators were purchased. Alloys selected tend to be in the range of 91% to 93% tungsten. This is mainly due to the improved toughness and ductility of such alloys over those with a higher tungsten content, although they do suffer a reduction in density compared to high tungsten content alloys such as W-2. The X-27X materials have a Ni-Co matrix, which represents an attempt to improve upon the standard Ni-Fe-(Co) system.

Table 1. Nominal Chemical Compositions (in weight %)

Penetrator Material	Tungsten	Nickel	Iron	Cobalt	Copper
X-27R (1983)	91	6.3	2.7	-	-
X-27C (1989)	91	4.5	2	2.5	-
X-27C (1991)	91	4.5	2	2.5	-
X-27X (1991)	91	6.0	-	3.0	-
X-21C (1989)	93	3.5	1.5	2.0	-
W-2 (1983)	97.1	1.6	0.7	0.1	0.5

Mechanical properties of these alloys are shown in Table 2. All of the WHA materials employed were swaged, most commonly by 15-20%. The two types of X-27X (#1 and #2) identified below are representative of different levels of swaging and heat-treatment of the base alloy in order to obtain different strength levels. For comparison, properties for the standard DU-3/4% Ti composition are also given (from Magness³). All values shown for the WHA materials were determined from tests performed at ARL-MD, with the exception of the impact energy values, which were obtained from Teledyne data. Impact tests were performed with an unnotched Charpy specimen geometry.

Several of the materials employed in these tests did exhibit significant improvements in static properties over previous alloys. The X-27C (1991) penetrators have about 9% greater strength than the 1989 batch and roughly similar ductility. The X-27X #2 has about 23% greater strength than the X-27C (1989), and is quite close to the DU alloy. Both X-27X materials exhibit significantly improved toughness. Macrohardnesses of these penetrators do not vary significantly, since these particular alloys

were all cold-worked by swaging. The elongation and reduction of area values for all the 91% tungsten alloys are good; even the high strength X-27X has about 9% elongation. The decrease in R.A. for the X-21C and the more dramatic reduction for the W-2 are functions of the reduced matrix volume in these materials.

Table 2. Mechanical Properties

Material	0.2% Yield (ksi) (MPa)	UTS (ksi) (GPa)	Hardness (HRC)	R.A. (%)	Elongation (%)	Impact (J)
X-27R (1983)	171.0 (1172)	174.0 (1200)	37.1	20.4	—	135
X-27C (1989)	169.4 (1168)	171.0 (1179)	38.6	16.8	11.9	244
X-27C (1991)	184.9 (1275)	186.4 (1285)	—	23.8	9.4	160
X-27X#1 (1991)	191.1 (1318)	199.1 (1373)	—	21.1	11.6	300
X-27X#2 (1991)	206.2 (1422)	209.9 (1447)	—	20.5	8.9	300
X-21C (1989)	187.9 (1296)	193.2 (1332)	39.4	10.4	10.8	143
W-2 (1983)	149.2 (1029)	150.3 (1036)	37.6	1.8	3.1	—
DU-3/4Ti	122.9 (848)	215.9 (1489)	40	—	24.0	—

Representative microstructures of X-27C, X-27X, X-21C, and W-2 are shown in Figures 1-4 respectively. Grain size of the X-27C is about 16 μm , with the X-27X around 30 μm , the X-21C at 25 μm , and the W-2 above 80 μm . An interesting feature evidenced in the X-27X material is the existence of numerous fine acicular precipitates within the matrix. EDX analysis indicates that these are mostly tungsten.

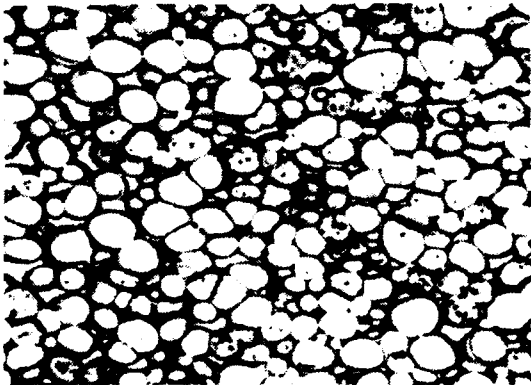


Figure 1. X-27C Alloy (Optical) 50 μm

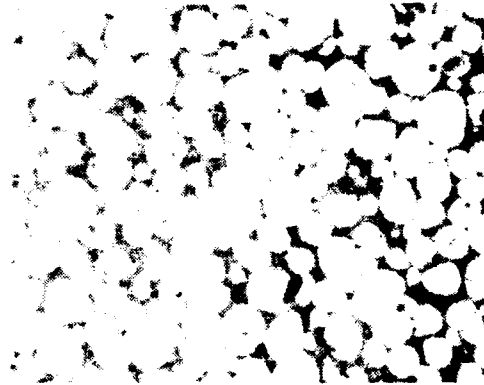


Figure 2. X-27X Alloy (Optical) 50 μm

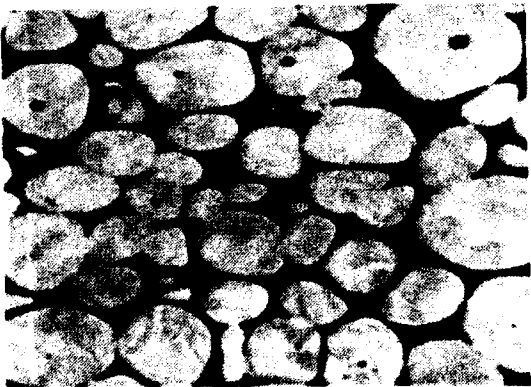


Figure 3. X-21C Alloy (BEI) 50 μm

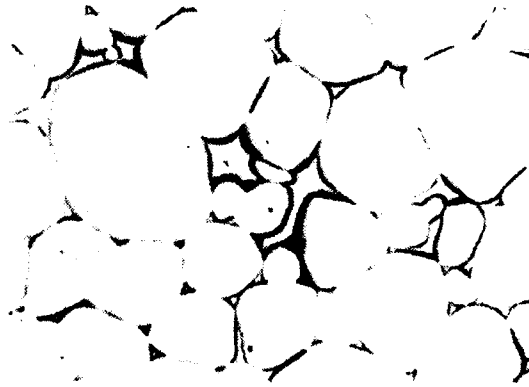


Figure 4. W-2 Alloy (Optical) 50 μm

BALLISTIC TESTING PROCEDURES

All tests were conducted at ARL-MD using a 20mm smoothbore powder gun. Projectile launch packages were base-push sabots using a steel pusher disc. The penetrators were cylindrical rods with hemispherical noses, having aspect ratios (L/D) of 10:1, and masses of 65 g. Exact penetrator dimensions were allowed to vary so as to maintain constant mass for alloys of different densities. A summary of dimensions and densities is given in Table 3 below. The values for DU penetrators are due to Magness³. Densities were obtained by Archimedes' method unless otherwise marked (indicating calculation from a dimensionally determined volume).

Table 3. Penetrator Dimensions and Masses

Material	Length	Diameter	Mass (g)	Density(g/cc)
X-27R (1983)	3.100	0.310	65	17.45
X-27C (1989)	3.100	0.3099	65.4	17.35
X-27C (1991)	3.125	0.308	65.1	17.33*
X-27X #1 (1991)	3.098	0.3079	65	17.45*
X-27X #2 (1991)	3.098	0.3081	65	17.45*
X-21C (1989)	3.070	0.3070	64.9	17.73*
W-2 (1983)	3.03	0.303	65	18.63
DU-3/4Ti	3.03	0.303	65	18.6

* Dimensional density

Projectile velocity and yaw were measured by means of an orthogonal flash X-ray system. Striking velocities were varied over a range from about 2500 fps (760 m/s) to about 5700 fps (1735 m/s) for the baseline data. Comparative tests made for this study were kept within the above range, and were generally made in the 4000 to 5000 fps (1220-1520 m/s) region. The criterion for acceptance and inclusion of a test point was a total projectile yaw of less than 3 degrees; previous studies at ARL-MD and the ARL-WTD have indicated this as an appropriate cutoff limit.

The target employed in all instances was a monolithic plate of RHA (rolled homogeneous armor) steel (MIL-A-12560, Class 3), with thickness selected to ensure that the plate thickness remained semi-infinite with respect to the penetration (meaning 4 inch or 5 inch (101 or 127 mm) thick plates were used in most cases). Plate surfaces were held at 0° obliquity (i.e., normal to the line of flight). The average hardness of the RHA plates was HRC 27. Depths of penetration into the plate were obtained by direct measurement of cross-sections, which were prepared by bandsaw cutting through the center of the penetration cavity.

RESULTS

Comparisons of the penetration efficiency of different penetrator materials may be made by plotting the depth of penetration into the steel as a function of projectile striking velocity. Previous results had determined the X-27R and X-27C (1989) to be identical in their penetration performance. Thus, these data form the baseline against which the other materials may be compared. Figure 5 shows a plot of the baseline tungsten data, together with a linear regression fit which may be used to obtain the penetration at any desired velocity. The standard deviation for the depth of penetration is 0.05 in over the tested velocity range. Figure 6 gives a comparison of the baseline tungsten with the standard DU alloy⁵. The performance advantage of the DU is evident from this.

Figure 7 shows the X-27C (1991) and X-21C (1989) compared with the line of fit for the baseline material. These exhibit no significant difference in performance, despite improved mechanical

properties. Figures 8 and 9 show the X-27X #1 and #2 alloys. Again, the average level of performance has not changed. There is some indication that for these materials, there may be a slight gain in penetration performance at the higher end of the velocity regime. Such behavior might be attributed to a slightly earlier shift from eroding to rigid body penetration near the end of the penetration process, based on the higher yield strength of these materials as compared to the baseline materials. In any event, even if this effect is manifested, it does not significantly raise the general level of performance. Finally, the W-2 alloy is compared with the baseline alloy in Figure 10. In this case only, there is a slight general improvement in penetration, which we attribute to the increased density. Again, its performance is not equal to the DU penetrator.

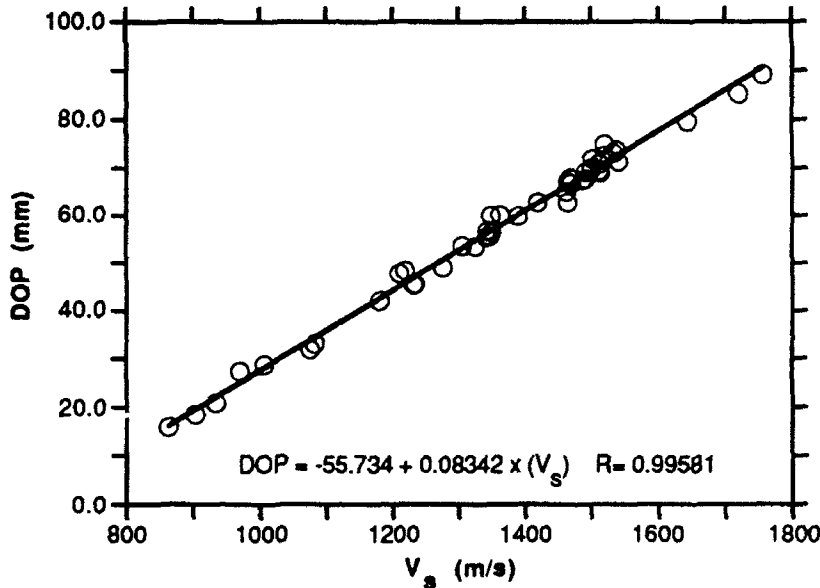


Figure 5. WHA Baseline (X-27R and X-27C (1989) Penetrators)

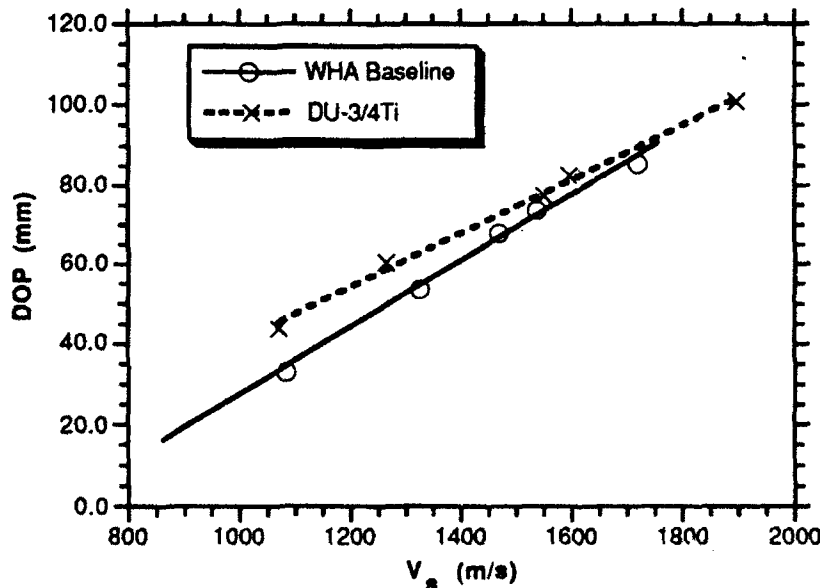


Figure 6. WHA and DU Performance Comparison

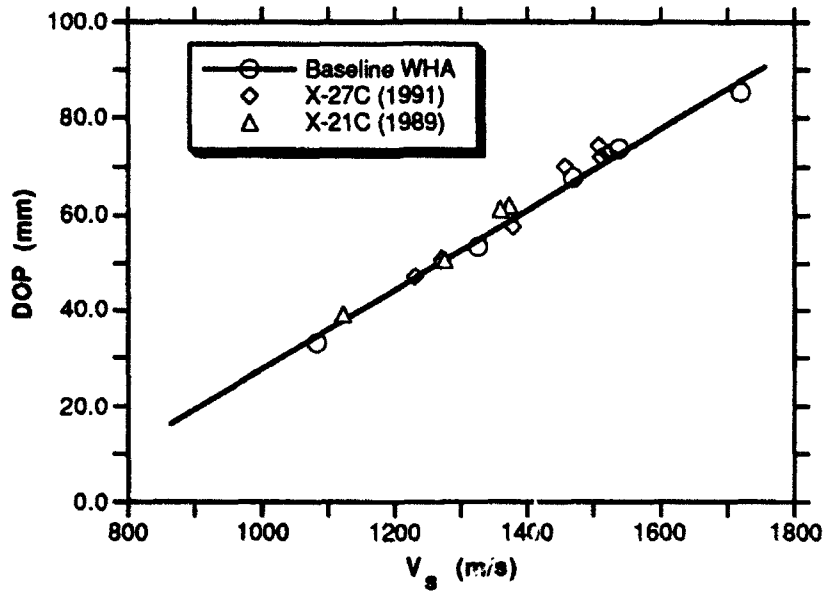


Figure 7. X-27C (1991) and X-21C Performance

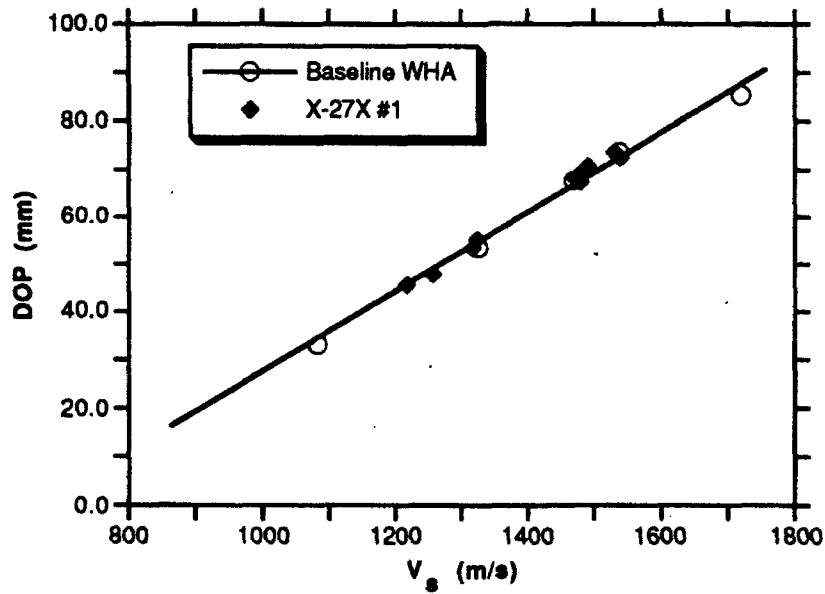


Figure 8. X-27X#1 Alloy Performance

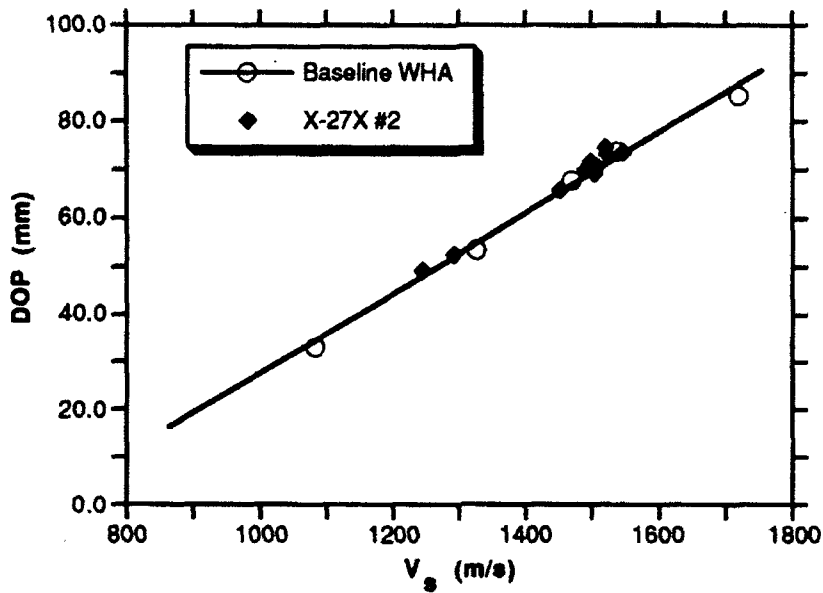


Figure 9. X-27X#2 Alloy Performance

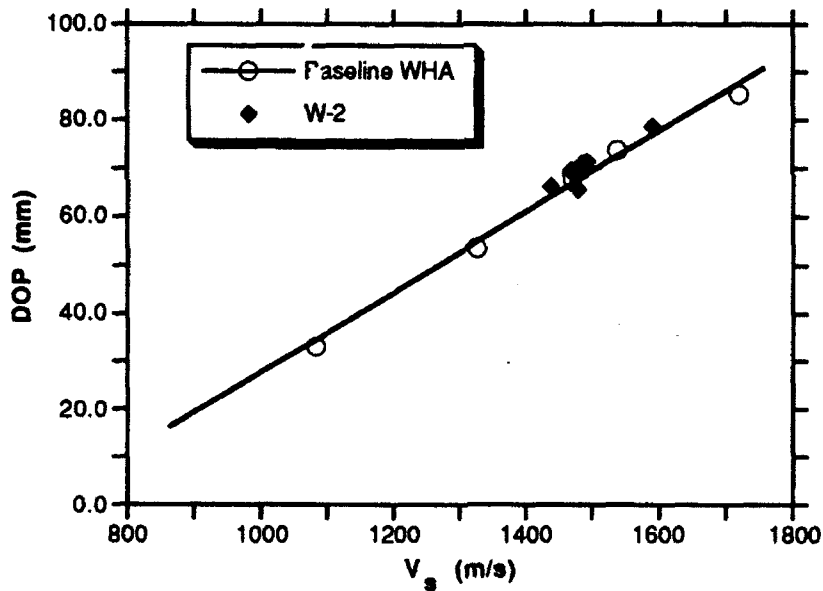


Figure 10. W-2 Alloy Performance

CONCLUSIONS

The behavior of all WHA materials over the tested velocity range is linear, and is at best marginally influenced by large strength variations. Only the W-2 rods exhibit an average level which is greater than the inherent scatter in the test results. These results confirm our earlier finding that only density is a significant driver of performance for traditional WHA materials in thick target penetration, as well as supporting the conclusions of Magness. This means that it will not be possible to provide a WHA penetrator with performance equivalent to a DU rod by simply improving its static mechanical properties. It does not imply that mechanical properties have no influence at all on performance, since

in finite plate targets which impart significant bending moments on the rods, it is possible to observe larger performance variations between WHA materials. However, this does mean that in order to bring tungsten into parity with DU, some other means of improvement, such as a new matrix material or tailored-failure structure providing an effect akin to adiabatic shear, must be found.

ACKNOWLEDGMENTS

The authors would like to thank Dr. Lee Magness for his technical contributions, Mr. Philip Wong for providing EDX analysis of the specimens, and Mr. Eugenio DeLuca for his support of this project. They also appreciate the valuable assistance of Messrs. John Segalla, John Loughlin, Robert Muller, and Raul Dominguez in performing the ballistic testing, and George Dewing and Robert Grossi in sample preparation.

REFERENCES

1. A. Tate, "A Theory for the Deceleration of Long Rods After Impact," *J. Mech. Phy. Solids* 15, 387 (1967).
2. C. E. Anderson, Jr. and J. D. Walker, "An Examination of Long Rod Penetration," *Int. J. of Impact Eng.*, 4, 481-501 (1991).
3. L.S. Magness and T.G. Farrand (1990), "Deformation Behavior and its Relationship to the Penetration Performance of High-Density KE Penetrator Materials," *1990 Army Science Conference*, Durham, NC.
4. R.J. Dowding, K.J. Tauer, F.S. Hodi, and P. Woolsey, "Metallurgical and Ballistic Characterization of Quarter-Scale Tungsten Alloy Penetrators," USAMTL TR 90-31, April 1990.
5. L.S. Magness and W.J. Perciballi, U.S. Army BRL (now ARL-WTD), private communications, September 1990.

DISTRIBUTION LIST

No. of Copies	To
1	Office of the Under Secretary of Defense for Research and Engineering, The Pentagon, Washington, DC 20301
	Director, U.S. Army Research Laboratory, 2800 Powder Mill Road, Adelphi, MD 20783-1197
1	ATTN: AMSRL-OP-CI-A
1	Dr. Alan Goldman
	Commander, Defense Technical Information Center, Cameron Station, Building 5, 5010 Duke Street, Alexandria, VA 22304-6145
1	ATTN: DTIC-FDAC
1	MIAC/CINDAS, Purdue University, 2595 Yeager Road, West Lafayette, IN 47905
	Commander, Army Research Office, P.O. Box 12211, Research Triangle Park, NC 27709-2211
1	ATTN: Information Processing Office
1	Dr. Andrew Crowson
1	Dr. Edward Chen
	Commander, U.S. Army Materiel Command, 5001 Eisenhower Avenue, Alexandria, VA 22333
1	ATTN: AMCSCI
	Commander, U.S. Army Materiel Systems Analysis Activity, Aberdeen Proving Ground, MD 21005
1	ATTN: AMXSU-MP, Director
	Commander, U.S. Army Missile Command, Redstone Arsenal, AL 35809
1	ATTN: AMSMI-RD-CS-R/Doc
	Commander, U.S. Army Armament Research Development and Engineering Center, Dover, NJ 07801
1	ATTN: Technical Library
1	Mr. D. Kapoor
1	Dr. S. Cytron
	Commander, U.S. Army Tank-Automotive Command, Warren, MI 48397-5000
2	ATTN: AMSTA-TSL Technical Library
	Commander, U.S. Army Foreign Science and Technology Center, 220 7th Street, N.E. Charlottesville, VA 22901
3	ATTN: AIFRTC, Applied Technologies Branch, Gerald Schlesinger
	Naval Research Laboratory, Washington, D.C. 20375
1	ATTN: Code 5830
1	Code 2627
1	Dr. Virgil Provenzano
	Chief of Naval Research, Arlington, VA 22217
1	ATTN: Code 471
	Naval Surface Weapons Center, Dahlgren Laboratory, Dahlgren, VA 22448
1	ATTN: Code G-32, Ammunition Branch, Mr. Brian Sabourin
	Commander, Rock Island Arsenal, Rock Island, IL 61299-6000
1	ATTN: SMCRI-SEM-T
	Battelle Columbus Laboratories, Battelle Memorial Institute, 505 King Avenue, Columbus, OH 43201
1	ATTN: Mr. Henry Cialone
1	Dr. Alan Clauer
	Battelle Pacific Northwest Laboratories, P.O. Box 999, Richland, WA 99352
1	ATTN: Mr. William Gurwell
1	Dr. Gordon Dudder
1	Mr. Curt Lavender
	GTE Sylvania, Inc. Chemical and Metallurgical Division, Hawes Street, Towanda, PA 18848
1	ATTN: Dr. James Mullendore
1	Mr. James Spencer
1	Ms. Susan Doepker

No. of Copies	To
1	Director, Ballistic Research Laboratory, Aberdeen Proving Ground, MD 21005
1	ATTN: SLCBR-TSB-S (STINFO)
1	SLCBR-TB-P, Mr. Lee Magness
1	Ms. W. A. Leonard
1	Teledyne, 47th Sterling, 1 Teledyne Place, LaVergne, TN 37086
1	ATTN: Dr. Steven Caldwell
1	Los Alamos National Laboratory, ATAC, MS F681, P.O. Box 1663, Los Alamos, NM 87545
1	ATTN: Mr. Bill Hogan
1	Mr. Paul Dunn
1	Mr. Bill Baker
1	Philips Elmet, 1560 Lisbon Road, Lewiston, ME 04240
1	ATTN: Mr. James Anderson
1	Ultramet, Inc., 12173 Montague Street, Pacoima, CA 91331
1	ATTN: Dr. J. J. Stiglich
1	Mr. Brian Williams
1	Dr. Robert Tuffias
1	Ceracon, Inc., 1101 N. Market Boulevard, Suite 9, Sacramento, CA 95834
1	ATTN: Dr. Ramas Raman
1	Mr. Sundeep Rele
1	Southwest Research Institute, 6220 Culebra Road, P.O. Drawer 28510, San Antonio, TX 78228-0510
1	ATTN: Dr. James Lankford
1	Metalworking Technology, Inc., 1450 Scalp Avenue, Johnstown, PA 15904
1	ATTN: Mr. C. Buck Skena
1	Mr. Timothy McCabe
1	Research Triangle Institute, P.O. Box 12194, Research Triangle Park, NC 27709-2154
1	ATTN: Dr. John B. Posthill
1	3C Systems, 620 Arglye Road, Wynnewood, PA 19096
1	ATTN: Mr. Murray Kornhauser
1	Advance Technology Coatings, 300 Blue Smoke Ct. West, Fort Worth, TX 76105
1	Alliant Techsystems, 7225 Northland Drive, Brooklyn Park, MN 55428
1	ATTN: Dr. Stan Nelson
1	Mr. Mark Jones
1	Mr. Thomas Steigauf
1	CAMDEC, 3002 Dow Avenue, Suite 110, Tustin, CA 92680
1	Chamberlain Manufacturing Co., 550 Esther St., P.O. Box 2545, Waterloo, IA 50704
1	ATTN: Mr. Tom Lynch
1	Defense Technology International, Inc., The Stark House, 22 Concord Street, Nashua, NH
1	ATTN: Mr. Douglas Ayer
1	Materials and Electrochemical Research Corporation, 7960 S. Kolb Road, Tucson, AZ 85706
1	ATTN: Dr. James Withers
1	Dr. Sumit Guha
1	Materials Modification, Inc., 2929-P1 Eskridge Center, Fairfax, VA 22031
1	ATTN: Dr. T. S. Sudarshan
1	Micro Materials Technology, 120-D Research Drive, Milford, CT 06460
1	ATTN: Dr. Richard Cheney
1	Nuclear Metals, 2229 Main Street, Concord, MA 01742
1	ATTN: Dr. William Nachtrab
1	Olin Ordnance, 10101 9th Street N., St. Petersburg, FL
1	ATTN: Hugh McElroy

No. of
Copies

To

1 The Pennsylvania State University, Department of Engineering Science and Mechanics, 227 Hammond Building,
University Park, PA 16802-1401

1 ATTN: Dr. Randall M. German, Professor, Brush Chair in Materials
Worcester Polytechnic Institute, 100 Institute Road, Worcester, MA 01690

1 ATTN: Dr. Ronald Biederman
1 Dr. Richard Sisson

Failure Analysis Associates, Inc., 149 Commonwealth Drive, P.O. Box 3015, Menlo Park, CA 94025

1 ATTN: S. P. Andrew
1 R. D. Caliguri
1 T. K. Parnell
1 L. E. Eiselstein

Amorphous Technologies International, Laguna Hills, CA
1 ATTN: Mr. Dick Harlow

Parmatech Corporation, 2221 Pine View Way, Petaluma, CA 94952
1 ATTN: Dr. Animesh Bose

Duffers Scientific Co., Route 355, Troy RRI, P.O. Box 1234, Poestenkill, NY 12140
1 ATTN: Dr. David Furguson

Lawrence Livermore National Laboratory, P.O. Box 808, L-35, University of California, Livermore, CA 94551
1 ATTN: Dr. Daniel Steinberg

Director, U.S. Army Research Laboratory, Watertown, MA 02172-0001
2 ATTN: AMSRL-OP-CI-D, Technical Library
20 AMSRL-MA-MB, Mr. Robert Dowding